Validated Numerical Simulations Investigating the Effects of Cross-sectional Asymmetry on Fluid Flow and Heat Transfer

A Dissertation

SUBMITTED TO THE FACULTY OF THE

UNIVERSITY OF MINNESOTA

BY

Abhimanyu Ghosh

IN PARTIAL FULFILLMENT OF THE REQUIREMENTS

FOR THE DEGREE OF

DOCTOR OF PHILOSOPHY

Dr. Ephraim Sparrow

November, 2017

Table of Contents

List of Tables

List of Figures

CHAPTER ONE

Introduction

Fluid mechanic phenomena are of great interest in their own right but are of equal or greater importance in their interaction with other transport processes such as heat transfer. This thesis deals with both these facets of fluid mechanic endeavor. The methodology used here for the solution of the selected complex physical situations is numerical simulation. The considered situations are primarily concerned with turbulent flows. In view of the current state of knowledge of turbulent flows, it is necessary to first focus attention on the logic of the selection of a turbulence model.

Consequently, Chapter Two is totally devoted to establishing the validity of the turbulence model that underlies the numerical simulations used in the succeeding chapters. The validation is based on the level of agreement between the numerical predictions and corresponding experimental data. The physical situation chosen for the validation study of Chapter Two is a pipe bend. This choice was influenced by the fact that the pipe bend geometry is encountered in later chapters of the thesis. Furthermore, as noted in Chapter Two, several other validation studies for a variety of turbulence models have been performed in our laboratory in recent years, all with the same outcome.

Chapter Three deals with a fundamental problem of fluid mechanics which has not heretofore been attempted to be solved. The physical situation may be termed a piezometer ring and may be connected with an instrument to measure circumferential pressure variations for pipe flows. Surprisingly, as pointed out in the literature review embedded in Chapter Three, the instrument has never been used properly as a measurement device. This reality means that there is no experimental data available to motivate consideration of a specific situation. Consequently, the piezometer ring study performed is to be considered as a fundamental case study problem of fluid mechanics.

A highly schematic diagram, taken from the literature, is conveyed in Fig. 1.1. The figure shows a circular pipe in which there is a flowing fluid. If the flow were perfectly axial, it would be expected that the pressure would be circumferentially uniform. However, if the pictured cross section were situated downstream of an asymmetric element such as a

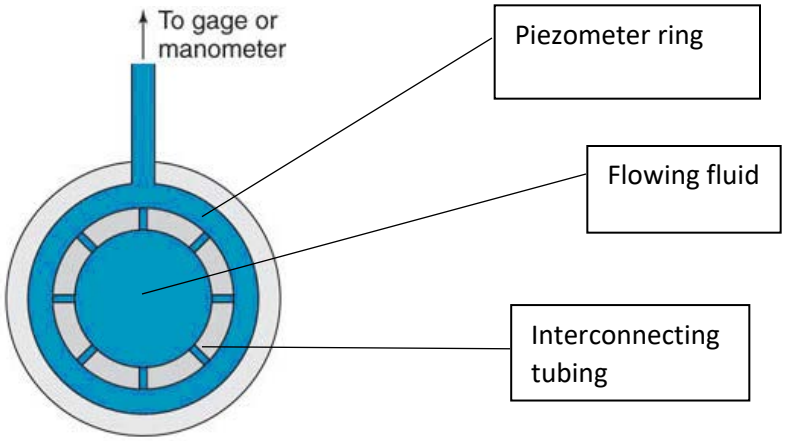

Fig. 1.1 *Schematic diagram of an installed piezometer ring*

right-angle bend, a significant circumferential pressure variation would result. Suppose that the figure represents a cross section just downstream of a right-angle bend. If the bottom of the pictured pipe represents the inside of the bend and the top corresponds to the outside of the bend, it is expected that the pressure will vary from low to high, from the bottom to the top. In such a situation, the fluid passing through the individual interconnecting tubing would carry the circumferential pressure variation that prevails in the pipe into the piezometer ring, thereby giving rise to a flowing stream in the ring proper. As a consequence of this external flow ringing the pipe, the circumferential pressure variation in the pipe would be altered.

The schematic figure, Fig. 1.1, shows a pressure take-off tap situated at the very top of the piezometer ring. In view of the circumferential circulation in the ring, it is unclear as to the relationship of that take-off pressure to the actual pressure variation in the pipe. The issue of where to position the location of the take-off pressure tap is one of the extreme weaknesses in the current uses of a piezometer ring. In particular, to the best knowledge of the author, there has been no attempt to quantify the circumferential

circulation in the ring nor to determine the pressure that would be measured at different circumferential locations of the take-off tap. The specific goal of Chapter Three is to create a valid physical model of the fluid mechanics of a piezometer ring, to quantify the patterns of fluid flow within the ring, and to determine the take-off pressure at all circumferential locations on the ring. Of particular focus is to find the particular take-off location which yields the average pressure in the pipe cross section in the absence of a ring.

To achieve these goals, a case study is performed in Chapter Three in which a piezometer ring is envisioned as being positioned just downstream of a right-angle bend. This configuration is chosen because it is accompanied by a significant circumferential pressure variation. The investigation, performed by means of highly detailed numerical simulation, makes use of both fluid flow and geometrical variables. The fluid flow Reynolds number was one of the independent parameters and the geometry of the piezometer ring was the second of the varied parameters.

Chapter Four is focused on the fluid mechanics and heat transfer phenomena encountered when a large-aspect-ratio rectangular jet passes through free space and may subsequently impinge on a plane surface. The uniqueness of the jet fluid flow investigation of Chapter Four is that it is the first study to take account of a phenomenon called jet axis switching for a turbulent jet. Although the axis switching phenomenon has been explored substantially from a purely fluid mechanics standpoint, there has been only a single study of related heat transfer phenomena. A detailed literature survey may be found in Chapter Four proper. In the aforementioned study, the flow rates were sufficiently small so that a laminar model was appropriate. Here, the more practical turbulent flow situation was investigated.

The aspect ratio (width-to-height) of the rectangular slot jet upon emergence was fixed at 10:1. This aspect ratio may be considered as assurance that the jet could be considered as nearly two-dimensional. The emerging jet discharges into an unobstructed airspace where it participates in the jet axis switching phenomenon. Farther downstream, an

impingement plate was positioned as a target. One of the key foci of the work was to appraise the effect of the axis switching on heat transfer coefficients due to impingement. The results of the jet investigation led to an explanation of certain peaks in the distribution of the heat transfer coefficient on the impingement plate. These peaks had been observed many decades ago but had been left unexplained.

The last substantive chapter of the thesis is Chapter Five. That chapter continues the theme of complex fluid mechanics and heat transfer that characterize the preceding chapters. The fluid-flow complexity of Chapter Five has two independently controllable causes. One of these is the secondary flow that occurs within a right-angle bend. The second is a partial blockage installed at the inlet cross section of the bend.

The specific problem chosen for investigation in Chapter Five is the fluid flow and heat transfer in a round pipe attached to the exit cross section of a 90^{o} bend and extending downstream from it. At the upstream end of the bend, wall-adjacent, washer-shaped blockages are installed. The bend geometry is characterized by the curvature ratio, which is the quotient of the radius of curvature of the bend axis divided by the diameter of the bend piping. Two values of the curvature ratio are considered: a ratio of 1 which corresponds to a sharp bend and a ratio of 3 which identifies a gradual bend. Two other independent variables are used in the study: the Reynolds number of the pipe flow and the blockage ratio, which is the quotient of the blocked cross-sectional area to the total cross-sectional area. The special case of no blockage is given equal footing with the with-blockage cases, both as a comparison baseline and a source of information not heretofore available in the literature.
The heat transfer problem is defined by adiabatic flow in the bend proper and heat transfer from the wall of the downstream pipe to the flowing fluid. The fluid arriving at the bend exit has a uniform temperature whereas the downstream pipe wall has a different uniform temperature.

The main heat transfer results are the streamwise variations of the circumferential-averaged local heat transfer coefficients as a function of the Reynolds numbers ranging

from 100 to 10,000, blockage ratios from 0 to 60%, and the aforementioned two values of the curvature ratio. To shed light on the observed trends in the heat transfer coefficient variations, both vector diagrams and color-contour diagrams of the fluid flow patterns are displayed.

The thesis concludes with Chapter Six, which is a retrospective view of the accomplishments of the thesis as a whole. The message conveyed by the thesis as a whole is the flexibility of numerical simulation as a means for solving relevant physical problems that are both complex and of a varied nature.

CHAPTER TWO

Quantitative Validation of the Numerical Simulation Model

2.1 Introduction

In this thesis, numerical simulation methodology is used to solve a number of intellectually fundamental and applied problems in fluid mechanics and heat transfer. These problems, although not unknown in engineering practice, appear not to have been subject to detailed investigation, neither in the laboratory nor by numerical means. As noted in Chapter One of this thesis, consideration is given to three problems which are respectively the subjects of Chapters Three, Four, and Five. The participating fluid flows encompass separation, swirl, turbulence, and axis switching, with heat transfer being a main feature. It can be argued that flows of such complexity deserve verification of whatever numerical model is used for their solution. In particular, since the chosen problems involve turbulent flow, it is imperative to examine the efficacy of the adopted turbulence model. The goal of this chapter to present a suitable verification for the chosen turbulence model and the numerical methods used in subsequent chapters.

In practice, the most accepted way of verifying numerical-based turbulence models is to compare predictions based on a given model with highly accurate experimental data. Although not widely acknowledged, implementation of this approach requires that the quantitative nature of the turbulence at the inlet of the flow space be known. In the absence of this information, most numerical codes provide the user the option to choose default values of turbulence intensity or related quantities. However, such options are of little merit when the actual turbulence quantities of the candidate validating experiments are not available. In reality, it is uncommon for experiments to include measurements of the inlet values of the turbulent state.

As noted in the foregoing paragraph, the unavailability of appropriate experimental information clearly increases the difficulty of performing definitive validations of

numerical predictions for a given problem. As a suitable alternative, it is reasonable to seek experimental measurements for a situation where the participating physical phenomena are the same as those that are encountered in the given problem, even if the experimental and numerical problems are not identical. This is the strategy being followed here.

Since two of the physical situations to be dealt with in this thesis include flow in pipe bends (elbows), it is not unreasonable to utilize appropriately detailed experiments involving bends for verification of a congruent numerical simulation model. Pipe bends involve swirl, flow separation, superposed circumferential and axial flows, and turbulence. The pipe-bend experiments of [1,2] provide detailed measurements of the state of the fluid (including turbulence) at the inlet of the flow space as well as downstream measurements suitable for comparisons with numerical predictions. Therefore, in this chapter, a detailed numerical simulation of the physical situation used in the experiments of [1,2] will be described and comparisons will be made of the numerical predictions with the experimental measurements.

As will soon be encountered, the outcome of the validation work of this chapter is the selection of the SST k-ω turbulence model. This specific outcome can be reinforced by additional verifications performed by others in our laboratory and elsewhere. In this regard, reference may be made to [3 - 5] for successful applications of the SST k-ω model to bends and for separated flows [6]. In addition, others have demonstrated the validity of the model for duct flows [7] and for flow through perforated plates [8]. Most recently, the comprehensive swirl-based data of [9] have been used as input to demonstrate the competence of the *SST* k-ω model for swirling flow and for flows with both laminar and turbulent portions [10]. The efficacy of the *SST* k-ω model stems from its origins as a blending of the two basic two-equation turbulence modeling platforms, k-ε and k-ω. The k-ω model has demonstrated great competence in near-wall regions while the k-ε model gives good results far from walls.

2.2 Physical Situation

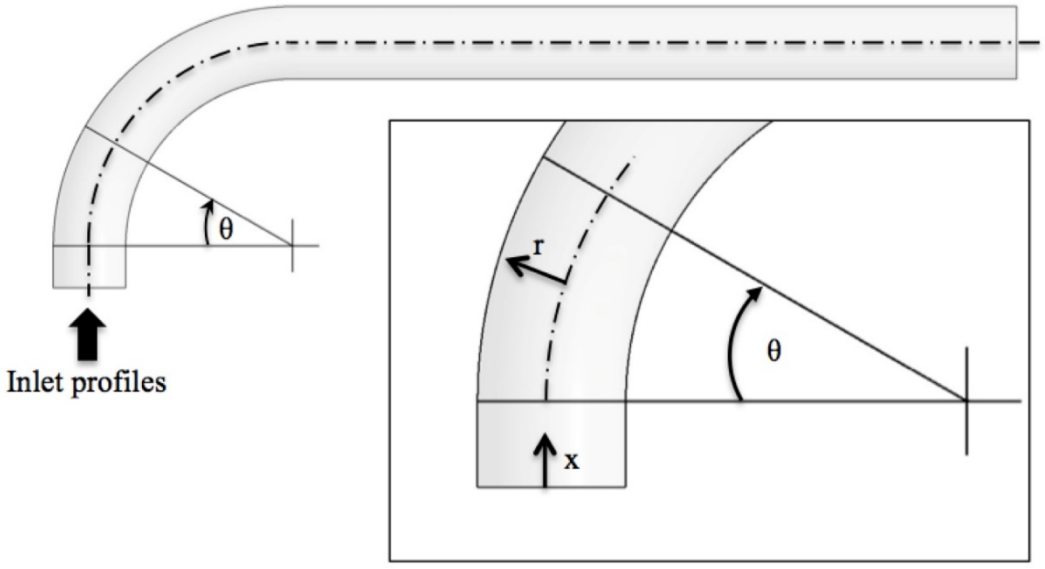

Fig. 2.1 *Schematic diagram of the experimental situation of [1,2]. The upper diagram displays the entire physical system, and the inset is a detail of the upstream end*

A schematic diagram of the fluid flow situation that was studied experimentally in [1,2] and used for validation purposes here is conveyed in Fig. 2.1. As seen in the figure, a pipe bend is mated at its upstream end with a short length of pipe and at its downstream end to a somewhat greater length of pipe. The pipe diameter is 48 mm, and the downstream straight section of pipe extended 480 mm (10 pipe diameters) beyond the exit of the bend i.e., $\theta = 90°$. The inlet boundary for the numerical simulation was located 0.58 diameters upstream of the start of the bend ($\theta = 0°$) because the available data (velocity profiles and turbulence intensities) was reported at that location. The bend radius of curvature is 2.8 times the pipe diameter.

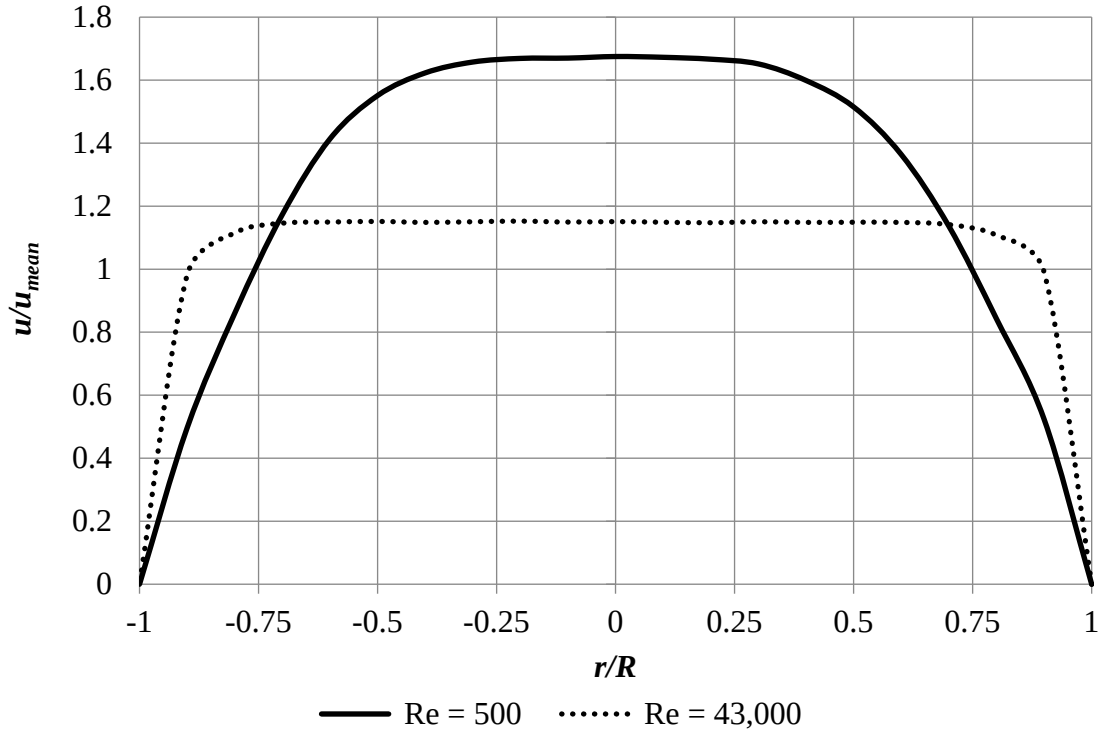

Fig. 2.2 *Axial inlet velocity profiles used for the numerical simulations based on the data of [1] and [2] at a location 0.58 pipe diameters before the bend.*

The measurements at x/D = 0 of axial velocity profiles and a turbulence intensity profile reported in [1,2] are displayed respectively in Figs. 2.2 and 2.3. In Fig. 2.2, dimensionless velocity profiles are conveyed for values of the pipe Reynolds number Re of 500 and 43,000. Not unexpectedly, the velocity profile corresponding to the higher Reynolds number (turbulent) is flatter than the profile for the lower Reynolds number case (laminar). Since the Re = 500 experiments corresponded to laminar flow, no turbulence intensity measurements were made for this case. Therefore, the information conveyed in Fig. 2.3 is confined to the turbulent flow case of Re = 43,000. It can be seen from the figure that strong turbulence is confined to a narrow annulus slightly displaced from the wall.

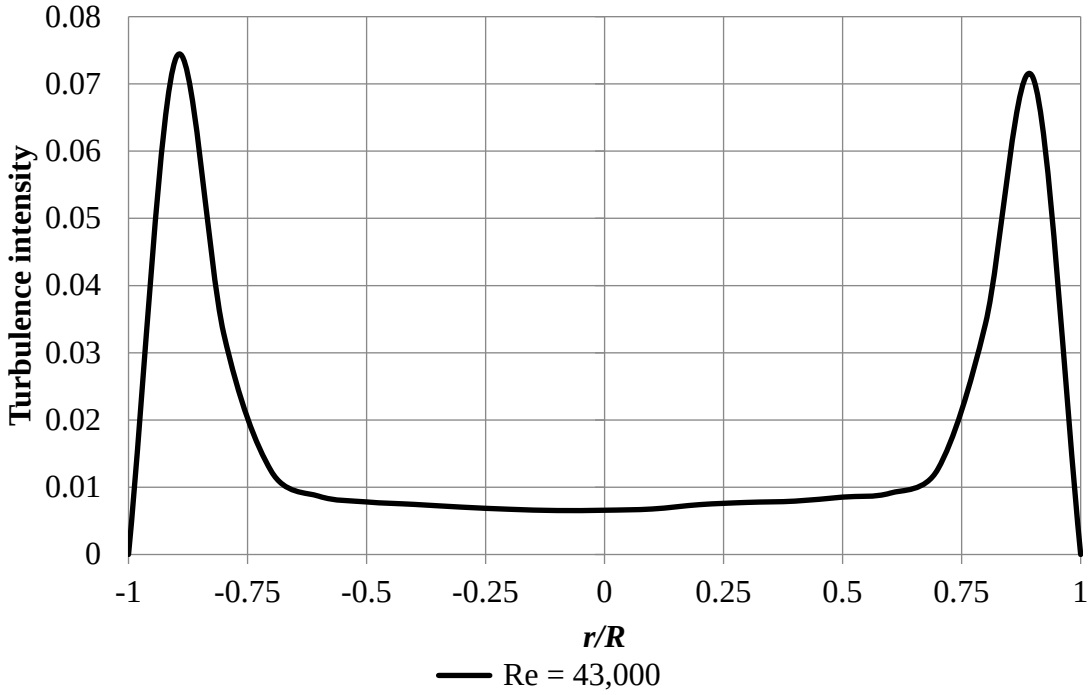

Fig. 2.3 *Inlet turbulence intensity profile used for the numerical simulation for Re = 43,000 based on data extracted from [1] and [2] at a location 0.58 pipe diameters before the bend.*

2.3 Numerical Simulation Model

The foregoing paragraphs describe the physical problem that was used for the validation of the numerical simulation methodology used throughout this thesis. Now, attention will be turned to the specific numerical simulation model whose validity is being explored. Although both laminar and turbulent flows are to be dealt with here, it will be sufficient to present the turbulent-flow equations and explain where these equations are to be modified for laminar flow. Numerical simulations of turbulent flow may be classified according to the nature of the method of solution. The most commonly used approach is to express the momentum conservation principle by means of the Reynolds-Averaged Navier-Stokes (RANS) equations. The steady-state, constant-property form of the RANS equations, written in Cartesian-tensor form, is

$$\rho\left(u_i \frac{\partial u_j}{\partial x_i}\right) = -\frac{\partial p}{\partial x_j} + \frac{\partial}{\partial x_i}\left((\mu + \mu_t)\frac{\partial u_j}{\partial x_i}\right) \quad i = 1,2,3 \;\; j = 1,2,3 \tag{2.1}$$

in which μ_t is called the turbulent viscosity. This quantity is not a material property as is the viscosity μ. Rather, it is a concept of convenience defined as

$$-\rho\overline{u_i'u_j'} = \mu_t \frac{\partial u_j}{\partial x_i} \tag{2.2}$$

For laminar flow, μ_t is eliminated from equation (1). The RANS equations do not conserve mass, so that a separate equation is needed to enforce that principle. It is the equation of continuity

$$\frac{\partial u_i}{\partial x_i} = 0 \tag{2.3}$$

The determination of μ_t depends on the specific turbulence model that is selected. The most-used approach is to select a model from the collection of two-equation models. This selection must be done carefully since certain models are more suitable than others for a specific physical situation. In that regard, it is relevant to take account of the expected physical processes that participate in the problem in question. For the problems considered in this thesis, the two special features are flow separation and secondary flow (swirl). For our purposes here, the SST *k-ω* turbulence model is used in the numerical simulations. The background information supporting the selection of this model as a candidate for adoption here is set forth at the end of the Introduction of this chapter. The governing differential equations for the SST *k-ω* model are

$$\frac{\partial(\rho u_i \kappa)}{\partial x_i} = P_\kappa - \beta_1 \rho \kappa \omega + \frac{\partial}{\partial x_i}\left[\left(\mu + \frac{\mu_t}{\sigma_\kappa}\right)\frac{\partial \kappa}{\partial x_i}\right] \tag{2.4}$$

$$\frac{\partial(\rho u_i \omega)}{\partial x_i} = A\rho S^2 - \beta_2 \rho \omega^2 + \frac{\partial}{\partial x_i}\left[\left(\mu + \frac{\mu_t}{\sigma_\omega}\right)\frac{\partial \omega}{\partial x_i}\right] + 2\rho(1 - F_1)\frac{1}{\sigma_{\omega 2}\omega}\frac{\partial \kappa}{\partial x_i}\frac{\partial \omega}{\partial x_i} \tag{2.5}$$

The solution to equations (4) and (5) yields the values of κ and ω, which give the turbulent viscosity μ_t through

$$\mu_t = \frac{\alpha\rho\kappa}{\max(\alpha\omega, SF_2)} \tag{2.6}$$

The symbols that appear in the foregoing equations are defined as

A	model constant
F_1, F_2	blending functions in the SST model
P_k	production term for the turbulent kinetic energy
S	absolute value of the shear strain rate
u	local velocity
x_i	tensor coordinate direction
α	SST model constant
β_1, β_2	SST model constants
ω	specific rate of turbulence dissipation
κ	turbulent kinetic energy
μ	molecular viscosity
μ_t	turbulent viscosity
σ	diffusion coefficient
ρ	fluid density

2.4 Numerical Solutions and Model Verifications

General Mesh Details

The solutions of the discretized forms of the governing differential equations were carried out by means of ANSYS CFX 16.1 software. A mesh independence study was performed with 5.5 million nodes and 14 million nodes for both the laminar and turbulent simulations. The overall pressure drop in the piping system was used as a metric for this mesh independence study, defined as the pressure drop between the inlet and the downstream outlet of the system. The percent difference in pressure drop between the

two node counts was 0.2% and 0.3% respectively for the laminar and turbulent cases. The maximum y+ value was 4.3 for the turbulent simulation.

Experimental Verification Details

As has already been noted, a necessary requisite for the confident use of a numerical simulation model is to verify the predictions provided therefrom with data from well-executed experiments. That search for suitable information yielded references [1] and [2], where suitable careful experiments are described. The information required to run the numerical simulations based on these experiments is shown in Figs. 2.1-2.3 and is taken from [1] and [2].

In Figs. 2.4 and 2.5, comparisons are made between the results from the present numerical simulations and the experimental results from [1] and [2]. Two angular stations within the bend were selected for the measurements, specifically $\theta = 30$ and 60^o. The information is presented as a normalized velocity profile along a diametral line extending from the inner edge to the outer edge of the bend cross section and passing through the center of the pipe. The laminar flow results (Re = 500) are conveyed in Fig. 2.4 and those for turbulent flow (Re = 43,000) are displayed in Fig. 2.5.

Inspection of Fig. 2.4 shows that the results at 30^o are more symmetric than those at 60^o, an outcome that can be attributed to the former's shorter residence time within the bend. The skewness of the latter profile is due to the packing of the flow to the outside of the bend. The agreement between the experimental data and the numerical predictions is excellent, aside for minor deviations near the outside of the bend cross section.

Figure 2.5 is for turbulent flow and, therefore, displays the degree of validation of the SST k-ω turbulence model. In truth, it appears that the level of agreement between the numerical predictions and the experimental data for the turbulent flow case (Fig. 2.5) is even better than that for the laminar case of Fig. 2.4.

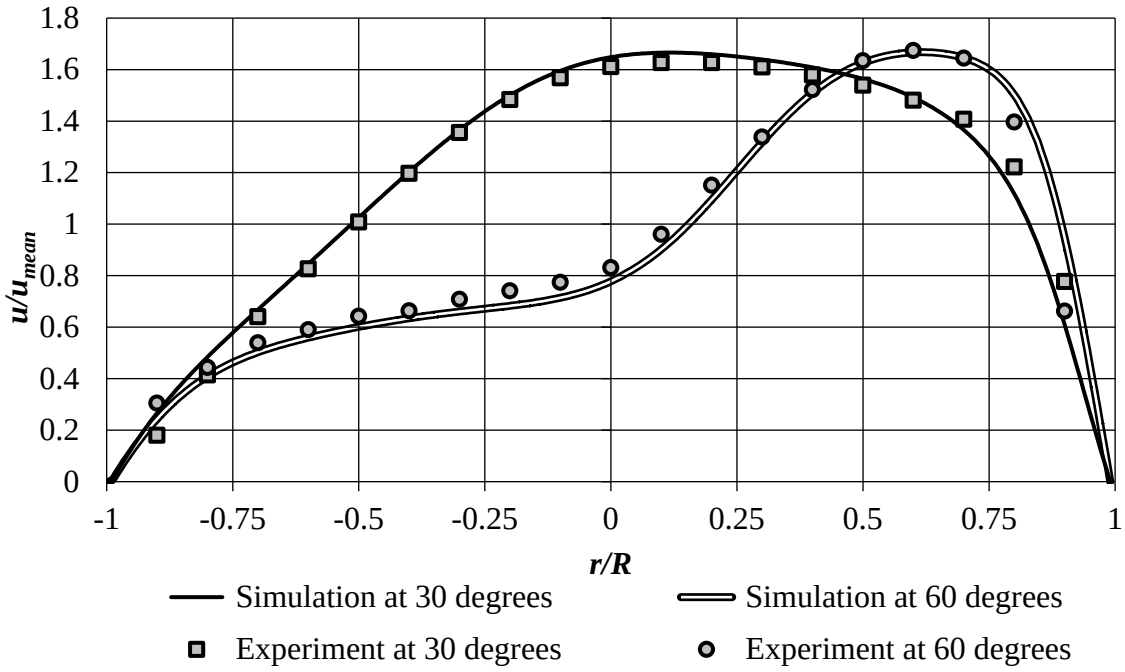

Fig. 2.4 *Comparison with experimental laminar flow velocity measurements [1, 2] at θ = 30° and 60° into the bend. Re = 500, U_{mean} = 0.0105 m/s*

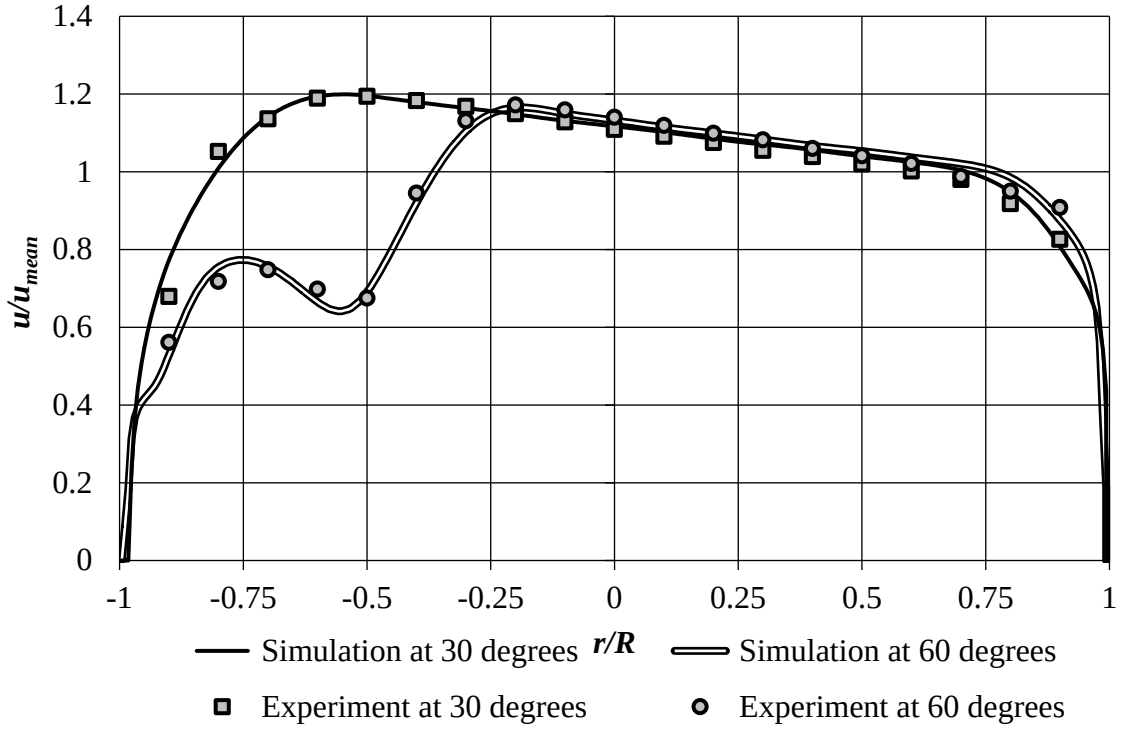

Fig. 2.5 *Comparison with experimental turbulent flow velocity measurements [1, 2] at θ = 30° and 60° in the bend. Re = 43,000, U_{mean} = 0.91 m/s.*

2.5 Concluding Remarks

The goal of the current chapter has been to validate tools that will be used throughout the remainder of this thesis. Although numerical simulation techniques have become well established over the years, it is still necessary to validate certain physical models that lie at the heart of simulation in certain areas. This is especially true in the field of fluid mechanics, especially when the problems under consideration involve turbulence. There is a plethora of models that have been developed for modeling turbulent flows. Some of these claim to be universal whereas others been developed for specific categories of problems. Notwithstanding specific claims of competence, it is essential that the capabilities of a model be verified before it is extensively utilization as a tool for solving complex fluid flow problems which have never been solved in the past.

Over the years, it has become acceptable to validate fluid-mechanic models for numerical simulation by means of experimentation. One difficulty with this approach, rarely acknowledged, is that the validating experiments encompass data which include a complete description of the fluid flow. In the case of turbulent flow, the appropriate experiments must include a description of the turbulence field at the inlet of the solution domain. This is an uncommon measurement, so that the absence of the corresponding information has blocked true validation efforts.

The absence of the requisite turbulence information at inlet has required the acceptance of some compromises in the validation work. In most cases, when appropriate experimental data is absent for a given problem for which simulation is to be performed, an acceptable compromise is to identify a sister problem which encompasses the same physical phenomena as in the problem of direct interest. If the sister problem is endowed with complete experimental data, including the inlet turbulence, it may be used for the validation task.

The discussion in the preceding paragraph pertains to the current situation. Specifically, none of the problems selected for study here have been subjected either to numerical simulation or to experimentation. However, all of the selected problems encompass

turbulent flow and two of them involve pipe bends. As luck would have it, an experimental study of a pipe bend was found where all the needed information for a validation assessment of numerical simulation was available. A detailed description that validation assessment was performed in this chapter, with a very favorable outcome. It was found that the use of the SST k-ω turbulence model led to simulation predictions that were in excellent agreement with the experimental measurements. This outcome lends strong support to the validity of the numerical simulations to be presented in the succeeding chapters of the thesis.

CHAPTER THREE

Fluid-Mechanic Interactions Between a Pipe Flow Having Circumferential Pressure Variations and a Girdling Piezometer Ring

Abstract

A piezometer ring is a small-diameter tube formed into the shape of a circle which girdles a pipe which contains a flowing fluid. The outer surface of the pipe wall is connected to the ring by means of several hollow radial spokes (i.e., pipe stubs). If there are circumferential pressure variations within the pipe flow, these variations are transmitted to the ring and may set up a flow in the ring which can, in turn, alter the flow in the pipe. This complex fluid flow appears yet to be subjected to analysis based on a first-principles, fluid-mechanic model. Piezometer rings have been employed in the measurements of pressure in internal flows, but without a full understanding of the fluid-mechanic issues involved. In particular, the issue of where to tap-off the pressure in the ring to achieve a best determination of the pressure in the pipe flow has not yet been addressed. Here, the interactive fluid mechanics between a ring and a pipe flow characterized by significant circumferential pressure variations has been modeled with hi-fidelity and free of accuracy-compromising assumptions. The model was based on turbulent flow, and an *a posteriori* analysis of the magnitude of the turbulent viscosity results supported this choice. The solution tool was high-accuracy numerical simulation. Two independent variables were used as independent parameters: (a) the pipe Reynolds number which ranged from approximately 50,000 to 200,000 and (b) the geometry of the piezometer ring. A major outcome of the analysis was a definitive specification of the optimal pressure take-off locations at the outer surface of the ring that give accurate information about the pressure in the pipe cross section.

3.1 Introduction

Pipe flows normally are governed by the pipe wall geometry, the thermophysical properties of the flowing fluid, and the Reynolds number. A piezometer is a small tube configured in the shape of a continuous ring that is connected to the external wall of a pipe by means of short radial pipe stubs. Fluid is free to flow between the piezometer ring and the pipe proper depending on the prevailing pressure distributions in the ring and the pipe. The flow in the ring is primary circumferential, following the axis of the ring. In contrast, the flow in the pipe is primarily in the direction of the pipe centerline. Commonly, a number of interconnecting radial pipe stubs are deployed circumferentially around the periphery of the pipe proper. There is a likelihood that the direction of fluid flow through the individual pipe stubs may differ among the respective stubs.

Consideration of the qualitative description set forth in the preceding paragraph offers a possible explanation of why the interactive fluid-flow problem involving a pipe flow and a piezometer ring has not been subjected to first-principle-based analysis. The present authors believe that the issue may be the complexity of the flow. The only attempt at analysis is due to Blake [11] in 1975. The importance of that paper as the only published attempt at analysis of the problem in question motivates a thorough discussion of its contents. The physical model considered by Blake is pictured in Fig. 3.1. Seen there is a fluid flowing in pipe flow which experiences circumferential pressure variations that give rise to pressures p_1, p_2, p_3, and p_4 at locations situated at 90^o intervals around the circumference of the pipe wall at the sites of the pipe stubs that link the pipe proper to the piezometer ring. No discussion is provided by Blake about the nature of the pipe flow by which the pressure variation is created. Furthermore, it is unclear whether the values of p_1, p_2, p_3, and p_4 are those at the selected locations prior to or after the piezometer ring was put in place.

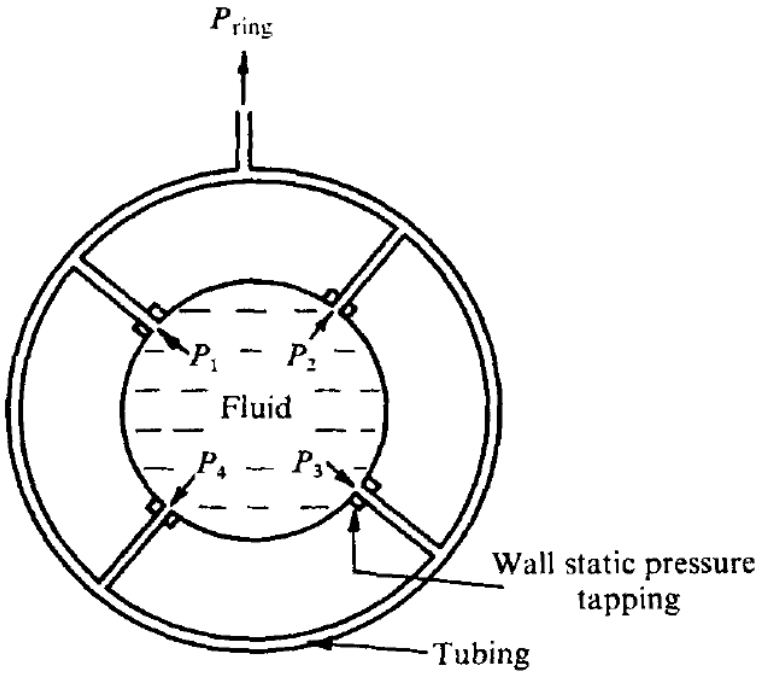

Fig. 3.1 *Physical model analyzed by Blake [11].*

The approach used by Blake neither analyzed the fluid mechanics of the piezometer ring nor the interactions of the ring with the flow in the pipe. Rather, it was assumed that the flows in the four straight radial pipe-stub segments and in the four circumferential curved segments of the ring were fully developed and laminar (i.e. Poiseuille flow). These assumptions are grossly deviant from reality. The choice of this model totally removes the need for a fluid-mechanic analysis since Poiseuille flow is a classical flow that is well documented in the literature.

Blake set up a linear resistance network by using the linear relation between the volumetric flow rate and pressure drop for fully developed laminar flow. If the fluid flow rate Q is taken to be analogous to the electric current flow I and the pressure drop Δp is regarded as analogous to the voltage drop V, a fluid-flow Ohm's Law emerges as $Q = \Delta p/R$, where R is the flow resistance. The numerical values of R are readily determined from the diameters and lengths of the individual segments and the properties of the flowing medium. Algebraic linear circuit theory was used by Blake to solve for the fluid flows and the pressure drops in each the branches.

Two relevant assumptions set forth in Blake's work are (a) the pressure p_{pipe} in the main flow passing through the pipe is

$$p_{pipe} = (p1 + p2 + p3 + p4)/4 \quad (3.1)$$

and (b) the pressure in the ring at a location midway between adjacent taps separated by 90^o is the average of the pressures at the adjacent tap locations.

A piezometer ring is a device which, in principle, should find use in fluid-flow experiments to provide pressure information when there are pressure variations around the perimeter of the pipe-flow cross section. Such pressure variations occur in complex fluid flows in which the velocity vectors of the flow are not straight and parallel to the axis of the pipe. A frequently encountered situation where such a flow prevails is a pipe bend and in the straight pipe downstream of the bend.

If the individual pipe-stub flows that either or leave the piezometer ring are different from each other, it may be expected that a flow will be induced in the ring itself. Such a flow, if existent, will experience frictional resistance at the internal walls of the piezometer ring. By this means, a circumferential pressure variation around the ring will be created that may be different from the circumferential pressure variation in the pipe-flow proper.

In light of the foregoing, it is remarkable that the forthcoming literature search revealed that the use of piezometers rings has been restricted to situations where significant circumferential pressure variations are not necessarily encountered or expected.

In the present research, no assumptions are made about the prevailing fluid mechanics, neither in the ring, the interconnecting pipe stubs, nor the pipe proper.

3.2 Literature Survey

In 1938, Vilbrandt [12] made use of a pipe-enveloping annulus which may be regarded as an early version of a piezometer ring. Vleggaar and Tels [13] were the first to use a piezometer ring with four distinct pipe-stub-type taps situated at 90^o intervals around the

circumference of a pipe while measuring drag reduction caused by introduction of a polymer into liquids. The four-tap, 90^{o}-deployment configuration is repeated in many other applications. These include the determination of pressure drop in heat transfer tubing having helical internal ridging [14], hydraulic capacity measurements of a slip-lined pressurized pipeline [15], etc. A unique application due to Beyler [16] made use of seven taps to test pressures in a sprinkler assembly. The use of piezometer rings in connection with venturi meters was introduced by Petroe [17] in a 1943 patent. Inasmuch as a venturi meter is designed as an axisymmetric device, the reason for the use of a piezometer ring is not clear. Keagy *et al*. [18] used piezometer rings to measure flow rates in their Schlieren experiment involving mixing in gas jets. In Collins and Gacesa [19], piezometer rings were again used as part of the setup with four venturi meters, but no details of their configuration are mentioned.

Keulegan and Beij [20] used the conventional four-tap piezometer ring to measure flow rates in turbulent regimes in curved pipes. In an even more complex application, Welsh [21] used a piezometer ring to measure flow rates for unsteady flows through wide-angled conical diffusers. The mean axial velocity deduced from the piezometer-ring measurement was compared with that measured by a cobra probe. Bullen *et al.* [22] made use of a Triple-T piezometer-ring configuration for obtaining static pressure values in a pipe flow with an abrupt contraction. The piezometer ring was calibrated by replacing the large-bore upstream segment of the pipe with a pipe segment of the same diameter as that of the downstream segment and observing the deviations due to friction loss. A patented design by Kurszewski and Selinger [23] from as late as 2007 is based on the use of two four-tap piezometer rings, respectively upstream and downstream of a fan. Although the four-tap configuration is more or less standard and is widely accepted, the authors justified its use because it is presumed to correct for uneven pressures at the cross section of interest.

Aside from the cited works by Welsh and by Bullen *et al*., there is little evidence that the users of piezometer rings had given much attention to the accuracy of the results obtained therefrom. In none of the thus-far cited papers was there any attempt to investigate the

fluid mechanics occurring in the piezometer ring and how that fluid mechanics affects the flow and pressure fields in the pipe to which the piezometer is attached.

There is a crucial and decisive feature of all the foregoing cited literature that may well serve to diminish its worth. That feature is the total absence of any expressed concern about where on the ring circumference to tap-off the pressure for subsequent measurement by a suitable meter. This issue can be made clear by inspection of Figure 3.1 where attention may be directed to the tap-off port labeled p_{ring}. Neither Blake [11] nor any of the authors of the cited literature addressed the issue of where to locate the tap-off port. The logic-based approach to determining the correct tap-off point is a full-blown fluid-mechanic analysis.

3.3 Research plan

Although it would appear logical to connect the forthcoming analysis to experimental data, the available data does not contain sufficiently detailed information on which to base a corresponding analytical model. For example, a major flaw in the available experimental measurements is the absence of any definitive information about the circumferential variation of the pressure. Another possible disconnect is that the available experiments are limited to very moderate circumferential pressure variations. These observations persuaded the authors to undertake the present work as fundamental research in fluid mechanics, without the limitations of the currently available experiments. The goal of the work is perform as complete an analysis as possible in order to demonstrate the methodology that may be used by others who are more immediately concerned with experimentation.

To ensure archival status, it is necessary that the present model avoid arbitrary inputs, in particular, for the circumferential pressure variation in the pipe flow. Rather, it is appropriate that the pipe pressure distribution correspond to a real physical situation that can be readily reproduced by others and serve as a baseline case. A valid candidate for this situation is the flow in a pipe bend. It is well documented that the flow both within the bend and at the bend exit possess large circumferential pressure variations. Although

there are numerous pipe bend studies in the literature, the authors have provided their own solutions because of the use of a well-supported model and of their currently superior computer resources.

3.4 Baseline case

With respect to the realities of engineering practice, a 90^o pipe bend is the most commonly encountered component that creates significant pressure variations around its circumference. It is, therefore, a logical focus for an in-depth investigation of the characteristics of a piezometer ring. In order to create a frame of reference for the effect of the piezometer ring, it is natural to first evaluate the nature of the flow and pressure fields in the absence of the ring. That physical situation will be designated as the baseline case.

Physical model

A schematic diagram of the piping system selected for study, without the piezometer ring, is shown in Fig. 3.2. As seen there, the system consists of a straight length of pipe upstream of the bend, the bend proper, and a downstream length of straight piping. In terms of the pipe diameter D, the upstream and downstream lengths are about 12D and 73D respectively, while the curvature ratio, equal to the diameter of the pipe to the diameter of curvature, 0.25. The sole operating parameter is the Reynolds number of the pipe flow, the values of which were selected to be 50,400, 94,100, and 201,500. These Reynolds numbers correspond to turbulent flow.

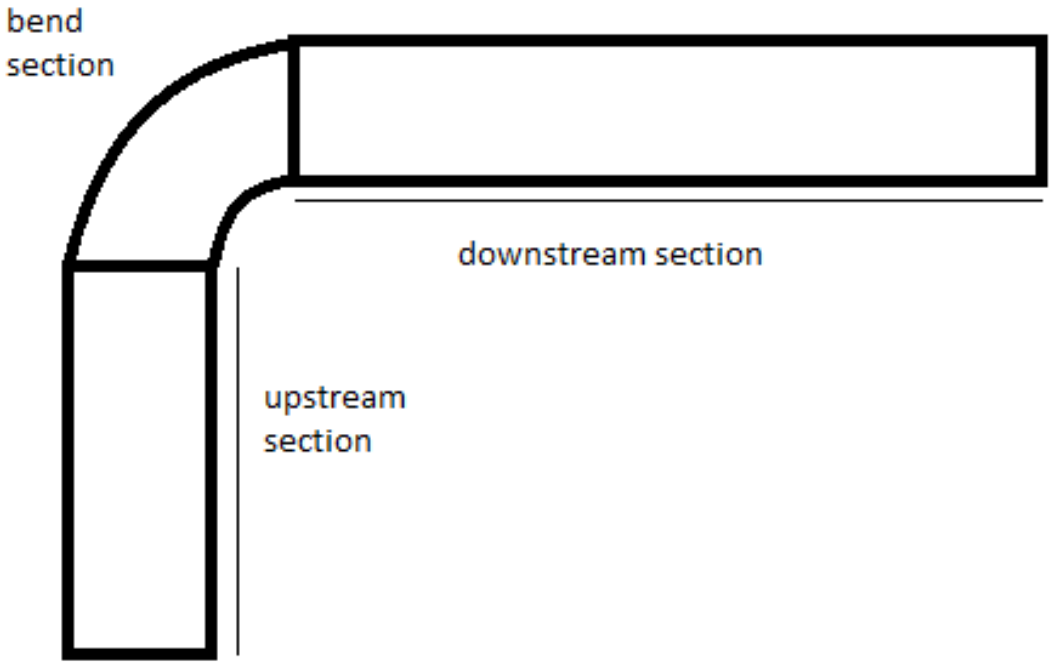

Fig. 3.2 *Schematic diagram of a piping system containing a 90^o bend.*

Governing equations

The starting point of the numerical simulation for the baseline case is the equations for momentum and mass conservation. The momentum conservation equations for turbulent flow are the Reynolds-Averaged-Navier-Stokes equations (RANS). In Cartesian tensor notation, the three components of the RANS equations are

$$\rho\left(u_i \frac{\partial u_j}{\partial x_i}\right) = -\frac{\partial p}{\partial x_i} + \frac{\partial}{\partial x_i}\left((\mu + \mu_{turb})\frac{\partial u_j}{\partial x_i}\right) \quad j = 1,2,3 \qquad i = 1,2,3 \tag{3.2}$$

The quantity μ_{turb} is the turbulent viscosity, which represents the Reynolds stresses. In the RANS formulation, turbulence isotropy is intrinsic. These equations are supplemented by the equation of continuity,

$$\frac{\partial u_i}{\partial x_i} = 0 \tag{3.3}$$

Turbulence model

A painstaking study was made for the selection and validation of an efficacious turbulence model. There are a number of models which purport to provide information and numerical values for the turbulent viscosity μ_{turb}. It is well established practice to validate the efficacy of competing turbulence models by critical comparisons with experimental data. A careful literature search coupled with prior experience led to the selection of the SST κ-ω turbulence model for application here, where κ is the turbulence kinetic energy, and ω is the specific rate of turbulence decay.

The selection of the *SST k-ω* turbulence model for application here is based on a substantial literature. In this regard, reference may be made [3-5] for successful applications of the SST *k-ω* model to bends and for separated flows [6]. In addition, the present authors have demonstrated the validity for duct flows [7] and for flow through perforated plates [8]. Most recently, they [9] have employed the comprehensive swirl-based data of [10] as input to demonstrating the competence of the *SST k-ω* model for swirling flow and for flows with both laminar and turbulent portions.

The efficacy of the *SST k-ω* model stems from its origins as a blending of the two basic two-equation turbulence modeling platforms, *k-ε* and *k-ω*. The *k-ω* model has demonstrated great competence in near-wall regions while the *k-ε* model gives good results far from walls. Another reason for this choice is that it auto-transforms to laminar flow for suitably small Reynolds numbers. Although the flow in the pipe is fully expected to be turbulent, it is possible that the flow in the piezometer ring may be laminar.

The equations of the SST model are partial differential equations for the turbulence kinetic energy κ and the turbulent eddy frequency ω. They are

$$\frac{\partial\left(\rho u_i \kappa\right)}{\partial x_i} = P_\kappa - \beta_1 \rho \kappa \omega + \frac{\partial}{\partial x_i}\left[\left(\mu + \frac{\mu_{turb}}{\sigma_\kappa}\right)\frac{\partial \kappa}{\partial x_i}\right] \tag{3.4}$$

$$\frac{\partial\left(\rho u_i \omega\right)}{\partial x_i} = A\rho S^2 - \beta_2 \rho \omega^2 + \frac{\partial}{\partial x_i}\left[\left(\mu + \frac{\mu_{turb}}{\sigma_\omega}\right)\frac{\partial \omega}{\partial x_i}\right] + 2\left(1 - F_1\right)\rho \frac{1}{\sigma_{\omega 2}\omega}\frac{\partial \kappa}{\partial x_i}\frac{\partial \omega}{\partial x_i} \tag{3.5}$$

The solution of Eqns. (3.4) and (3.5) yields the values of $\boldsymbol{\kappa}$ and ω, which give the turbulent viscosity μ_{turb} from

$$\mu_{turb} = \frac{\alpha \rho \kappa}{\max(\alpha\omega, SF_2)} \tag{3.6}$$

The symbols that appear in the foregoing equations are defined as

A model constant

F_1, F_2 blending functions in the SST model

P_k production term for the turbulent kinetic energy

S absolute value of the shear strain rate

u local velocity

x_i tensor coordinate direction

α SST model constant

β_1, β_2 SST model constants

ω specific rate of turbulence dissipation

κ turbulent kinetic energy

μ molecular viscosity

μ_t turbulent viscosity

σ diffusion coefficient

ρ fluid density

To establish the upstream boundary condition, supplementary numerical solutions were performed for flow in the piping system. The downstream portion of the modeled piping system is sufficiently long to assure the attainment of fully developed flow. The thereby-determined fully developed velocity profiles were used as the upstream boundary condition and were applied at a location that is 12 pipe diameters upstream of the bend. The downstream boundary condition, applied at the exit of the pipe, is that the streamwise second derivatives of all the velocity components are zero, and the gage pressure was also specified as being zero.

Numerical solutions

The partial differential equations encountered in this numerical simulation were solved by employing ANSYS CFX 15.0 software. The discretization of the partial differential equations was performed by the software by means of the finite-volume method. The solution domain was meshed by between 9 and 12 million nodes for the different cases that were investigated. A mesh independence study was performed to determine the accuracy of the discretization. The overall pressure drop was selected as the metric for the mesh independence study. For meshes consisting of 9 and 12 million nodes, the calculated overall pressure drops differed by only 0.3%. This level of coincidence can be regarded as sufficient witness to mesh independence. Also, a convergence criterion of 10^{-6} was also used for the computational residuals.

3.5 Pipe circumferential pressure variations for the no-ring baseline case

Inasmuch as the largest circumferential pressure variations for the pipe-flow case (without a piezometer ring) occur in the pipe situated at the very exit of the bend, it is appropriate to display detailed information about the pressure field at that location in the absence of the ring. To provide orientation definitions that are relevant to that display, Fig. 3.3 has been prepared. The figure shows the circular cross section of the pipe at the bend exit along with callouts describing the orientation of the bend. The locations θ = 0, 90, 180, and 270° mark the installation of the radial-oriented pipe stubs. The angular positions θ = 0 and ±180^o respectively correspond to the outer and inner radii of the bend.

To display the circumferential pressure variations in the pipe at the bend exit, it is appropriate to use dimensionless parameters to generalize the outcome. To this end, the cross-sectional-average pressure $\overline{p_{exit}}$ at the bend exit is evaluated from the numerical solutions and then combined with other known quantities to yield the dimensionless pressure p^{**} defined in Eq. (3.7). The numerator of the equation is the local pressure difference with respect to the cross-sectional mean, while the denominator is the so-called velocity head in which U is the mean velocity of the pipe flow.

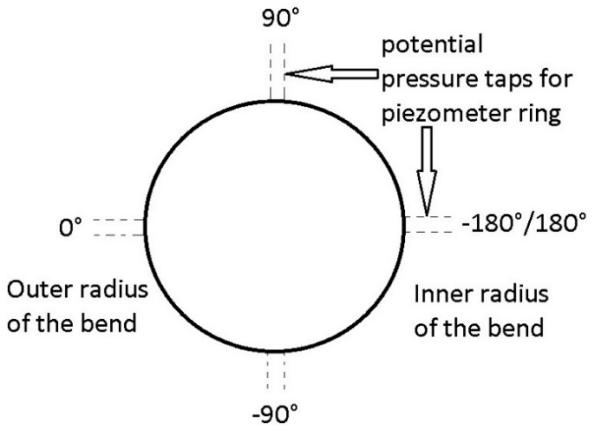

Fig. 3.3 *Schematic diagram of the cross section of the pipe at the bend exit with 90º-deployed taps to connect the piezometer ring to the pipe*

For reference, the values of the velocity head for airflow in units of Pa are 990.2, 3451, and 15,820 for *Re* = 50,400, 94,100, and 201,500 respectively. The definition of p^{**} is

$$p^{**} = \frac{p - \overline{p_{exit}}}{\frac{1}{2}\rho U^2} \tag{3.7}$$

A graph displaying the dimensionless circumferential pressure variations at the pipe wall that bounds the exit cross section is conveyed in Fig. 3.4. In that display, the quantity p^{**} is plotted as a function of the angular coordinate that was defined in Fig. 3.3. Inspection of Fig. 3.4 shows that there is a substantial circumferential variation of the pressure at the pipe wall, on the order of 0.4 velocity heads. After non-dimensionalization, the results for the three Reynolds numbers are virtually identical. Since the highest pressure occurs at the outside of the bend, p^{**} is a maximum there. The lowest pressure exhibited in Fig. 3.4 is slightly displaced from the inside of the bend. It is relevant to note that the results of Figure 4 correspond to the absence of the piezometer ring and will, therefore, serve as a basis of comparison to identify the impact of the presence of the ring.

The numerical solutions yielded a plethora of information about the fluid mechanics of pipe bends in the absence of the piezometer ring. However, that information is peripheral to the focus of the present investigation and need not be presented here.

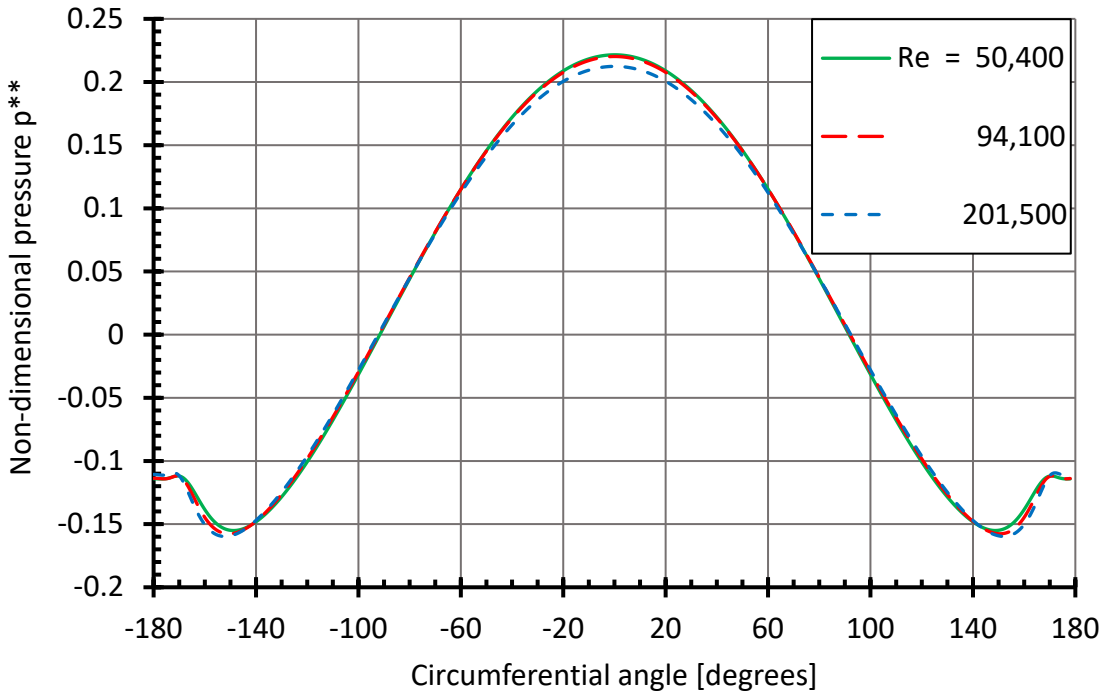

Fig. 3.4 *Circumferential variation of the dimensionless pressure p** at the bounding wall of the pipe at the exit of the bend in the absence of the piezometer ring*

3.6 Pipe circumferential pressure variations for the with-ring case

The numerical solutions for the situation in which a piezometer ring is installed on the pipe immediately downstream of the bend exit requires much more extensive calculations than those for the case in which there is no ring. In particular, the bend and all its upstream and downstream piping continue to be involved in the calculations, but now the piezometer ring must also be taken into account.

Two different piezometer rings were considered for investigation. These are respectively designated as the smaller ring and the larger ring. The geometries of these rings are respectively displayed in Figs. 3.5(a) and 3.5(b). It is seen from these figures that the internal diameter of the pipe proper remains the same for the two different rings. Note that thickness of the pipe wall in the geometrical setup has been neglected since it plays no role in the numerical simulations. For the larger ring, the diameter of the ring and the diameters and lengths of the interconnecting pipe stubs (spokes) have all been enlarged compared with those for the smaller ring.

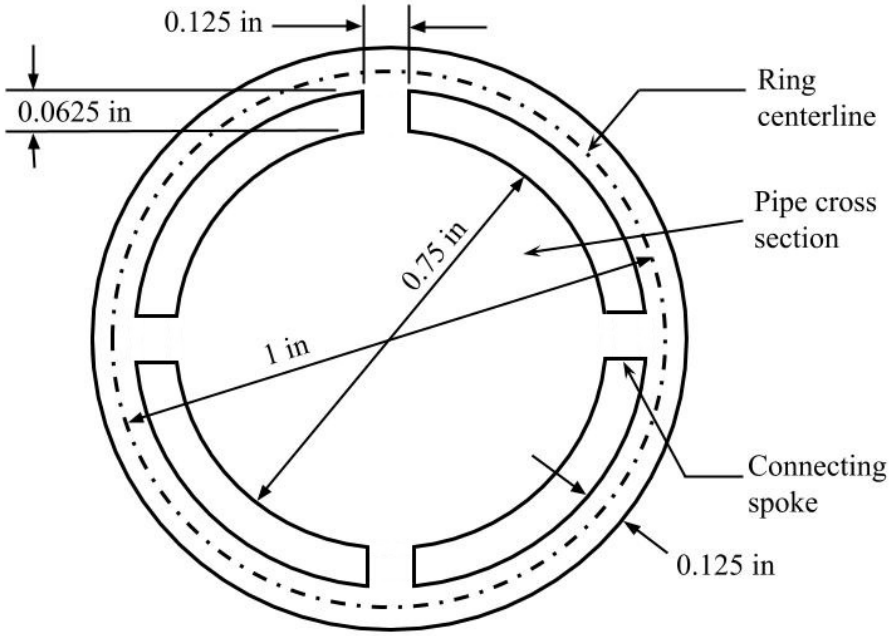

Fig 3.5(a) *Schematic diagram of the geometry of the smaller piezometer ring.*

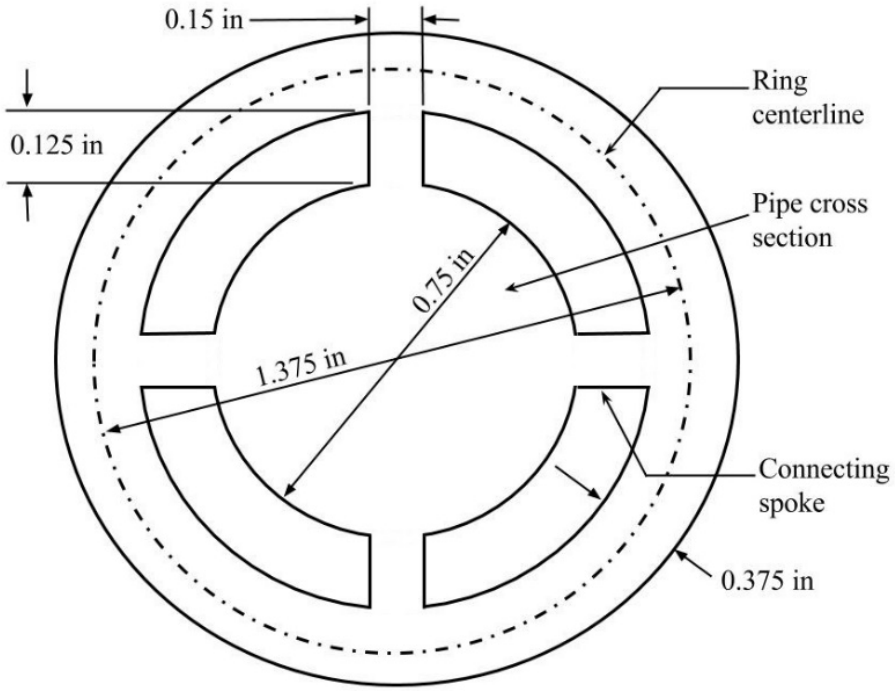

Fig 3.5(b) *Schematic diagram of the geometry of the larger piezometer ring.*

The first focus of the presentation is the circumferential variation of the dimensionless pressure p^{**} at the bounding wall of the pipe at the exit of the bend. This information is conveyed in Figs. 3.6(a) and 3.6(b), respectively for the smaller and larger ring.

An overview of Figs. 3.6(a) and 3.6(b) reveals general trends that are quite similar to the no-ring results displayed in Fig. 4 but with significant differences at the locations of the spokes (pipe stubs) which interconnect the pipe and the ring. Since these differences are undoubtedly related to the fluid flowing in the spokes, it is relevant to examine the magnitudes and directions of the individual flows in each spoke. These mass flow and directions are conveyed in Table 3.1 for both the smaller and larger piezometer rings and for all three investigated Reynolds numbers. Positive numbers in the table indicate that the flow is from the pipe into the ring, and negative numbers correspond to flow from the ring into the pipe.

Inspection of the table shows that for any fixed Reynolds number and ring geometry, the larger of the individual mass flow rates occur at the outside ($\theta = 0^o$) and at the inside ($\theta = \pm 180^o$) of the bend, with the former being a flow from the pipe to the ring and the latter from the ring into the pipe. At the intermediate locations $\theta = \pm 90^o$, there is a weak flow from pipe to ring. The slight differences between the impacts of the spoke flows on the pressure distributions conveyed in Figs. 3.6(a) and 3.6(b). Note that the numerical values conveyed in the table for a given Reynolds number and ring geometry sum to zero, thereby confirming the steady state nature of the model.

The minor differences in pressure between those for the small and large piezometer rings as seen in Figs. 3.6(a) and 3.6(b) respectively are attributable larger angular spans of the spokes for the latter.

Table 3.1 *Mass flow rates through spokes interconnecting the pipe and the piezometer ring*

	Mass flow rates through pressure taps [x 10^{-5}kg/s] *(positive indicates inflow into the ring and negative indicates outflow from the ring into the pipe)*			
	$0°$ tap	$-90°$ tap	$90°$ tap	$-180°/180°$ tap
Small ring				
Re = 50,400	4.9	1.1	1.1	-7.1
94,100	9.2	2.1	2.1	-13.4
201,500	19	4.2	4.2	-27.4
Large ring				
Re = 50,400	8.7	1.5	1.5	-11.7
94,100	16.4	2.9	2.9	-22.2
201,500	34.6	6.3	6.3	-47.2

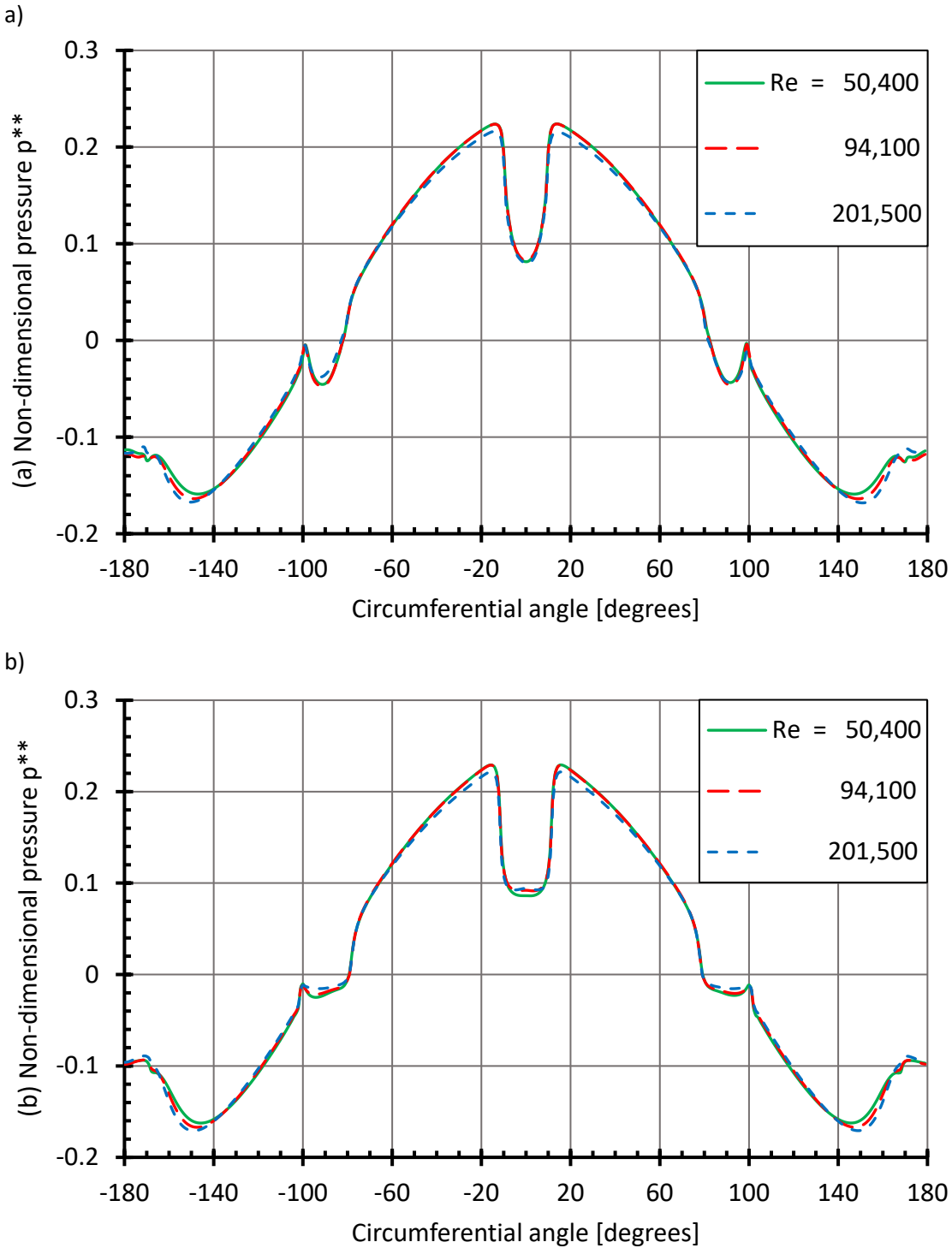

Fig. 3.6 *Circumferential variation of the dimensionless pressure p** at the inner bounding wall of the pipe at the exit of the bend in the presence of the piezometer ring (a) the smaller-diameter piezometer ring and (b) the larger-diameter piezometer ring*

3.7 Pipe longitudinal pressure variations for the with-ring case

Of particular practical relevance is the concern that the presence of the ring might affect the pressure drop between the pipe-inlet and bend-exit cross sections. To this end, cross-sectional average pressures were computed at both the pipe inlet and bend exit. This information is used in the presentation in Fig. 3.7, where the non-dimensional pressure drops between the aforementioned cross sections are plotted as a function of the duct Reynolds number.

As expected, the smallest pressure drop among those exhibited corresponds to the absence of a piezometer ring, while the largest pressure drop occurs when the small ring is in place. The pressure drop that corresponds to the large ring in place is intermediate. That the small ring causes the largest of the pressure drops can be attributed to the fact that smaller diameter tubing gives rise to larger pressure drops than does larger diameter tubing.

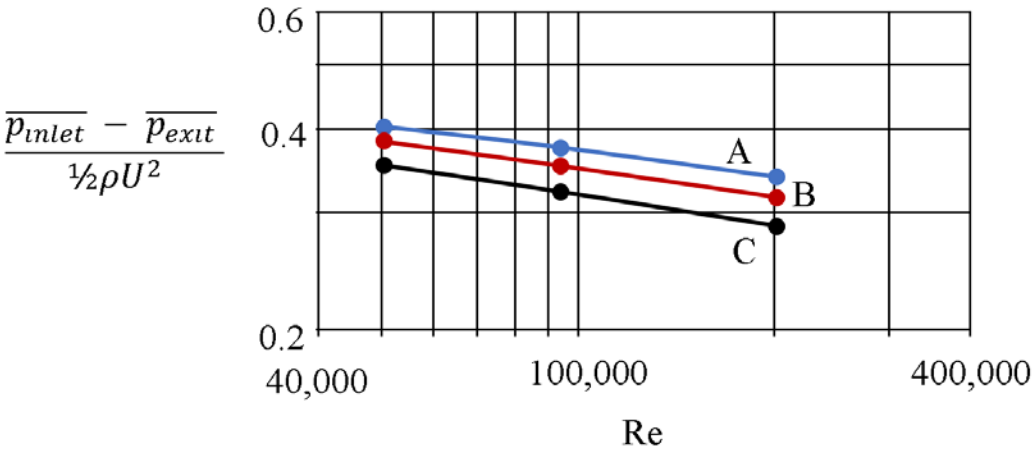

Fig. 3.7 *Non-dimensional pressure drop between the pipe-inlet and bend-exit cross sections. A: smaller ring, B: larger ring, and C: no ring.*

The power-law relationships that connect the dimensionless pressure drop with the Reynolds number are

$$A: \frac{\overline{p_{inlet}} - \overline{p_{exit}}}{\frac{1}{2}\rho U^2} = 1.565 Re^{-0.125} \tag{3.8}$$

$$B: \frac{\overline{p_{inlet}} - \overline{p_{exit}}}{\frac{1}{2}\rho U^2} = 1.724 Re^{-0.139} \tag{3.9}$$

$$C: \frac{\overline{p_{inlet}} - \overline{p_{exit}}}{½\rho U^2} = 1.833Re^{-0.152} \quad (3.10)$$

The percentage increases in the pressure drop between the pipe-inlet and bend-exit cross sections due to the presence of the small piezometer ring are: 13% for Re = 50,400, 15% for Re = 94,100, and 17% for Re = 201,500. While these pressure drop increases are moderate, they may be sufficient to be noteworthy for practical design. With regard to the larger piezometer ring, the increase in pressure drop with respect to no-ring case are: 8% for Re = 50,400, 9% for Re = 94,100, and 10% for Re = 201,500.

3.8 Tap-off locations on the ring for pressure measurements

A motivation for the use of a piezometer ring is to provide a means of determining the average pressure in a flow cross section. Up to the present, there has been no quantitative assessment tool to judge the best tap-off location to fulfill this objective. Figures 3.8 and 3.9 have been prepared to assist in the decision of where to position the tap-off location. The first of these figures corresponds to the smaller ring and the second to the larger ring. The information conveyed by these figures is the circumferential pressure distributions on the *outermos*t *edge of the piezometer ring*. The reason for this choice of pressure tap-off location is that in all likelihood, that would be the most convenient for tap installation. The information plotted in Figs. 3.8 and 3.9 is the dimensionless pressure distribution in terms of the p^{**} variable that was defined in Eq. (3.7). This quantity conveys the difference between the local circumferential pressure p and the area-averaged pressure $\overline{p_{exit}}$ in the flow cross section of the pipe. Clearly, the choice of a tap-off location would correspond to any point at which p^{**} is equal to zero. The information conveyed in Figs. 3.8 and 3.9 should be viewed with respect to this condition.

Inspection of Figs. 3.8 and 3.9 shows that the use of the non-dimensional pressure p^{**} is successful in bringing together the results for the various investigated Reynolds numbers. In addition to the curves for the circumferential p^{**} results, each figure includes a horizontal line corresponding to $p^{**} = 0$. Wherever the circumferential distributions of p^{**} cross the horizontal reference line, that point is a candidate location for a tap-off.

However, it is necessary to recognize that pressure taps have some circumferential span and this reality must be considered. Another consideration is the manner in which the curve representing the circumferential variation of p^{**} crosses the reference line. Note from Figs. 3.8 and 3.9 that a given crossing is actually defined by adjacent local upward and downward branches of the p^{**} curve. If the angular spacing between the two adjacent branches spans several degrees of angle, the outcome might not a crisp location for a take-off tap. In general, the desired $p^{**} = 0$ condition should be confined to a narrow span of the take-off tap.

Clearly, in Fig. 3.8, tap locations at ±50° are attractive tap-off locations. In contrast, the locating of taps at ±10° and at ±95° may lead to significant errors. With regard to Fig. 3.9, taps at $\pm 95^{o}$ should yield good results, whereas taps at $\pm 10^{o}$ might yield errors.

The foregoing discussion is noteworthy in another sense: that is, that only two tap locations on the ring appear to be viable for pressure take-off. Furthermore, the intuitive tendency to use taps at 0, 90, 180, and 270° appears to be incorrect. These findings tend to invalidate the four-tap proposal made by Blake [11]. The Blake recommendation, although couched in the clothing of analysis, is not based on fluid- mechanic reality.

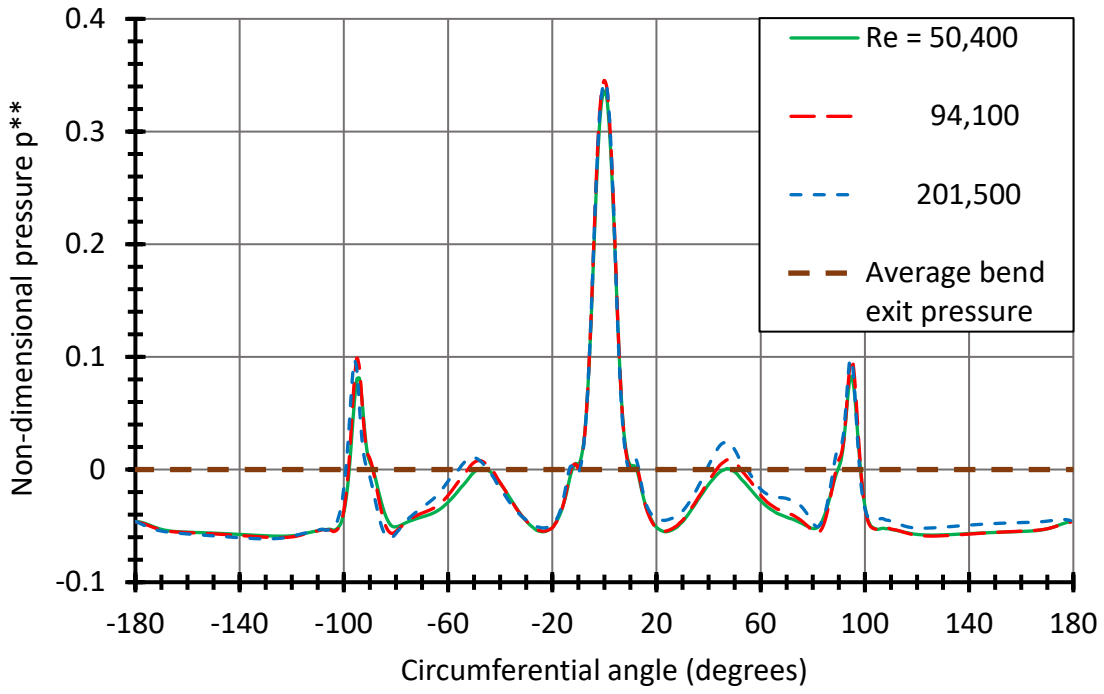

Fig. 3.8 *Circumferential pressure p** variation along the outermost boundary of the smaller piezometer ring*

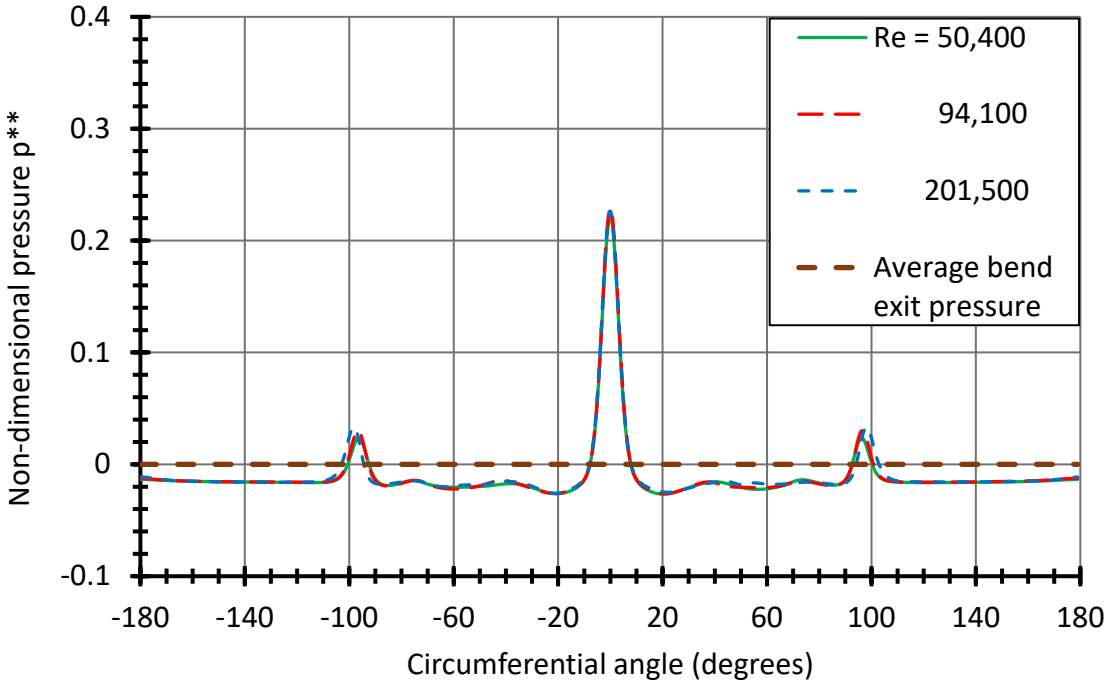

Fig. 3.9 *Circumferential pressure p** variation along the outermost boundary of the larger piezometer ring*

3.9 Turbulence intensities

As a relevant part of the fluid-mechanic analysis, turbulence intensities have been extracted from the numerical solutions. For this purpose, the turbulent viscosity μ_{turb} will be used as a measure of the intensity. The magnitude of this quantity will be quantified by the dimensionless ratio μ_{turb}/μ, where μ is the absolute viscosity. Highly turbulent flows are characterized by this ratio attaining magnitudes of several hundreds. Even a ratio of 1.0 indicates that turbulence is present and is moderately important. Although turbulence intensity plots were made for all the three investigated Reynolds numbers, the differences among them , except for the magnitude of the turbulence, were seen to be so slight that the display of a representation figure for the intermediate Re = 94,100 was thought to be sufficient.

In Fig. 3.10, μ_{turb}/μ is plotted as a function of x/D along the axis of the pipe for Re = 94,100. The exit of the bend is at x/D = 13. The issue that is relevant to the present study is the effect of the presence of the piezometer ring on the ratio. That presence is seen to cause a discernible increase in the turbulence just downstream of the bend exit. Also, at that location, the strength of the turbulence is seen to be slightly different for the smaller and larger rings, and the intensity in the absence of the ring also increases, but not as rapidly as when the ring is present Notwithstanding any minor perturbations, it is clear that the present results are clearly applicable to turbulent flows since $\mu_{turb}/\mu \gg 1$ everywhere. As a final note, it may be of some interest to show how the μ_{turb}/μ ratio depends on the Reynolds number. For the successive Reynolds numbers of 50,400, 94,100, and 201,500, the corresponding maximum values of μ_{turb}/μ are 205, 350, and 790.

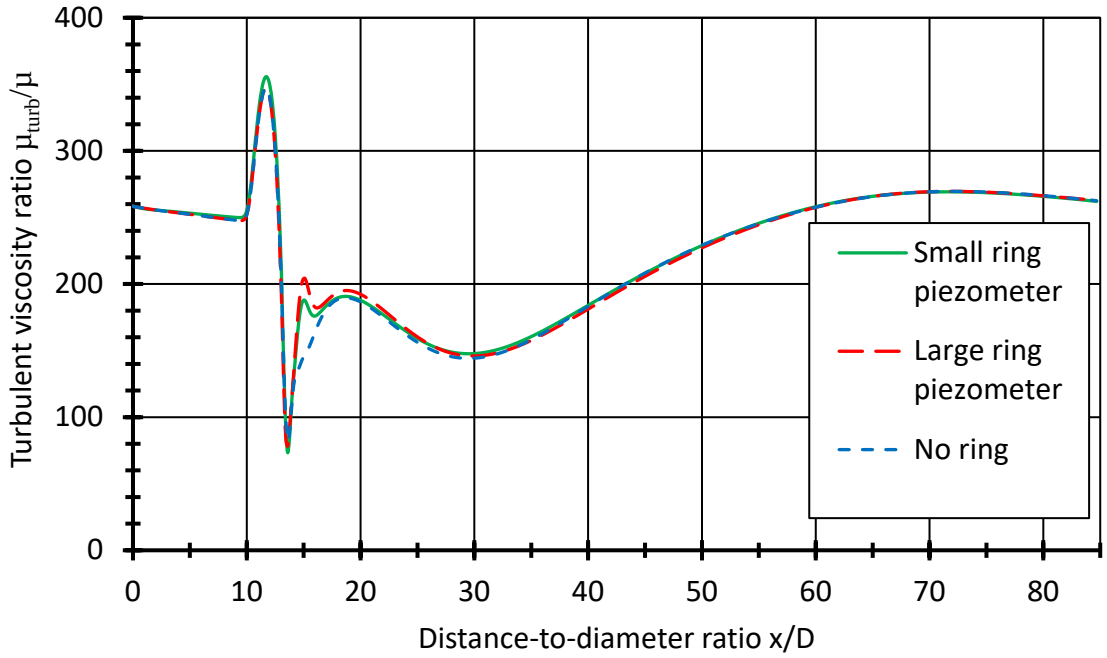

Fig. 3.10 *Axial distribution of the turbulence intensity along centerline of the pipe for Re = 94,100. The exit of the bend and the location of the piezometer ring are at x/D = 13.*

Since the diameter of the radial spokes that interconnect the pipe proper to the piezometer ring is much smaller than the pipe diameter, there might be reason to expect that the μ_{turb}/μ ratio might be smaller for the fluid passing through the former. The same concern relates to the ring itself. To assess this issue, Fig. 3.11 has been prepared. The figure corresponds to the lowest of the investigated Reynolds numbers and is, therefore, most sensitive to possible laminarization. That figure enables a clear comparison to be made of the values of the μ_{turb}/μ ratio in the pipe, in the interconnecting spoke, and in the ring. The ordinate of the figure is the magnitude of the ratio, while the abscissa is the radial distance starting at the pipe axis and running radially outward to the outer wall of the ring. The radial line being considered is at the angular position of 180°.

Inspection of Fig. 3.11 shows that the most intense turbulence occurs at the pipe axis. The intensity at first diminishes with radial distance from the axis and then humps up to a local maximum which may be due to the pinching together of the fluid entering the spoke. When the point of observation enters the interconnecting spoke, the intensity rises not unexpectedly since the in-spoke velocities are elevated. Another maximum is

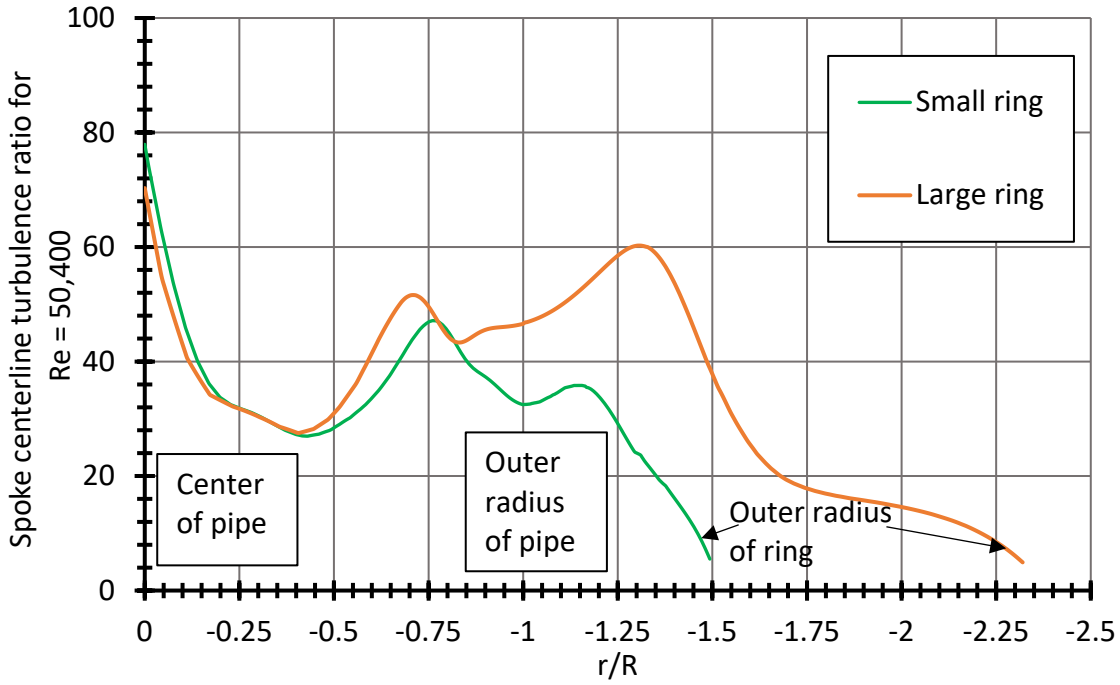

Fig. 3.11 *Variation of μ_{turb}/μ along a radial line from the pipe centerline to the outer wall of the ring at angle 180°. Re = 50,400.*

encountered when the spoke encounters the ring. Thereafter, the intensity decreases in the direction of the outer wall of the ring. Aside from the near neighborhood of the outer wall of the ring, the μ ratio exceeds 20 and has a maximum value of approximately 75. However, in the outer wall neighborhood, μ_{turb}/μ drops to a lowest value of approximately five. That value still indicates that turbulence is dominant, but to a lesser extent than at other locations in the cross section.

To examine the issue of whether or not the μ_{turb}/μ ratio takes on even lower values at any location in the ring, a thorough survey of the values of the ratio at all circumferential stations within the ring. That survey was made at three radial positions spanning the diameter of the ring. It was found that for both rings, the minimum value of μ_{turb}/μ was found to be approximately five. This outcome adds further support to the use of a turbulence as was done here.

3.10 Concluding remarks

The research described in this paper is believed to constitute the first attempt to investigate and understand the fluid mechanics of the interactions of piezometer rings with the piping systems to which they are attached. From the literature review conveyed in the Introduction, it is clear that piezometer rings are frequently encountered in engineering practice as an aid to pressure measurement. . On the other hand, a retrospective review of that literature gives rise to some fundamental doubts about whether the use of such instrumentation was performed in a manner that took proper cognizance of the participating fluid-mechanic phenomena.

One of these concerns is whether there was a true need for making use of piezometer rings in the cited applications. In particular, in not one of the applications did the geometry of the flow passage give rise to large circumferential pressure variations. Certainly, in none of the referenced literature citations were the circumferential pressure variations as large as those due to a pipe bend as encountered here. The second concern is the absence of any rational approach to the choice of the optimum tap-off location on the ring circumference for capturing the mean pressure of the flow and conveying it to a proper measurement instrument. Indeed, none of the references made any mention of a tap-off location.

The perspective set forth in the preceding paragraphs is the need for a fundamental fluid-mechanic analysis to expose the complex participating physical phenomena. The use of piezometer rings seems to have a life of its own despite the lack of a full understanding of the phenomena involved. The plan of the present work is to perform a deep fundamentals-based analysis that can also serve others who are more dedicated to the use of piezometer rings as an experimental tool.

The physical model that underlay the numerical simulations used to quantify the piezometer-ring fluid mechanics was free of accuracy-compromising assumptions. The model was based on turbulent flow, and an *a posteriori* analysis of the magnitude of the

turbulent viscosity results supported this choice. To assure an accurate representation of the circumferential pressure variations at the bend exit, painstakingly implemented numerical solutions of the fluid flow in the entire piping system, including the bend, were performed both in the presence and in the absence of the piezometer ring.

Two independent variables were taken into account during the course of the investigation. One of these was the pipe Reynolds number which ranged from approximately 50,000 to 200,000. The other was the geometry of the piezometer ring. Two rings, both of similar form but with different dimensions, were investigated. Each ring consisted of four radially deployed short lengths of circular tubing which connect the pipe proper to a circular tube that rings the pipe. The interconnections between the pipe and the ring were situated at 90^o intervals around the circumference of the pipe. Two of these locations respectively corresponded to the highest and lowest values in the circumferential pressure distribution, while the other two locations were at intermediate locations. These deployments coincided with standard practice as reported in the literature.

With regard to the results, major focus was directed to three issues: (a) the optimal circumferential locations of the radial bridges (spokes) connecting the pipe and the ring, (b) the optimal circumferential locations of take-off lines which enable accurate measurement of the pressure of the fluid flow in the pipe, and (c) the pressure drop penalty, if any, incurred by the use of a piezometer ring. The use of four equally spaced pipe-to-ring bridges that encompassed the entire maximum-to-minimum circumferential pressure variation provided at least two candidate locations for the optimal positioning of a take-off line.

For the clear specification of these optimal take-off positions, the outside of the bend was described to be at the 0^o angular position and the inside of the bend was at the $\pm 180^o$ angular position. For the smaller piezometer ring, optimum pressure take-off occurred at angles of $\pm 50^o$ whereas for the larger piezometer ring, pressure take-off at $\pm 95^o$ was the most advantageous. The pressure drop between the pipe inlet and the bend exit was seen

to increase due to the presence of the ring. For the smaller ring configuration, the increase relative to the no-ring pressure drop was on the order 15%. The pressure drop increase due to the presence of the larger ring configuration was about 10%.

CHAPTER FOUR

Heat Transfer Effects of Axis-switching of Two-dimensional Rectangular Jets Impinging on Flat Plates

4.1 Introduction

One of the most efficacious means of transferring heat is by jet impingement. This method is commonly found in the thermal management of electronic equipment. There is a rich literature that deals with the heat transfer characteristics of jet impingement. That literature may be subdivided according to the details of the jet's fluid mechanics. It is well understood that a jet is created by a fluid flow exiting from a nozzle, pipe, or rectangular slit into a space within which there is a target surface whose thermal state is to be managed. One category of jets is termed a submerged jet in which the jet fluid is identical to that in the space into which the jet empties. Another category is termed a confined jet wherein the space has confined boundaries which tend to focus the trajectory of the jet. All of these situations are encountered in practice. When a jet impinges at normal incidence on a plane surface, the fluid may turn sharply and continue its flow along and parallel to the surface. That situation is termed a wall jet.

Of particular interest here are submerged air jets which are unconfined and are free to develop during their course of flow throughout a free space. Somewhere in that space is a target plate whose axis is aligned with the original axis of the jet at its origin. The creation of the jet as treated here is somewhat unique. In the published literature, most jets are envisioned as being initiated at the exit of a nozzle, a pipe, or a rectangular slit. There is virtually no attention given to the upstream history of the fluid which passes through those apertures. Here, the fluid which ultimately emerges as a jet initiates its flow at the inlet of an upstream rectangular duct. After traversing the length of the duct, the fluid contracts slightly in order to pass through a rectangular slit in a plate which caps the downstream end of the duct. Upon passing through the slit, the fluid emerges into a free

air space without confinement. It continues traversing the space until it impinges on a target plate whose distance from the slit is variable.

It has been demonstrated by many authors [24-28] that during its time of flight between the slit and the impingement plate, the cross-sectional shape of the jet may evolve from a pure rectangle mirroring the slit geometry to a circular cross section or an intermediate shape upon impingement. This phenomenon has been termed jet-axis switching. Those studies were confined totally to fluid mechanic issues.

To the author's best knowledge, Gorman [29] is the only reference in which heat transfer in the presence of jet axis-switching has been investigated. His work was confined to relatively low Reynolds numbers, the largest being 1,100, where the definition of the Reynolds number was based on the short dimension of the rectangular slit and the mean velocity of the fluid passing through it. The Reynolds numbers of Gorman are generally lower than most of the practical applications where jet impingement plays a major role. Here, the investigated Reynolds numbers range from 11,000 to 88,000. Another key variable is the aspect ratio of the slit, which is the ratio of the long to the short dimension. That aspect ratio was selected here to be 10 in order to ensure that the studied jets would represent wide rectangular slots. With respect to the literature, many authors would classify a 10:1 jet as being two-dimensional.

A major focus of this work is heat transfer. The fluid emerging from the slit was assigned a given temperature different from that of the downstream impingement plate. The plate temperature was taken to be uniform. Among the heat transfer results, the distribution of heat flux on the surface of the impingement plate was determined as were local/average heat transfer coefficients. The impact of axis-switching on the distribution of heat flux on the impingement plate was displayed in detail. With regard to fluid flow, focus was directed to the axis-switching phenomenon with a view to determining how the switching is affected by the Reynolds number. Vector diagrams were used to display the pattern of fluid flow.

Although the literature on jet impingement heat transfer is very rich, it appears that there has been no prior identification of axis-switching playing a major role. This issue is of primary concern here.

4.2 Physical Situation

A pictorial schematic diagram of the situation to be considered in this chapter is displayed in Fig. 4.1. As seen there, a fluid (air) enters a flat, rectangular duct and traverses the full length of the duct, exiting through a narrow slit in a plate that caps the downstream end. The flow undergoes a moderate contraction at the duct exit because the

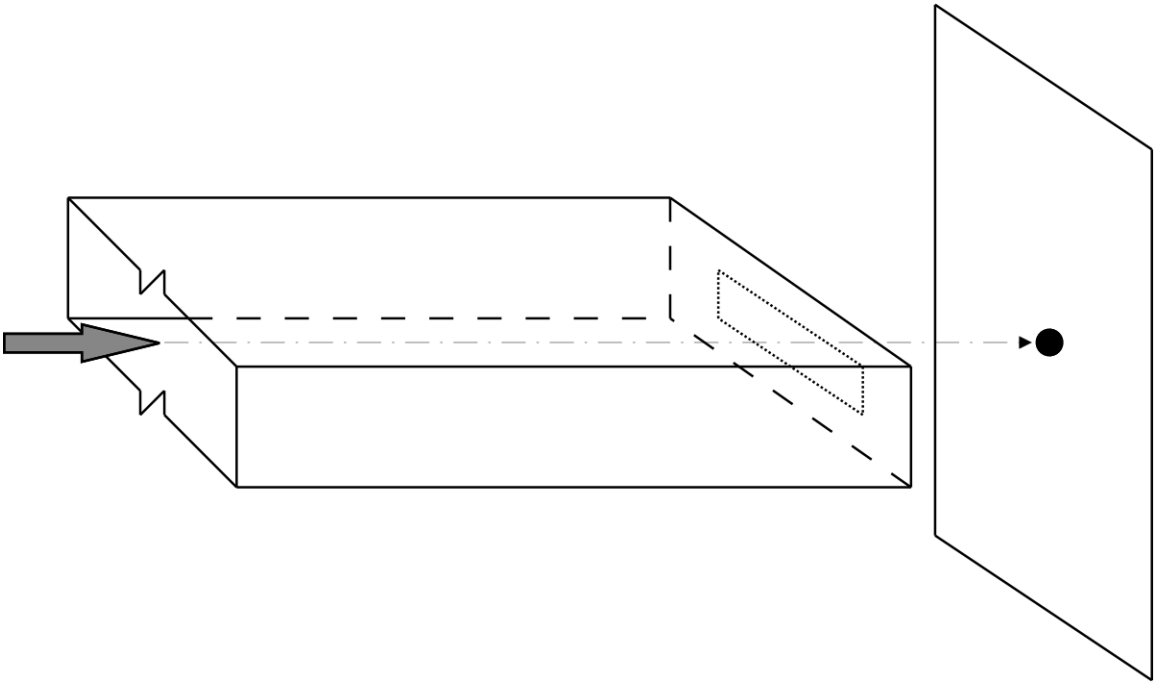

Fig. 4.1 *A pictorial schematic diagram of the physical situation to be considered in this chapter*

slit cross-sectional area is smaller than the duct cross section. After passing through the slit, the air exhausts into an unconfined space. At the downstream end of the space, a target plate is positioned at an assigned distance from the exit of the duct. The plate temperature is maintained at a uniform value that is different from the temperature of the impinging air. This situation is a prototype of numerous cooling applications encountered in practice. The specific situation displayed differs from many others dealt with in the

literature in that the space into which the jet exits is unconfined. In contrast, the bulk of the literature deals with coolant jets entering confined spaces.

Detailed diagrams featuring the exit plane of the emerging jet are conveyed in Figs. 4.2, (a) and (b). In Part (a), the geometrical variables are displayed whereas Part (b) shows the coordinates. Note that the *x*-coordinate lies in the streamwise direction and coincides with the axis of the flow as it emerges from the rectangular duct, and it is that coordinate which will be used to define the distance between the jet exit position and the target plate.

Of special note is the aspect ratio a/b of the slit which defines the initial geometry of the emerging jet. This aspect ratio was held fixed at a value of 10 with the dimensions a and b fixed at 20 cm and 2 cm respectively.

The solution methodology to be employed here is numerical simulation. In that regard, a necessary first step is to define the space in which the solution is to be obtained. That space is commonly termed the solution domain. Figures 4.3, (a) and (b), are used to display the solution domain, respectively in a side view and in a pictorial view. The solution domain is delineated in both the (a) and (b) parts of the figure by means of dashed lines.

Attention will first be focused on Part (a) which may be regarded as a side view of the solution domain. From the figure, it is seen that the solution domain extends the entire length of the interior of the delivery duct and also encompasses a large volume in the free space into which the jet emerges. Note that the exterior boundary of the solution domain extends backward from the plane of emergence of the jet. This backward extension was prompted by the recognition that air entrained by the jet could activate fluid motion adjacent to the outside of the duct. The downstream boundary of the solution domain is defined by the front face of the target plate. Since the position of the target plate with respect to the jet exit is one of the variables of the study, the extent of the solution domain downstream of the jet-exit plane will vary accordingly.

(a)

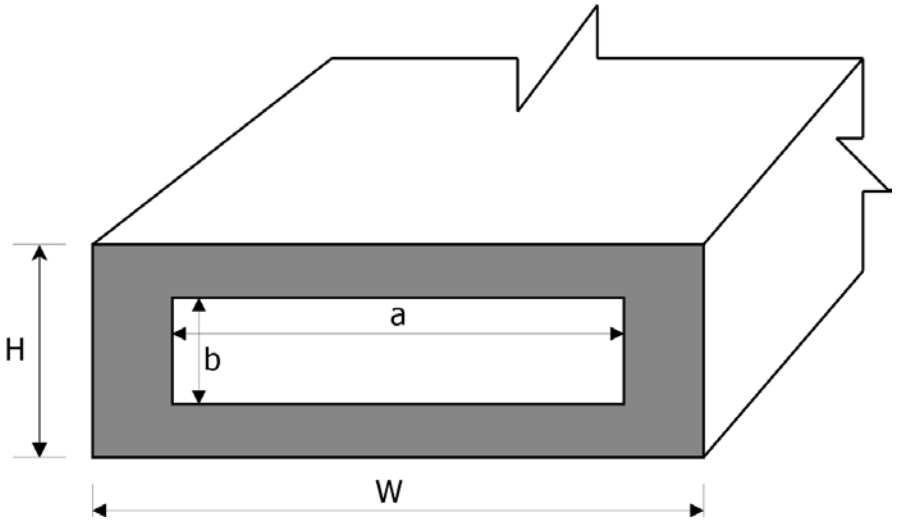

(b)

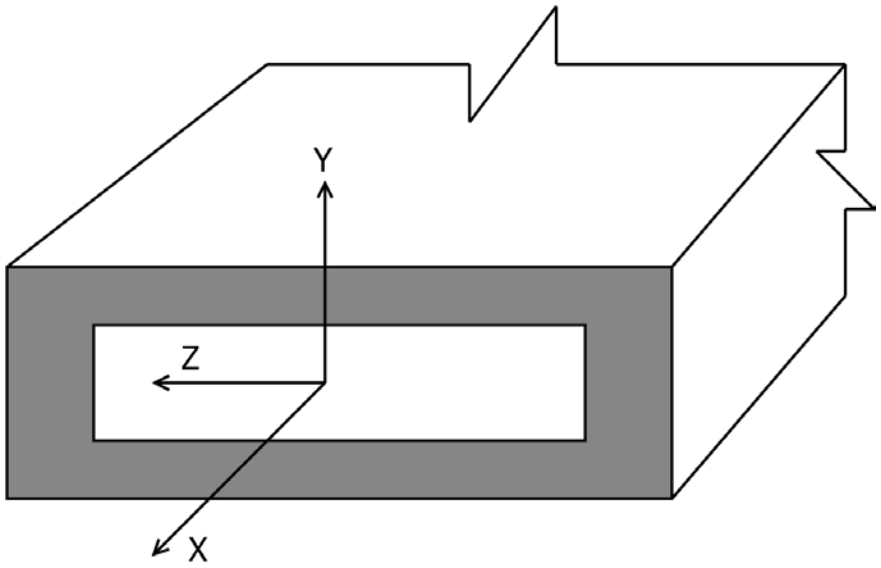

Fig. 4.2 *Details of the slit at the exit plane of the emerging jet: (a) geometrical notation and (b) coordinates*

(a)

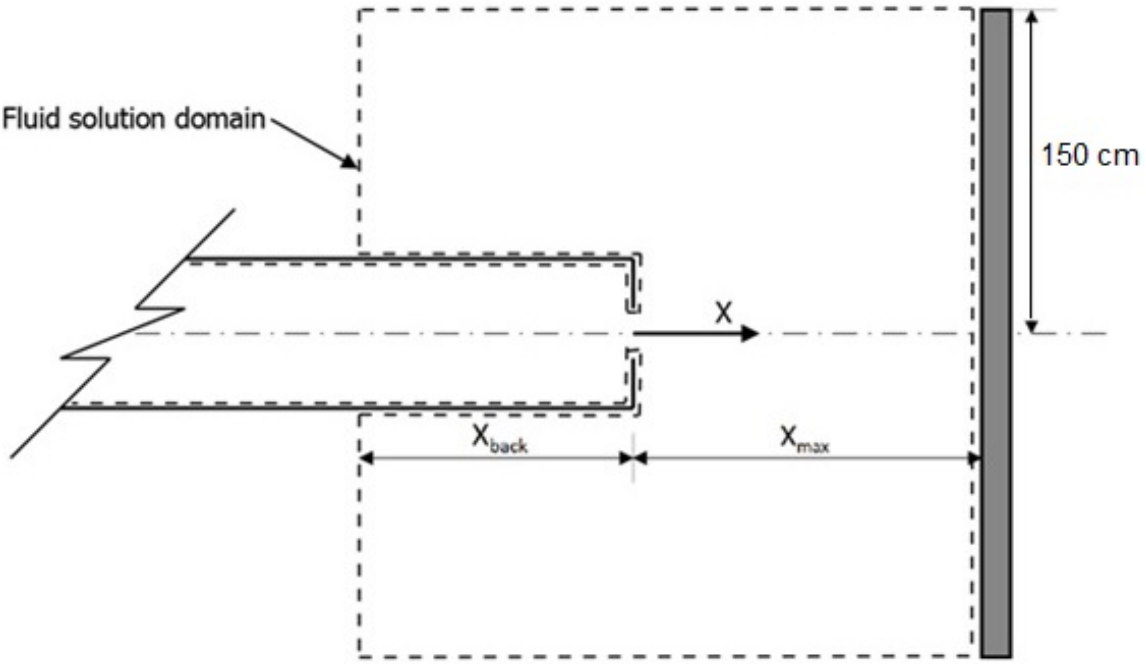

(b)

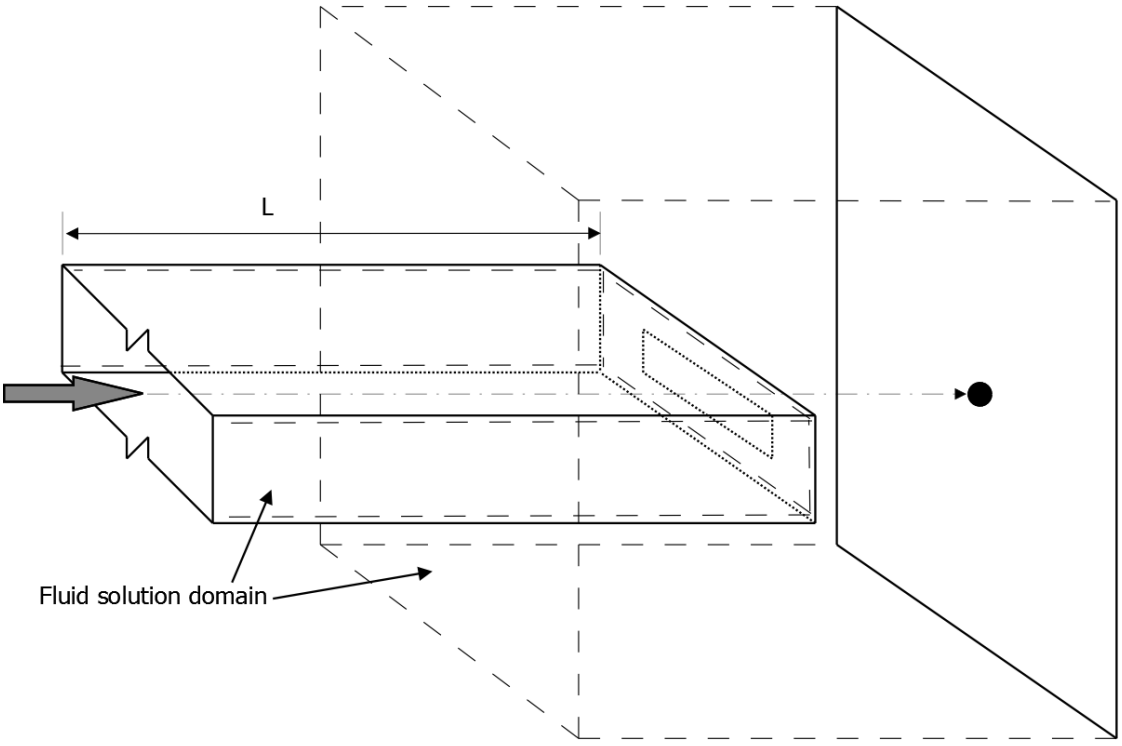

Fig. 4.3 *Views of the solution domain: (a) two-dimensional side view, (b) three-dimensional pictorial view*

Part (b) of Fig. 4.3 shows a three-dimensional pictorial view of the solution domain. Note that the figure is not to scale. In particular, the height of the slit is, in actuality, 1% of the height of the impingement plate. The distance L, the streamwise length of the duct, was not varied throughout the various stages of the solutions. The ratio of the duct length L to the duct height H (Fig. 4.2(a)) is 60. That ratio was chosen to ensure that the duct flow was fully developed prior to the exit plane. Another fixed geometric ratio is the duct aspect ratio W/H whose value is chosen to be 4.5, with H fixed at 5.33 cm and W at 24 cm.

4.3 Numerical Simulation Model

The model of the problem under consideration involves the implementation of several basic laws of conservation. The first of these is momentum conservation. If the flow is turbulent, the mathematical statement of momentum conservation is termed the RANS equations (Reynolds-Averaged, Navier-Stokes). These equations, written in Cartesian tensor form are

$$\rho\left(u_i\frac{\partial u_j}{\partial x_i}\right) = -\frac{\partial p}{\partial x_j} + \frac{\partial}{\partial x_i}\left((\mu+\mu_t)\frac{\partial u_j}{\partial x_i}\right) \quad i = 1,2,3 \;\; j = 1,2,3 \tag{4.1}$$

in which μ_t is called the turbulent viscosity. This quantity is not a material property as is the viscosity μ. Rather, it is a concept of convenience defined as

$$-\rho\overline{u_i'u_j'} = \mu_t\frac{\partial u_j}{\partial x_i} \tag{4.2}$$

Since the RANS equations do not conserve mass, it is necessary to include an equation, termed the equation of continuity, to achieve mass conservation. The continuity equation is

$$\frac{\partial u_i}{\partial x_i} = 0 \tag{4.3}$$

To complete the specification of the governing equations, it is necessary to choose a turbulence model for the evaluation of μ_t. There are numerous two-equation turbulence models that are used in connection with RANS equations. Not all of these equations are equally suitable for the specific physical phenomena that are involved with a given situation. In the present situation, there is a duct flow and a swirl associated with the axis-switching. It has been shown that the SST k-ω model performs very well for flows encompassing these features [3-6], and it has been chosen for application here.

The equations of the SST model are

$$\frac{\partial(\rho u_i \kappa)}{\partial x_i} = P_\kappa - \beta_1 \rho \kappa \omega + \frac{\partial}{\partial x_i}\left[\left(\mu + \frac{\mu_{turb}}{\sigma_\kappa}\right)\frac{\partial \kappa}{\partial x_i}\right] \tag{4.4}$$

$$\frac{\partial(\rho u_i \omega)}{\partial x_i} = A\rho S^2 - \beta_2 \rho \omega^2 + \frac{\partial}{\partial x_i}\left[\left(\mu + \frac{\mu_{turb}}{\sigma_\omega}\right)\frac{\partial \omega}{\partial x_i}\right] + 2\rho(1 - F_1)\frac{1}{\sigma_{\omega 2}\omega}\frac{\partial \kappa}{\partial x_i}\frac{\partial \omega}{\partial x_i} \tag{4.5}$$

The solution of Eqs. (4) and (5) yields the values of κ and ω, which give the turbulent viscosity μ_t from

$$\mu_t = \frac{\alpha \rho \kappa}{\max(\alpha\omega, SF_2)} \tag{4.6}$$

The symbols that appear in the foregoing equations are defined as

A	model constant
F_1, F_2	blending functions in the SST model
P_k	production term for the turbulent kinetic energy
S	absolute value of the shear strain rate
u	local velocity
x_i	tensor coordinate direction
α	SST model constant
β_1, β_2	SST model constants0

ω	specific rate of turbulence dissipation
κ	turbulent kinetic energy
μ	molecular viscosity
μ_t	turbulent viscosity
σ	diffusion coefficient
ρ	fluid density

The heat transfer problem is governed by the First Law of Thermodynamics in conjunction with the Fourier Law of Heat Conduction. For incompressible, constant property, turbulent flow, the First Law can be written as

$$\rho c_p \frac{\partial (u_i T)}{\partial x_i} = \frac{\partial}{\partial x_i}\left[(k + k_t)\frac{\partial T}{\partial x_i}\right] \tag{4.7}$$

in which T is the fluid temperature and c_p and k are, respectively, the constant-pressure specific heat and thermal conductivity of the fluid. The quantity k_t is designated as the turbulent thermal conductivity. Its value is closely linked to that of the turbulent viscosity by means of the turbulent Prandtl number

$$Pr_t = \frac{c_p \mu_t}{k_t} \tag{4.8}$$

Extensive experience [30, 31] has shown that a constant value of $Pr_t = 0.85$ gives rise to highly accurate heat transfer results.

The specification of the boundary conditions on the surfaces of the solution domain are a necessary ingredient of the problem definition. In selecting the solution domain, it is important to avoid constraining the natural motions of the domain. In addition, the selection should take account of inherent symmetries of the problem in question. For the situation of interest here, the symmetries are such that only a quarter of the total geometry need be identified as being included in the solution domain. The selected solution domain that defines the quarter-symmetry feature is pictured in Fig. 4.4. Note that many of the boundaries that are seen in Fig. 4.4 are actually symmetry planes.

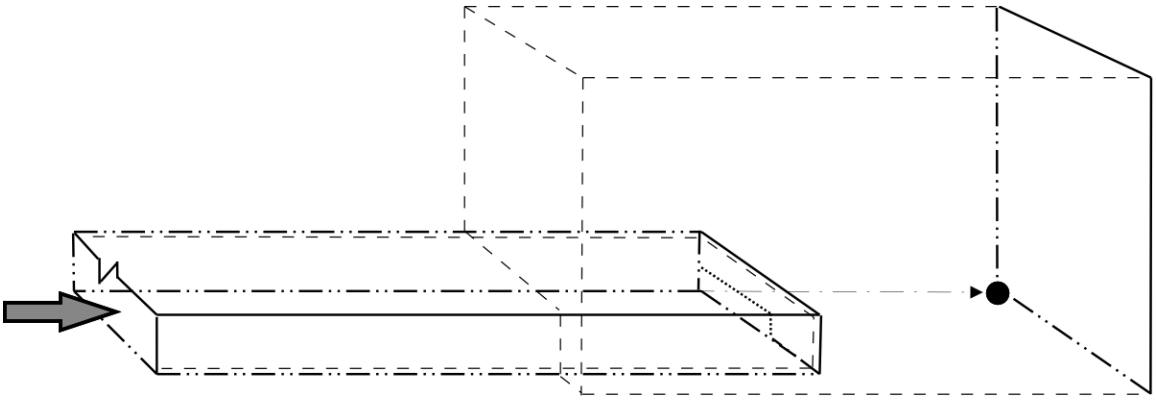

Fig. 4.4 *Pictorial view of the solution domain chosen for the numerical simulation. The domain is a quarter of the total geometry in which fluid motion exists.*

With regard to the velocity boundary conditions, on all solid surfaces the velocity is zero, both normal and tangential to the plane of the surface. At the duct inlet cross section, the velocity is uniform and its magnitude is specified. Since the work is performed in a dimensionless context, it is convenient to specify the inlet velocity magnitude in terms of a Reynolds number of the slit, which is defined as

$$Re_{slit} = \frac{\rho U_{slit} b}{\mu} \tag{4.9}$$

In this equation, U_{slit} is the mean velocity of the fluid passing through the slit, and *b* is the height of the slit pictured in Fig. 4.2(a). The numerical solutions were executed for values of the slit Reynolds number of 11,000, 22,000, 33,000, 55,000, and 88,000. Using the values of H and W to calculate D_h, the hydraulic diameter of the duct, the duct Reynolds numbers are calculated to be in the range of 161,315 – 1,290,512 for the aforementioned range of slit Reynolds numbers. The inlet to the duct was assigned a 'zero gradient' turbulence intensity. Based on ANSYS documentation, the turbulence intensity can be measured using the formula

$$I = 0.16\, Re_{Dh}^{-1/8} \tag{4.10}$$

Based on the above formula, turbulence intensities are the inlet appear in the range of 2.7 - 3.5 %. Another parametric variation to be specified is the value X_{max} (see Fig. 4.3(a))

which defines the distance between the jet egress and the target plate. For symmetry boundaries, the normal derivatives of all velocity components are zero and the component of velocity that is perpendicular to the plane is zero whereas the other component is parallel to the plane.

With regard to the heat transfer solutions, they were carried out for a value of the Prandtl number $Pr = 0.7$. The heat transfer boundary conditions are: (a) temperature T_i of the fluid at the inlet of the duct, (b) all surfaces of the duct and the slit are adiabatic, (c) uniform temperature T_t of the target plate, (d) on symmetry planes, there is no heat transfer, and (e) at an outflow boundary, the streamwise second derivatives of all of the dependent variables are zero.

There is another type of surface which is frequently encountered in numerical simulation work. It is called an *opening.* This type of surface designation is appropriate when it is not known whether fluid passes inward or outward across the surface. When an opening is designated, fluid may flow either in or out through that surface. The specification of an opening requires an additional choice: (a) whether the fluid crossing the surface is perpendicular to it or (b) whether the fluid is carried across the boundary by entrainment. Regardless of whether options (a) or (b) is selected, it is necessary to prescribe the pressure at the opening. For the heat transfer boundary condition at an opening, if fluid is flowing out of the solution domain through the opening, the standard aforementioned temperature outflow boundary condition is applied. If, on the other hand, fluid is passing into the solution domain through the opening, the temperature is specified as being that of the fluid that is being carried into the domain.

4.4 Numerical Considerations

The numerical simulations were implemented with the aid of ANSYS CFX 16.1 software. The software performs the discretization of the governing partial differential equations described earlier in this chapter by means of the finite-volume method. Meshing of the solution domain has a major effect on the accuracy of the solutions. As a consequence, great care was taken in the meshing process. In particular, a mesh-

independence study was carried out. For a fixed size of the solution domain, solutions were run with various numbers of nodes. For each such computer run, the total rate of heat transfer at the impingement plate was recorded. The number of nodes was increased systematically until the numerical value of the total rate of heat transfer was independent of the node number to within 0.2%. Since the extent of the solution domain varied as a function of the position of the target plate, so too did the number of nodes. For the largest separation distance between the jet exit and the target plate $X_{max}/b = 30$, the mesh consisted of approximately 20 million nodes.

4.5 Fluid Flow Results and Discussion

One of the fluid flow results to be presented include displays of the extent of the velocity field as a function of the separation distance between the jet exit and the target plate. A number of cross sections in the space between the jet exit and the plate were selected and bookmarked, and in each cross section, the velocity field was displayed by a color contour diagram. The goal of this presentation is to identify the changing geometry of the jet as it passes through the free space and, in particular, to clearly demonstrate the presence of the jet axis-switching at the relatively high Reynolds numbers that characterized this work.

Another fluid flow result is focused on showing details of the flow field by means of vector diagrams. Two forms of vector diagrams will be used to provide a complete display. In one of these forms, denoted as normalized, all of the vectors are of the same length, with the outcome being a clear description of the flow directions. In contrast, the other form of vector diagram can be designated as un-normalized. In such diagrams, the lengths of the vectors are proportional to the local magnitude of the velocity. The two types of vector diagrams, taken together, provide both magnitudes and directions of the local flow field.

Jet Evolution

The jet evolution information will be reported in Figs. 4.5, 4.6, and 4.7, respectively for impingement plate locations of X_{max}/b = 10, 25, and 30. Each of these figures consists of a number of color contour diagrams of the velocity field. Those color contour diagrams are intended to unambiguously display the development of the jet as it passes through the space between the egress cross section and the target plate. The number of color contour diagrams for each figure correspond to the space between the egress plane and the target. If the target plate is at X_{max}/b = 10, color contour diagrams are displayed at x/b values of 2.5, 5, 7.5, and 9.5. At the other extreme, for the target plate at X_{max}/b = 30, the color contour diagram are conveyed at locations x/b = 2.5, 5, 10, 15, 20, and 25. It is believed that this display provides ample evidence of the mode of jet evolution.

Attention is first turned to Fig. 4.5, for which the target plate is at X_{max}/b = 10. The contour diagrams are arranged in four columns, with each column corresponding to a given Reynolds number and ranging from 11,000 to 55,000, left to right. Each row of the displayed diagrams corresponds to a different x/b plane. Note that in each contour diagram, there is a sharp black outline which depicts the geometry of the slit through which the jet emerges. In fact, the outline depicts one quarter of the total slit. Focus will first be directed to a given column (fixed Reynolds number) to observe the evolution of the jet with increasing distance from the plane of emergence. It can be seen that for any Reynolds number, the jet becomes thicker (taller) with increasing x/b but does not show any tendency toward widening. The thickening is more marked toward the outboard end of the jet, but the distance from the emergence plane is too short to show significant evolution to a drastically different shape.

Consideration is next turned to Fig. 4.6, where data is displayed for the target plate location X_{max}/b = 25. For this case, color contour diagrams are shown for x/b = 5, 10, 15, and 20. The enlarged space between the plane of emergence and the target plate enables further development of the jet compared with that displayed in Fig. 4.5. An overview of this figure clearly shows an extensive change in the shape of the jet cross section. Whereas the thickening of the jet is greatest at the outboard end for x/b = 5 and 10, there

is a shift in the evolution as witnessed by the contour diagrams for x/b = 15 and 20; for the latter, the jet appears to be round.

Figure 4.7 is the last of this set of figures and pertains to the target plate at X_{max}/b = 30 with graphical information displayed at x/b = 10, 15, 20, and 25. It is convenient to note that the contour diagram for x/b = 20 for Fig. 4.7 is hardly different from that x/b = 20 for Fig. 4.6. Focusing fully on Fig. 4.7, it is seen that there is continuing evolution of the jet cross section between x/b = 20 and 25. The observed growth of the jet in that range of x/b is clearly in the vertical direction, so that further growth that might occur as X_{max}/b were further increased would give rise to a jet shape which is vertically elongated in contrast to its initial horizontal elongation. This observation along with those enunciated in the preceding paragraphs lends strong support to the heightened importance of jet axis turning at higher Reynolds numbers. It will shortly be shown that this phenomenon has important heat transfer implications.

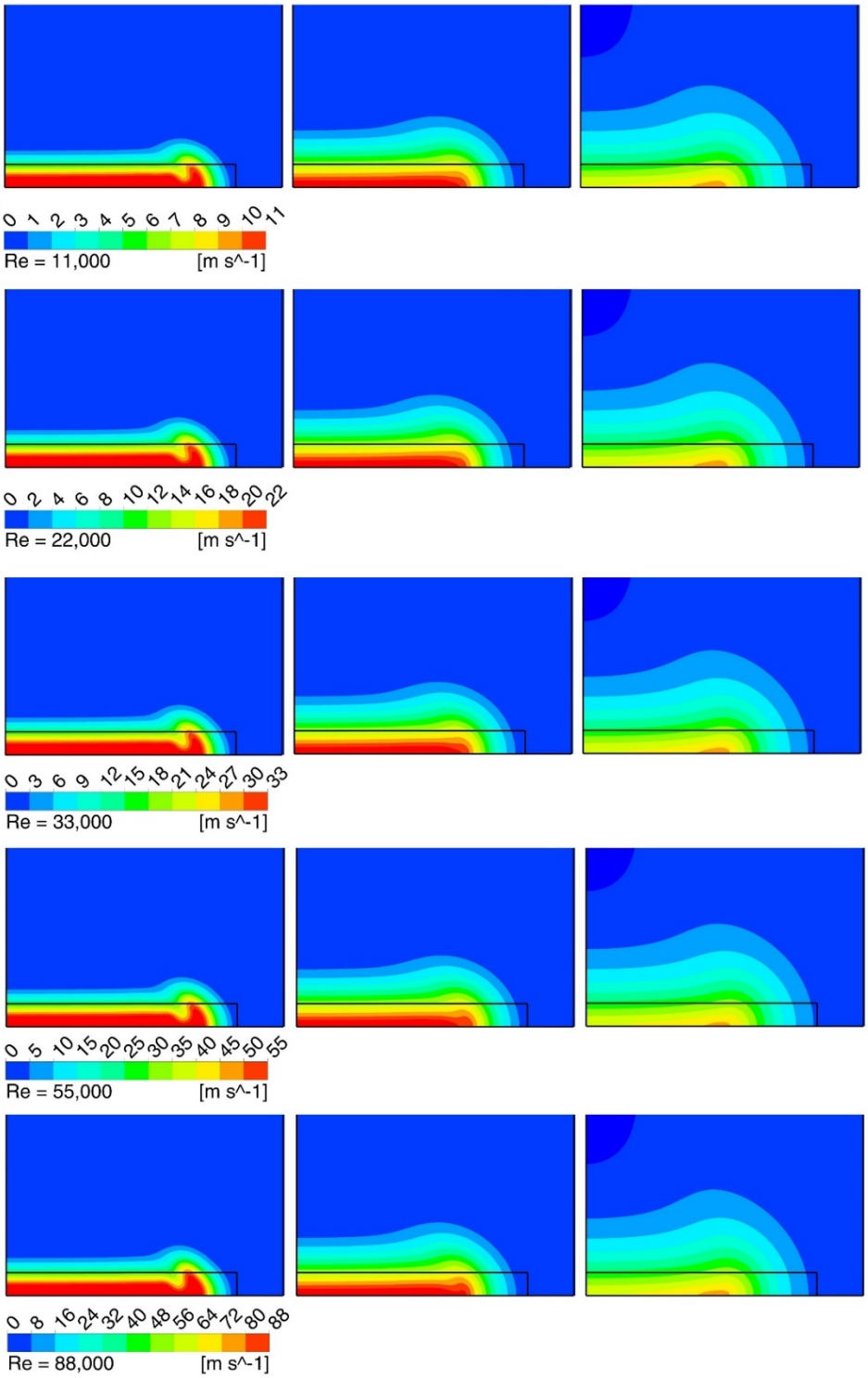

Fig. 4.5 *Color contour diagrams showing magnitudes of the perpendicular velocity in planes situated at x/b = 3, 6, and 9, respectively from left to right for the Reynolds numbers mentioned in the legend. The target plate is positioned at* $X_{max}/b = 10$

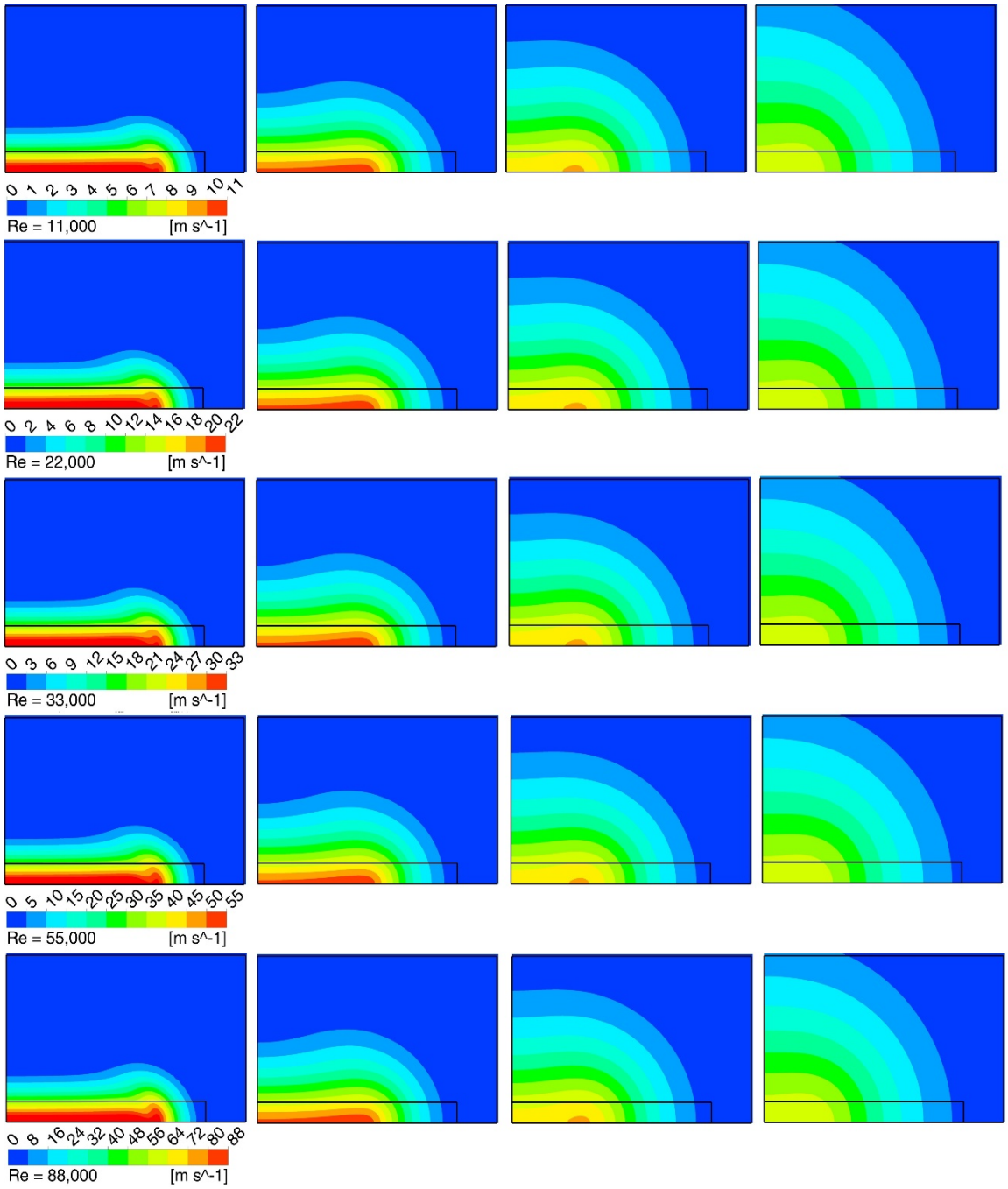

Fig. 4.6 *Color contour diagrams showing magnitudes of the perpendicular velocity in planes situated at x/b = 5, 10, 15, and 20 (from left to right.). The target plate is positioned at* $X_{max}/b = 25$

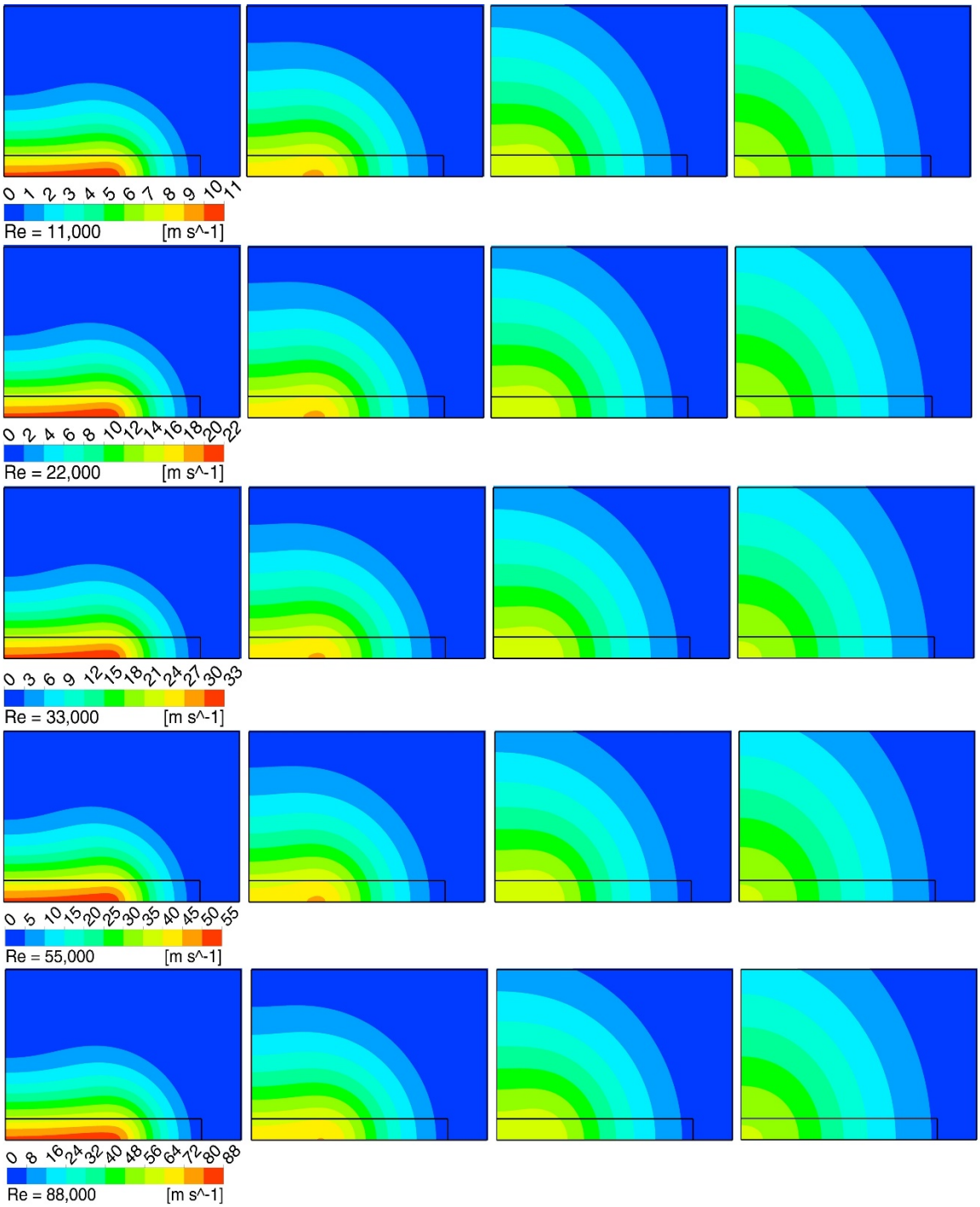

Fig. 4.7 *Color contour diagrams showing magnitudes of the perpendicular velocity in planes situated at x/b = 10, 15, 20, and 25 (from left to right). The target plate is positioned at* $X_{max}/b = 30$

Velocity field via vector diagrams

Details of the velocity field are well displayed by vector diagrams. As discussed earlier, there are two types of such diagrams that provide complementary information. One type is the normalized vector diagram in which all vectors are of common length and clearly show flow directions. The other type is designated as un-normalized wherein the length of each vector is proportional to the velocity magnitude measured from the tail of the vector. Vector diagrams will be displayed from *two vantage points* of observation. The first of these is a vertical plane which includes the axis of the system along its lower horizontal edge. The second vantage point includes planes which are perpendicular to the axis.

Vector diagrams displayed from the first vantage point are conveyed in Figs. 4.8, (a) and (b), where the (a) part of the figure shows un-normalized vectors while the (b) part shows normalized vectors. Inspection of both parts of the figure illustrate the growth of the vertical thickness of the jet owing to entrainment and subsequent impingement on the target plate. The (a) part of the figure shows the velocity variations across the thickness of the jet and the interface between the jet and the nearly stationary quiescent fluid in the surroundings. The interface is more sharply identified in the un-normalized jet diagram. It appears that the effect of impingement on the target plate on the growth of the jet begins at approximately between x/b = 25 and 27.

The large portions of Fig 4.8(a) devoid of vectors contain slowly moving fluid whose presence is revealed by Fig. 4.8(b). That figure shows fluid being entrained into the thickening jet. Also seen in the figure is flow passing over the outer surface of the delivery duct. These velocities of these flows are very small compared with the velocities within the jet proper.

Vector diagram plots will be presented for the space between the jet emergence plane and the target plate at X_{max}/b = 30. In general, vector diagrams can be used alternatively to display flow information that lies in the plane of the diagram or is perpendicular to that plane. Here, in recognition of the fact that the color contour diagrams of Figs. 4.5, 4.6,

and 4.7 conveyed information on velocities perpendicular to the displayed plane, the vector diagrams to be presented are focused on velocities that lie in the plane of observation.

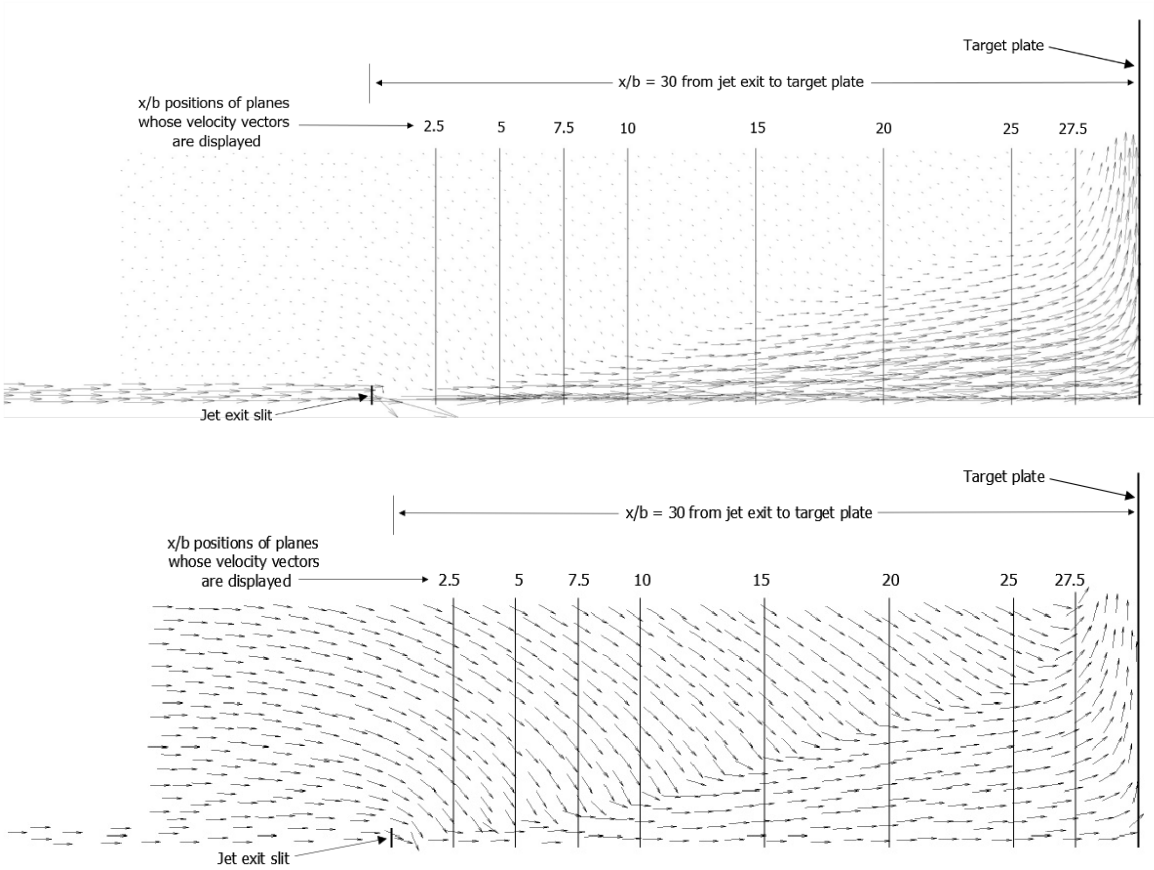

Fig. 4.8 *Vector diagrams that lie in a vertical plane whose lower edge coincides with the axis of the jet. (a) Un-normalized vectors, (b) normalized vectors. The target plate is at* $X_{max}/b = 30$

Figures 4.9, 4.10, and 4.11 each convey velocity vector information in planes that are perpendicular to the x-direction, which is the streamwise direction. There are (a) and (b) parts of each such figure. Figure 4.9(a) corresponds to a plane of observation at $x/b = 5$ whereas Fig. 4.9(b) is for plane at $x/b = 10$. Similarly, Fig 4.10, (a) and (b), conveys information for x/b = 15 and 20, and Figures 11(a) and (b) are for x/b = 25 and 27.5. In both the (a) and (b) parts, the figures in the left column display un-normalized vectors whereas those in the right column show normalized vectors. All of Figs. 4.9 - 4.11 are for the intermediate Reynolds number of 55,000.

Inspection of the evolution of the flow field starting at x/b = 5 through x/b = 25 shows that the entrainment flow is directed from locations situated far from the forward-flowing jet to the jet proper. With increasing x/b, the interaction of this inflowing stream with the jet surface creates a turning flow which is blocked by the symmetry surface which bisects the width of the jet. This blockage effect molds the turning into an upflow parallel to the symmetry surface. This upflow opposes the vertical downflow due to entrainment along that surface. The vector field at x/b = 27.5 is majorly affected by the close proximity of the target plate at X_{max}/b = 30. The fluid situated at the x/b = 27.5 perceives the absolute blockage of the target plate and recognizes that it must find a direction other than the x-direction to continue its flow. This recognition is responsible for what appears to be a radial outflow from the jet proper.

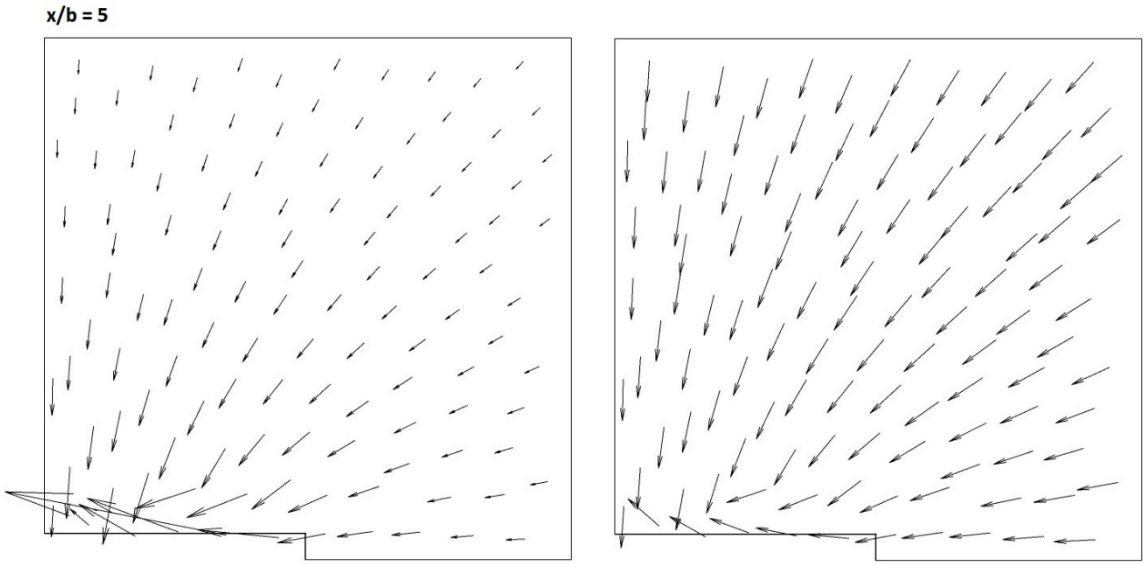

(a)

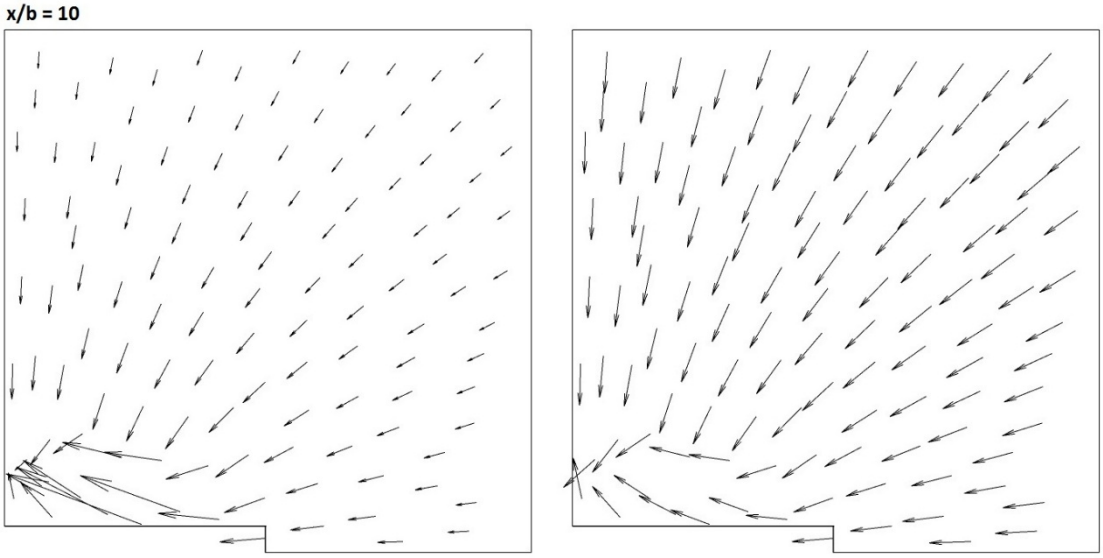

(b)

Fig. 4.9 *Velocity vector diagrams in planes defined by x/b = 5 Part (a) and x/b = 10 Part (b). Re = 55,000. Left-hand diagrams show un-normalized vectors and right-hand diagrams show normalized vectors.*

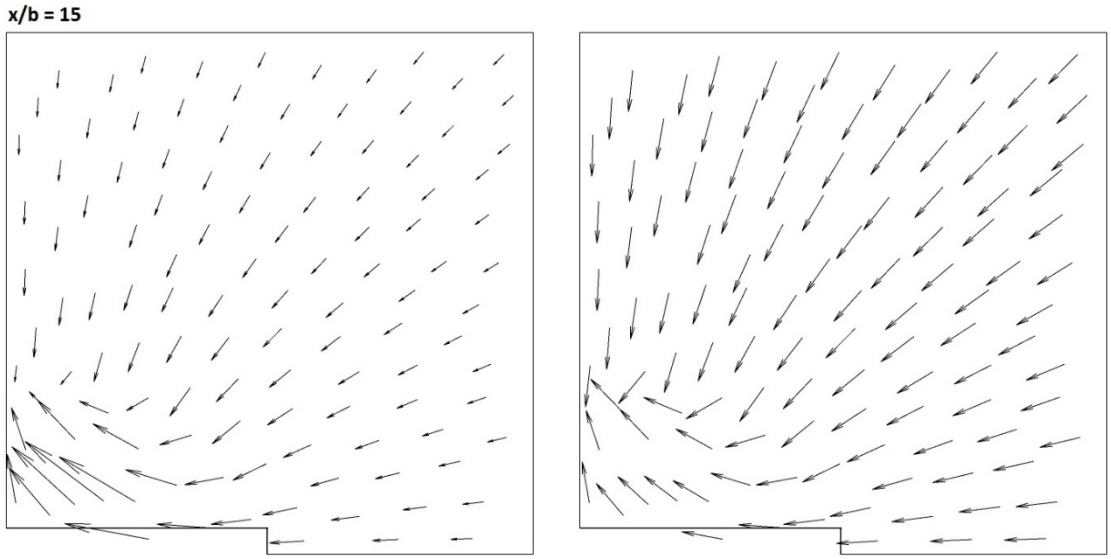

(a)

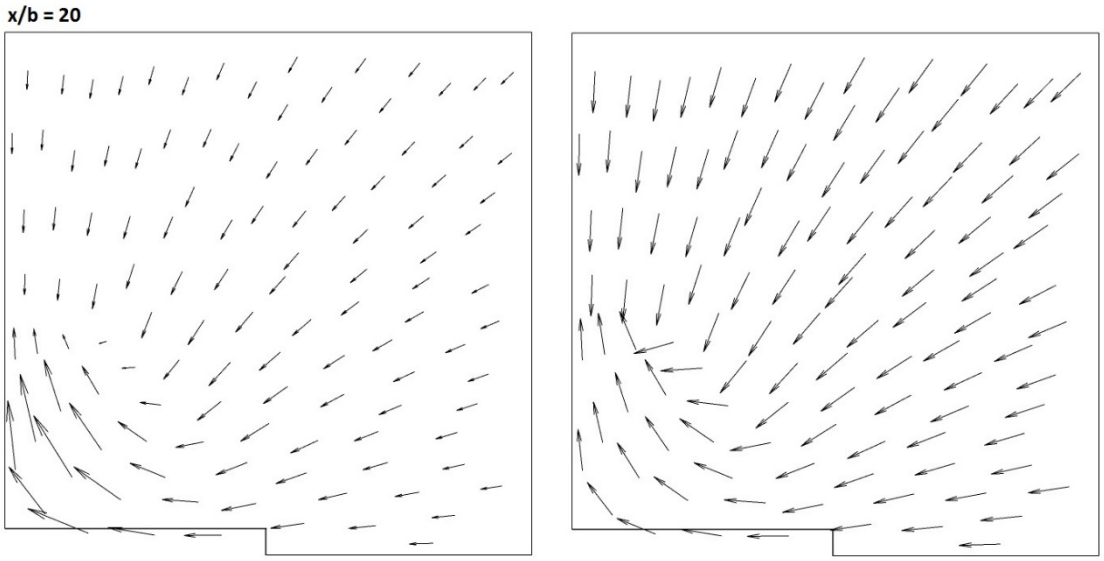

(b)

Fig. 4.10 *Velocity vector diagrams in planes defined by x/b = 15 Part (a) and x/b = 20 Part (b). Re = 55,000. Left-hand diagrams show un-normalized vectors and right-hand diagrams show normalized vectors.*

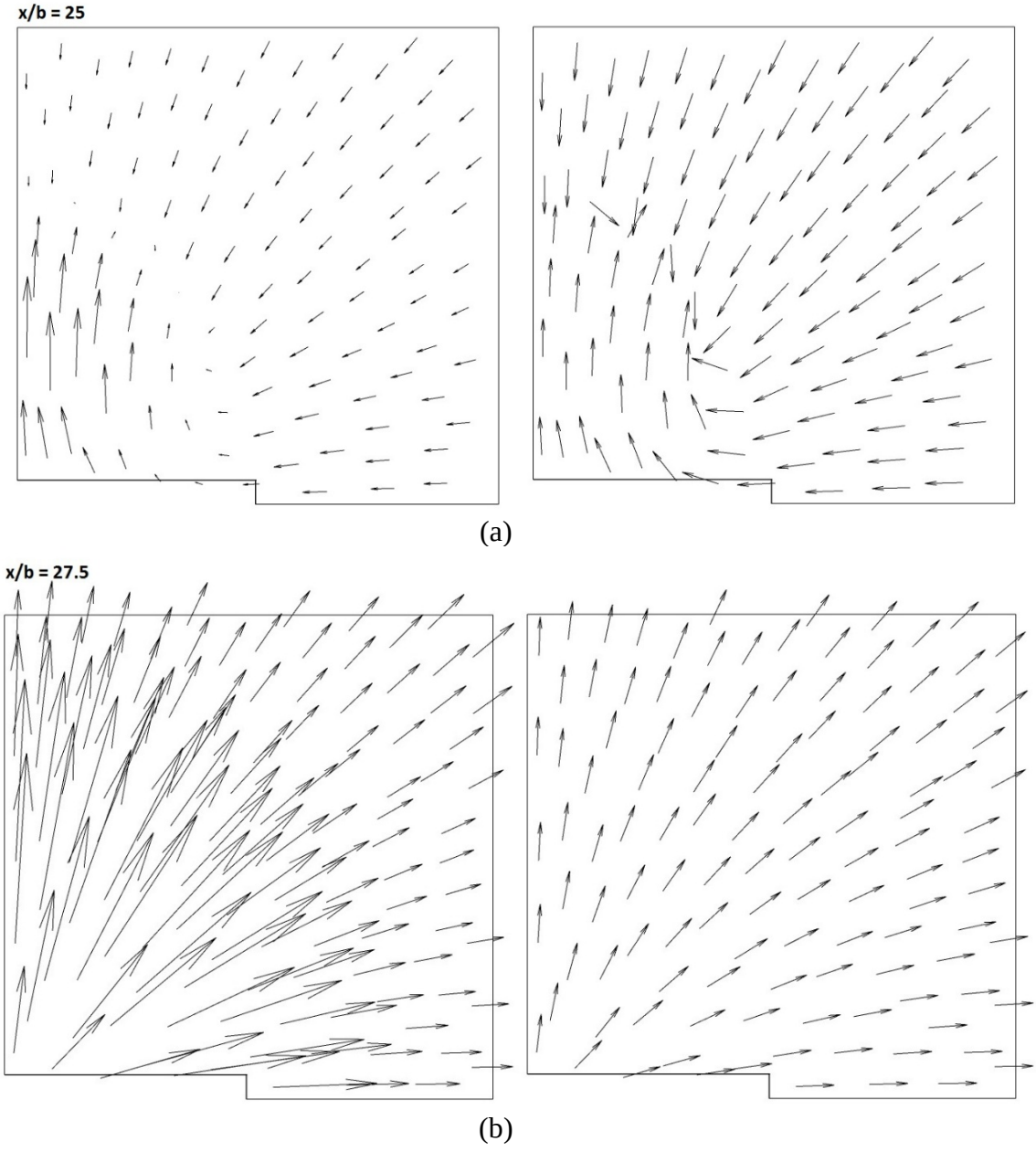

Fig. 4.11 *Velocity vector diagrams in planes defined by x/b = 25 Part (a) and x/b = 27.5 Part (b). Re = 55,000. Left-hand diagrams show un-normalized vectors and right-hand diagrams show normalized vectors.*

4.6 Heat Transfer Results and Discussion

In view of the great interest in jet-impingement heat transfer, the highlight of the present work is a definitive presentation encompassing both local and average results for the heat transfer coefficient. In this regard, it is appropriate to note that from the foregoing presentation of the velocity results, the jet-axis-turning phenomenon is present and is expected to influence the spatial variation and values of the heat transfer coefficients. Since, to the best knowledge of the author, there has been no recognition of the effects of jet-axis turning on impingement heat transfer in the Reynolds number range investigated here, it is appropriate to regard the forthcoming presentation of results as a conveyance of novel information.

Stagnation point heat transfer

The presentation will be initiated by focusing on local heat transfer coefficients at the stagnation point on the target plate, which corresponds to the center point of the plate. This information will be presented in dimensionless terms as follows. First, the local coefficient h is defined as

$$h = q/(T_{fluid} - T_{plate}) \tag{4.11}$$

In this equation, q is the local heat flux at the stagnation point, T_{fluid} is the temperature of the supplied air, and T_{plate} is the temperature of the plate surface. To achieve a dimensionless presentation, the local Nusselt number Nu will be used. It is customary to add a subscript to the Nusselt number to convey the dimension which appears in its definition number in order to assure its proper use. Therefore,

$$Nu_b = hb/k \tag{4.12}$$

where b is the height of the slit from which the jet emerges, and k is the thermal conductivity of the air. Here, the value of k is that at 25^{o}C.

A graphical presentation of the stagnation point heat transfer at the target plate is displayed in Fig. 4.12. In the figure, the Nusselt number at the stagnation point is plotted

as a function of the separation distance X_{max}/b of the target plate from the jet origin for parametric values of the Reynolds number. It can be seen from the figure that the highest values of the Nusselt number do not occur when the plate is nearest to the origin of the jet. This outcome has been observed in the experimental results of others [32] whose maximum Reynolds number was 22,000. As the distance between the jet origin and the target plate increases, a maximum value of the stagnation-point Nusselt number occurs approximately at $X_{max}/b = 10$, in accordance with the findings of Gardon [32]. Thereafter, as X_{max}/b continues to increase, the stagnation-point value decreases monotonically. This trend is well supported by the experimental data of Gardon [32]. The verification of the present results afforded by independent experiments lends strong support to the simulation model and its implementation. Although the aforementioned experiments were performed for Reynolds numbers no greater than 22,000, it is believed that the verified current model provides reliable data up to 88,000, the largest Reynolds number investigated here

In Fig. 4.12, the shape of the curves between $X_{max}/b = 20$ and 25 displays an unexpected undulation. The reason for this undulation will be explained shortly when results are presented from other viewpoints.

The results displayed in Fig. 4.12 are exhibited from a somewhat different viewpoint in Fig. 4.13. In the latter, the Nusselt number is plotted as a function of the Reynolds number for parametric values of the target plate location $X_{max}/b \geq 10$. For all $X_{max}/b \geq 10$, Fig. 4.13 indicates a power-law dependence of the Nusselt number on the Reynolds number. The results for the $X_{max}/b = 5$ case did not display a power-law behavior. This outcome may be attributed to the still-forming jet having a significant potential core at this X_{max}/b.

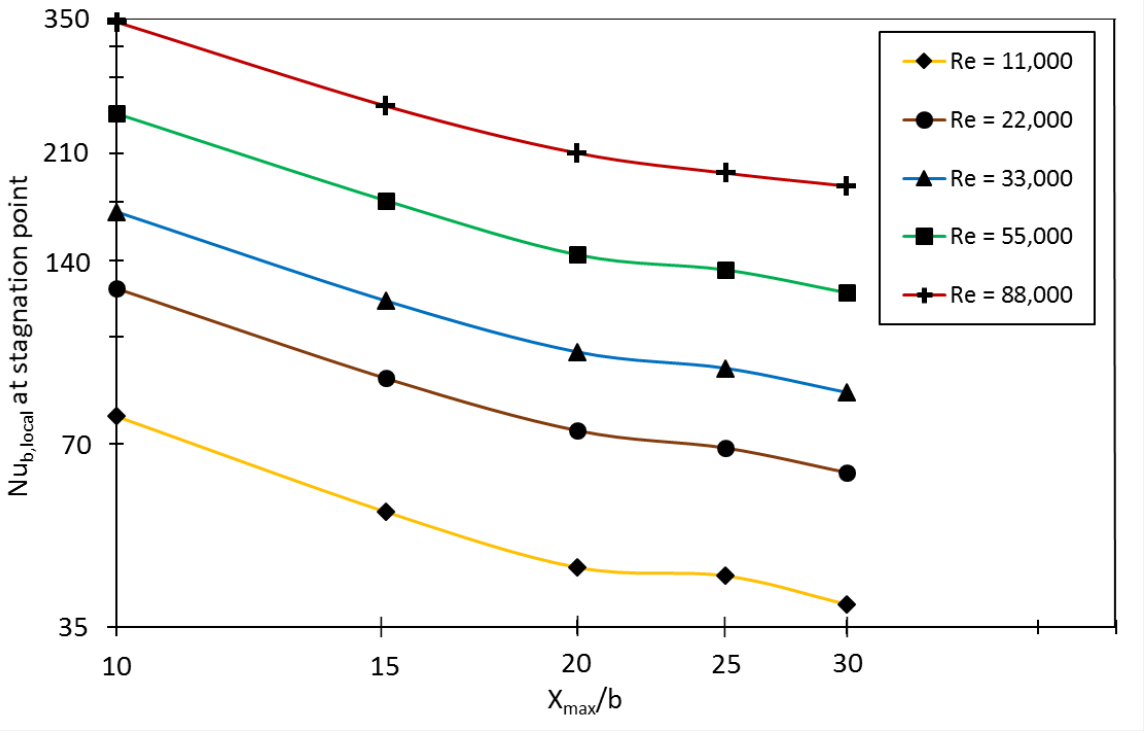

Fig. 4.12 *Stagnation point heat transfer at the target plate for various distances X_{max} between the jet egress and the target plate for Reynolds numbers between 11,000 and 88,000*

For the cases with $X_{max}/b \geq 10$, the slopes of the various power-law representations of Fig. 4.14 are virtually the same. This finding suggests that a more compact presentation of those results can be achieved by using a common power-law exponent for all of the cases being considered. This approach has been used in the construction of Fig. 4.14. For that figure, the correlation equation is

$$Nu_{b,stag} = f\left(\frac{X_{max}}{b}\right) Re^{0.725} \tag{4.13}$$

The function f is displayed in Fig. 4.14 and is well-represented by the equation,

$$f = .000157\left(\frac{X_{max}}{b}\right)^2 - 0.008348\left(\frac{X_{max}}{b}\right) + 0.156332\,, \quad \frac{X_{max}}{b} \geq 10 \tag{4.14}$$

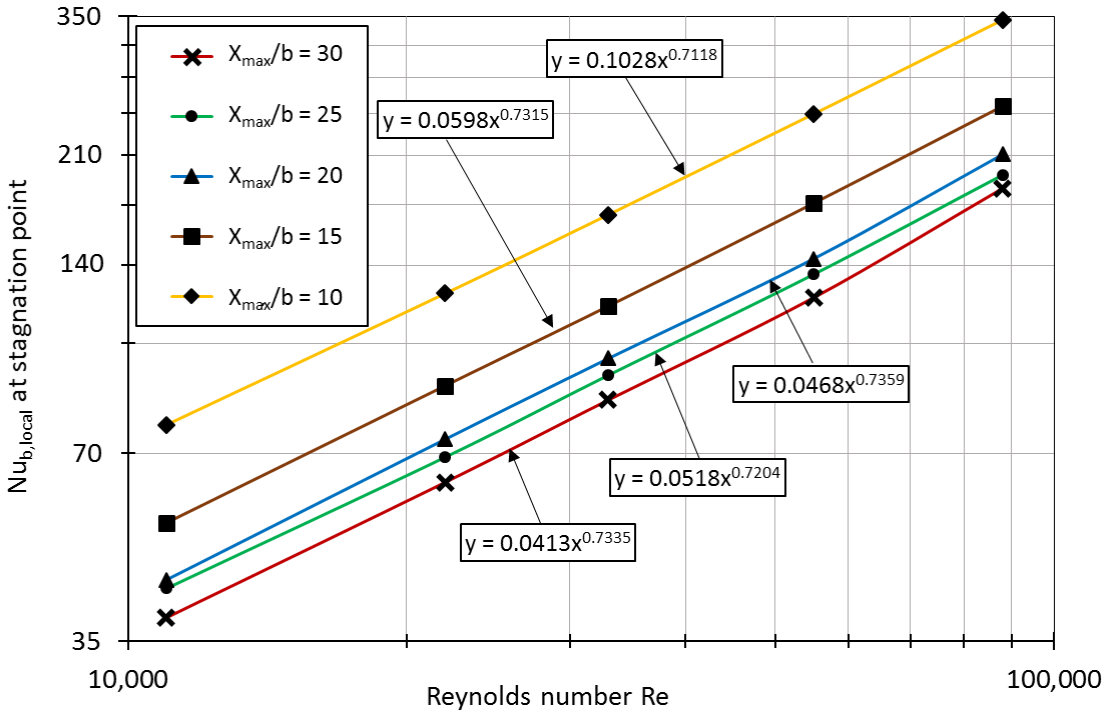

Fig. 4.13 *Stagnation-point heat transfer at the target plate as a function of Reynolds number for parametric values of the distance between the jet egress and the plate location*

Spatial variations of the local heat transfer results

The variations of the local Nusselt number along coordinate lines inscribed on the target plate will now be presented. First, focus will be directed to the line $y = 0$, which is a horizontal line whose orientation can be verified by reference to Fig. 4.2(b). Along that line, z/b varies from zero (stagnation point) to a maximum value of 75 which is the half width of the target plate in the horizontal direction. Figures 4.15 and 4.16 convey this information. Figure 4.15 displays the local results for Re = 11,000 and 22,000, respectively in Parts (a) and (b). Similarly, Fig. 4.16 conveys the results for Re = 33,000 and 55,000.

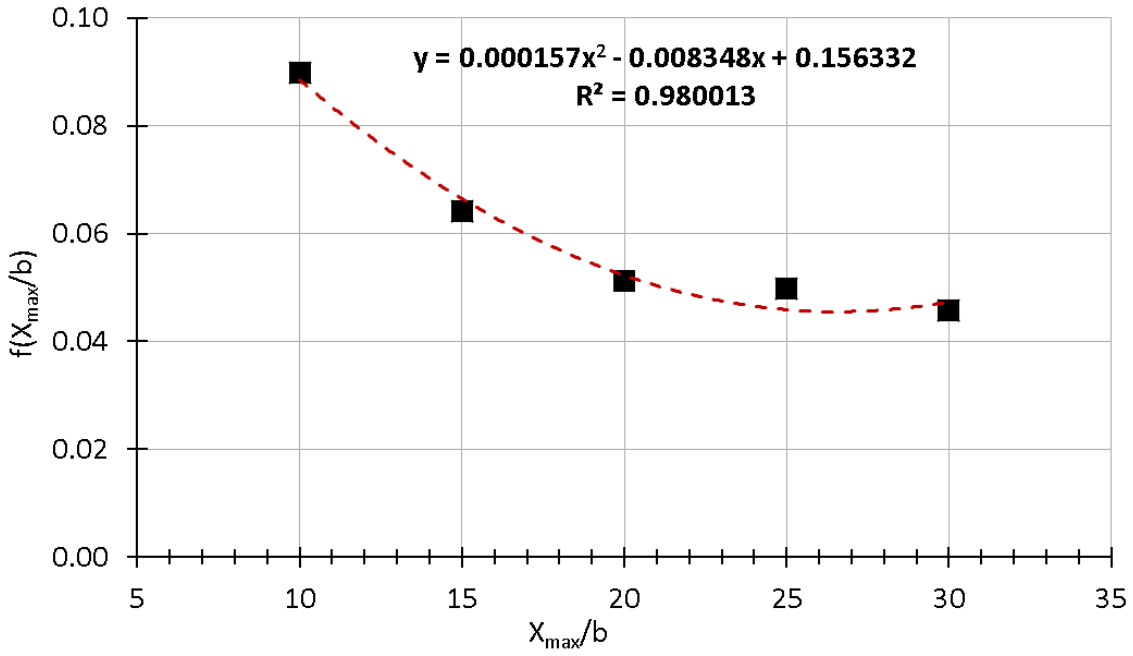

Fig. 4.14 *Dependence of the coefficient f on* X_{max}/b

Inspection of Fig. 4.15 indicates a non-monotonic variation of the local Nusselt number as a function of position along the z-axis. In particular, when the target plate is situated at locations $X_{max}/b \leq 25$, a local maximum is observed in the spatial variation of the local Nusselt number at values of $z/b \sim 2$ - 3. Further inspection indicates that the higher values of the local maximum occur for the smaller values of X_{max}/b; with increasing values of X_{max}/b, the magnitudes of the local maxima decrease. Simultaneously, the location of the maximum moves closer to the jet origin with decreasing values of X_{max}/b. It may be conjectured that the low z/b behavior observed in Fig. 4.15 is due to the progressive intrusion of turbulence into the potential core of the emerging jet.The trends that are observed in Part (a) of Fig. 4.15 are reinforced by observation of Part (b). In both figures, at values of z/b well beyond the locations of the local maxima (i.e., z//b ≥ 30), the Nusselt numbers have dropped off to virtually negligible values. As expected, symmetry prevails at z/b = 0, the stagnation point. The presence of off-axis Nusselt number peaks can be verified by experimental results [33, 34] in literature available for smaller Reynolds numbers.

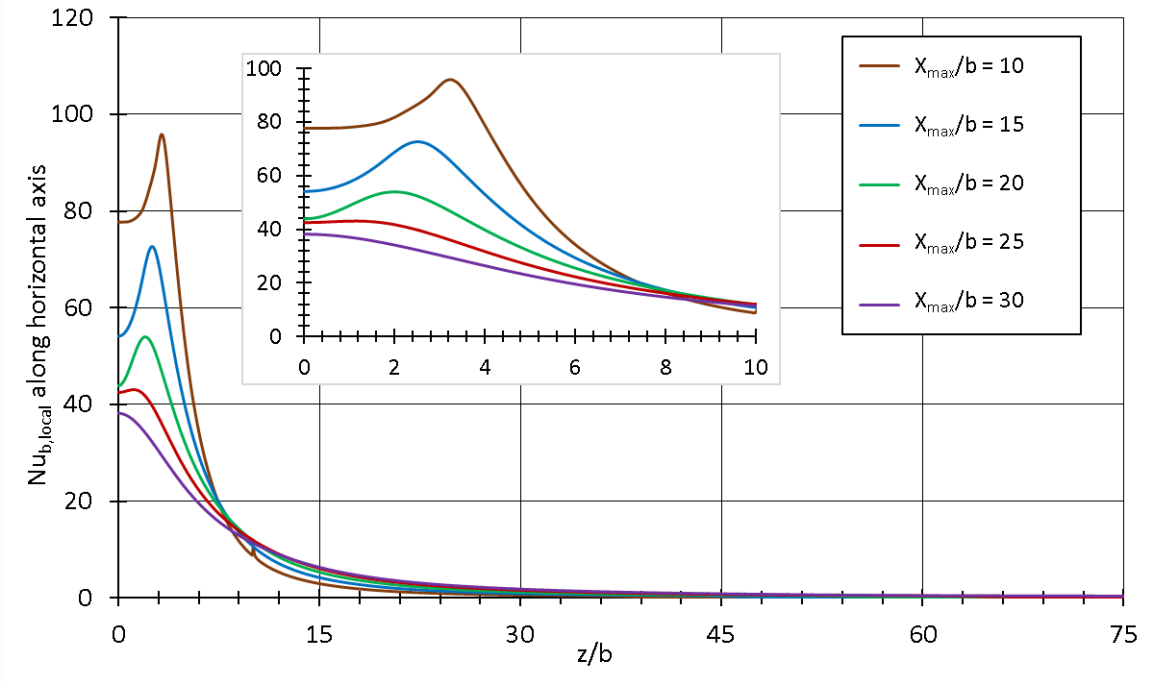

(a)

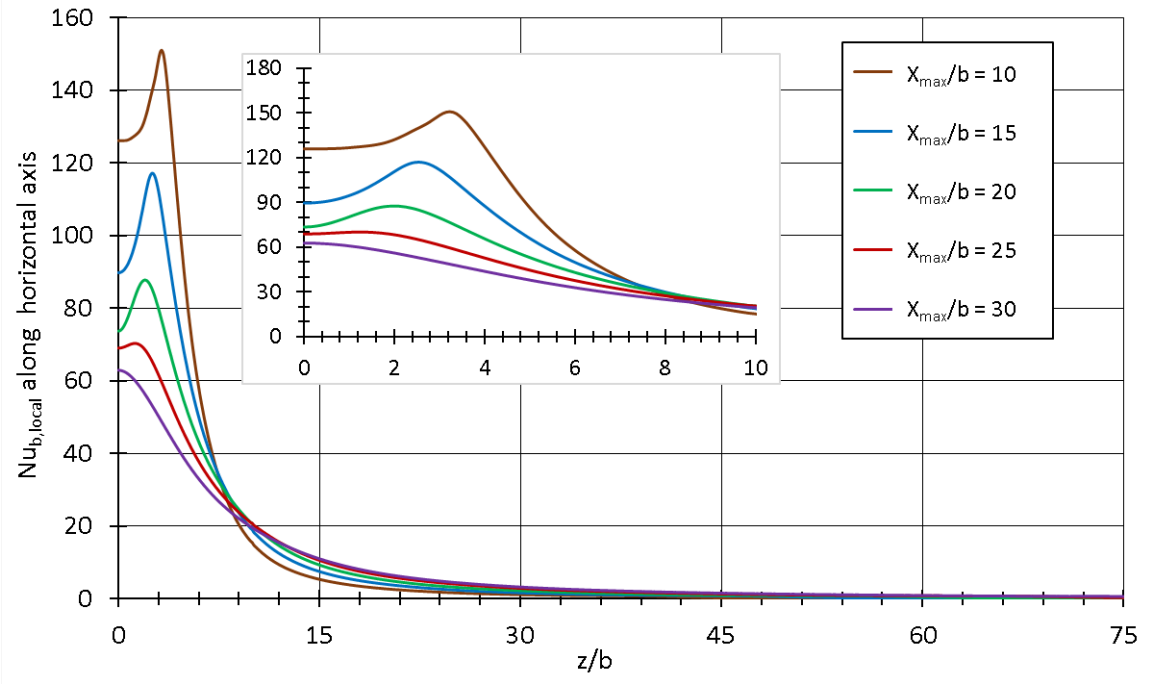

(b)

Fig. 4.15 *Variation of the local Nusselt number along the horizontal axis (y = 0) of the target plate. (a) Re = 11,000, (b) Re = 22,000*

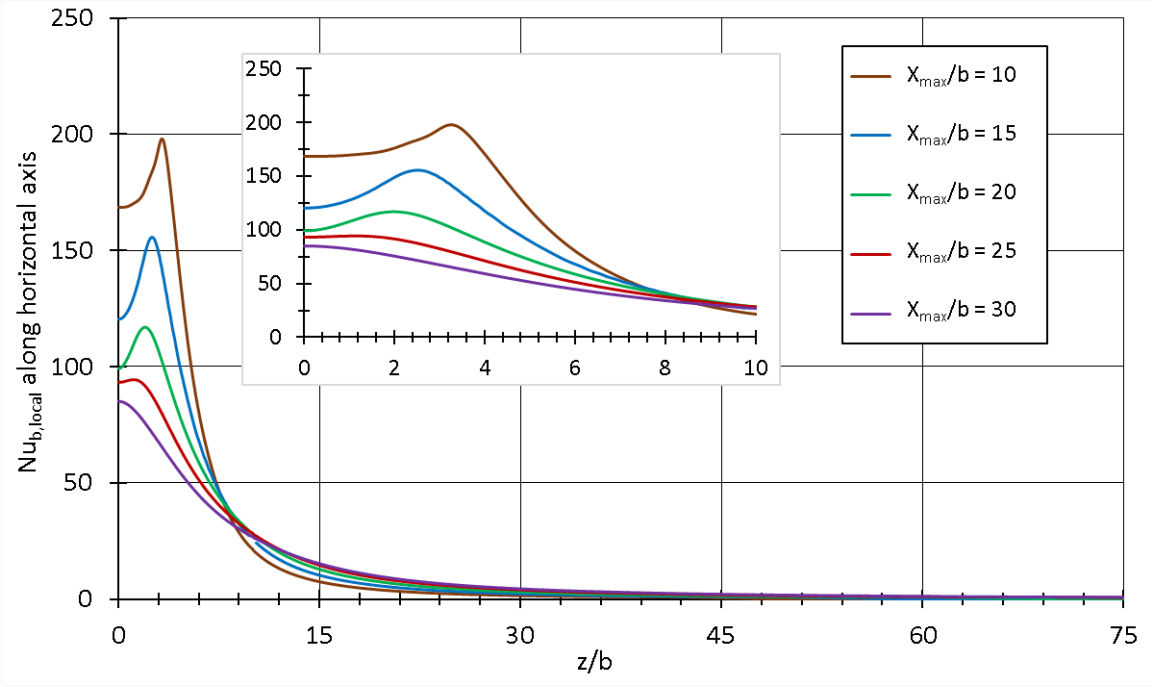

(a)

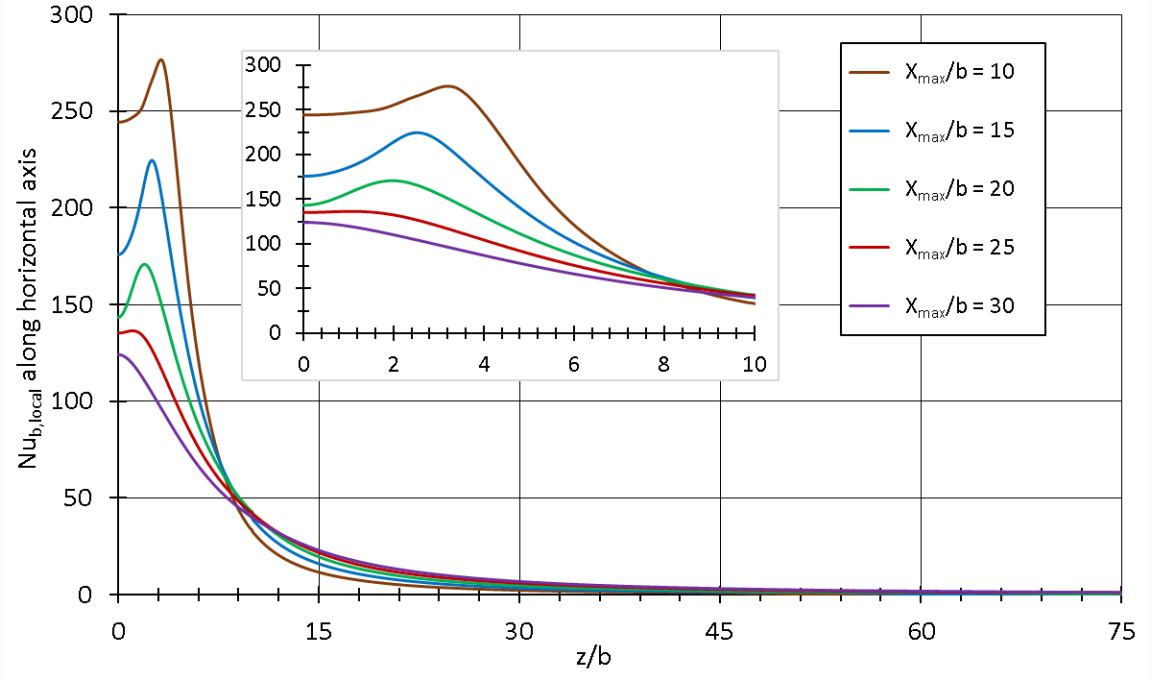

(b)

Fig. 4.16 *Variation of the local Nusselt number along the horizontal axis (y = 0) of the target plate. (a) Re = 33,000, (b) Re = 55,000*

Figure 4.16 is a continuation of Fig. 4.15 for the Reynolds numbers of 33,000 and 55,000. The main difference between the two figures is in the magnitudes of the Nusselt numbers. Clearly, the higher the Reynolds numbers, the larger the magnitudes of the Nusselt numbers. Other than that, the trends exhibited in the two figures are the same.

Attention is now refocused to the variation of the local Nusselt number on the plate surface along the y direction for the vertical line z = 0. The traverse starts at the stagnation point y/b = 0 and proceeds to y/b = 75, which is the half height of the target plate. This information is conveyed in two figures, 4.17 and 4.18, each of which has (a) and (b) parts. Figures 4.17 are for Re = 11,000 and 22,000, whereas Figs. 4.18 are for Re = 33,000 and 55,000. An overview of this group of four figures indicates that the trends displayed do not change as a function of Reynolds number. In particular, no off-axis peaks exist. The main trends are that the magnitude of the Nusselt number increases monotonically with increasing Reynolds number and that the magnitude also increases with diminishing values of the distance X_{max}/b between the jet emergence and the target plate. These trends are physically reasonable. It is noteworthy that the behaviors of the Nusselt number along the horizontal traverse (Figs. 4.15 and 4.16) and the vertical traverse (Figs. 4.17 and 4.18) are so different. These different behaviors are consistent with the different rates of evolution of the jet cross-sectional shape that were set forth in Figs. 4.5 - 4.7.

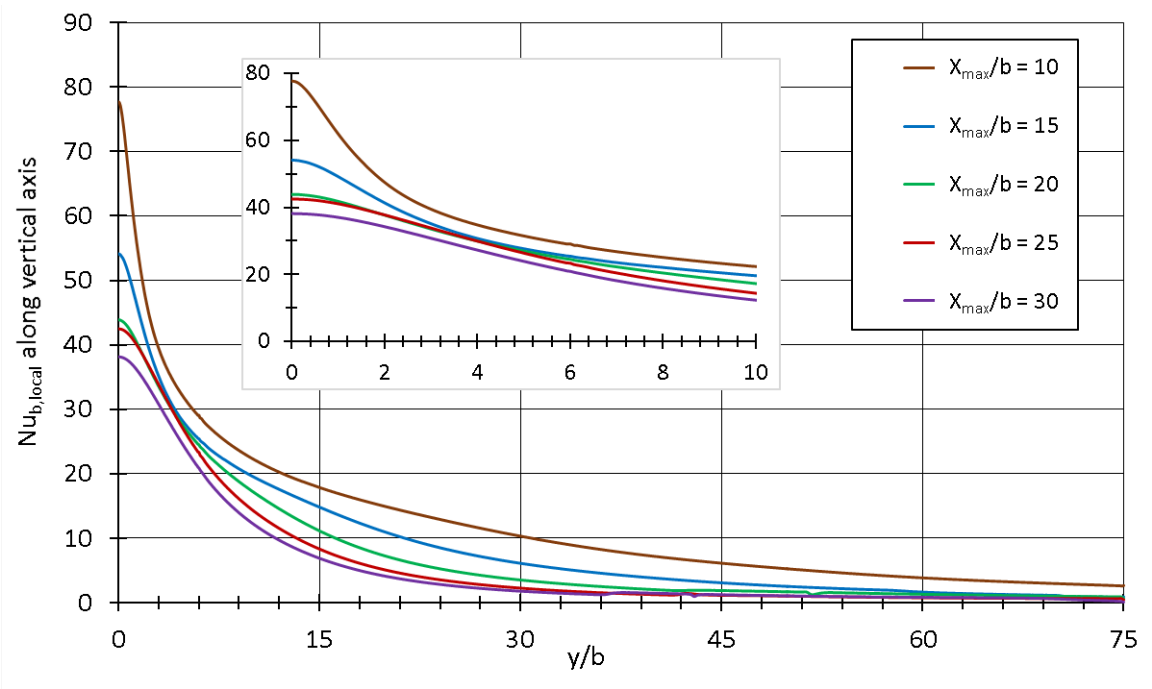

(a)

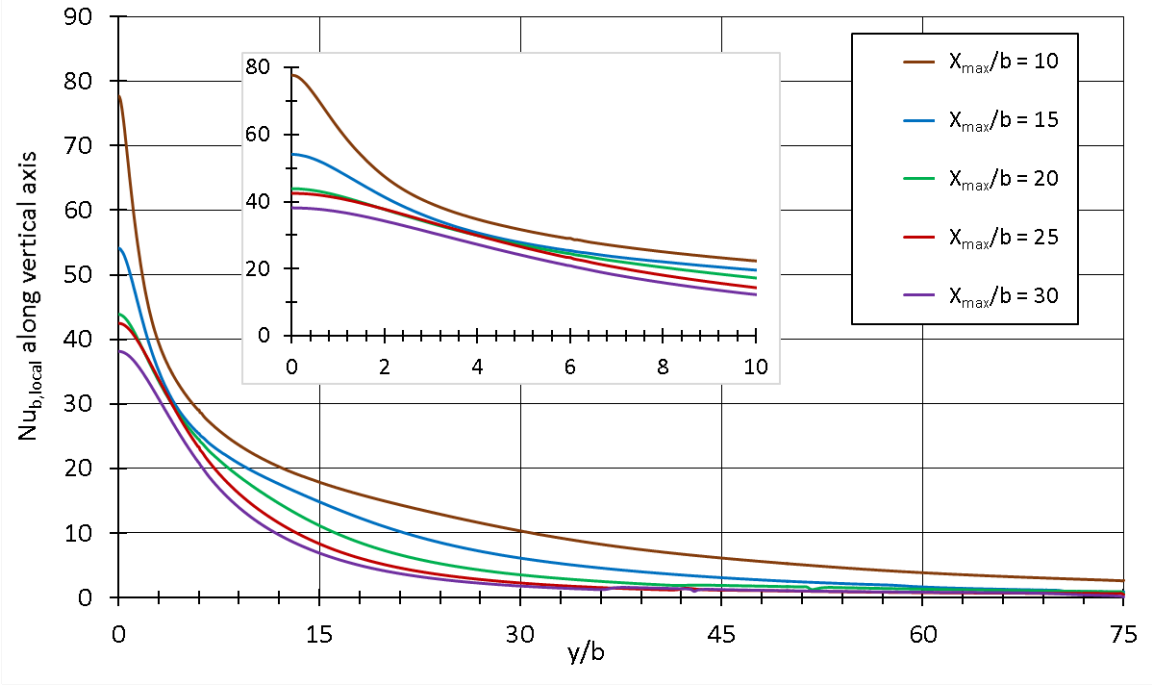

(b)

Fig. 4.17 *Variation of the local Nusselt number along the vertical axis (z = 0) of the target plate. (a) Re = 11,000, (b) Re = 22,000*

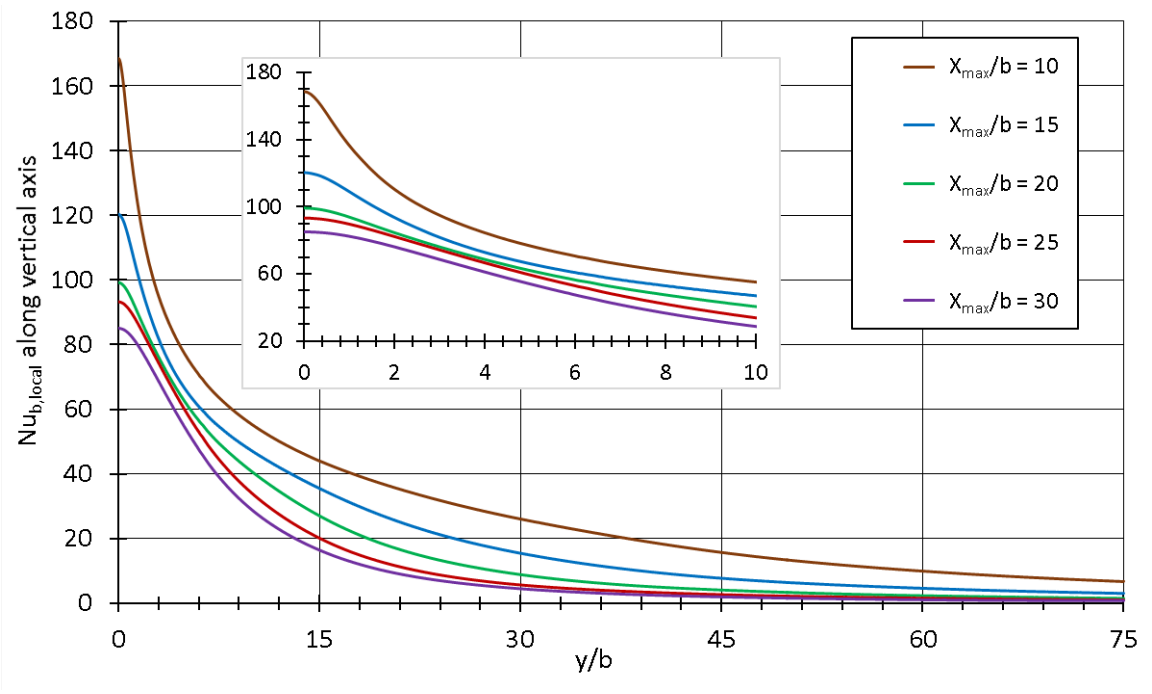

(a)

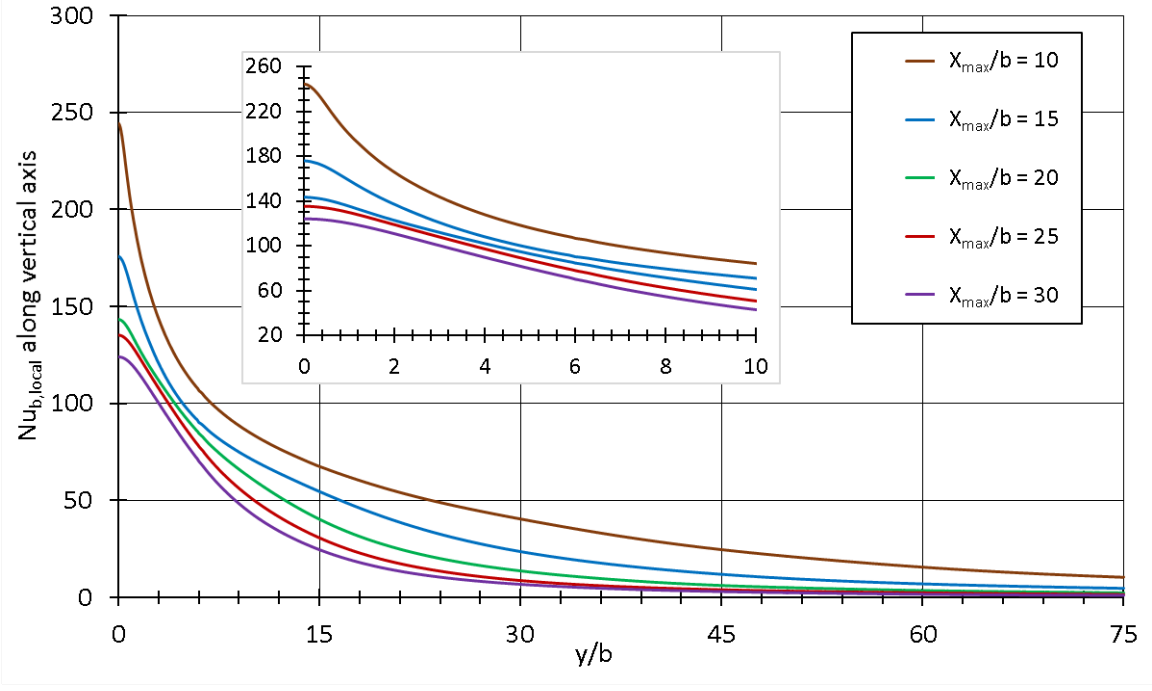

(b)

Fig. 4.18 *Variation of the local Nusselt number along the vertical axis (z = 0) of the target plate. (a) Re = 33,000, (b) Re = 55,000*

The preceding figures have conveyed local heat transfer results for specific locations on the target plate such as the stagnation point (Figs. 4.12 and 4.13), along the horizontal axis of the impingement plate (Figs. 4.15 and 4.16), and along the vertical axis of the impingement plate (Figs. 4.17 and 4.18). Now, a different mode of presentation will be used to display the distribution of the local heat transfer coefficient at all points on the surface of the target surface. That display will be the color contour diagrams of Fig. 4.19.

The figure consists of a matrix of 20 front-face views of the impingement plate. A given horizontal strip of five plate faces corresponds to a given Reynolds number. There are five such horizontal strips. From the uppermost to the lowermost strip, the Reynolds number is varied from 11,000, 22,000, 33,000, 55,000, and 88,000. The five front-face views for a given horizontal strip (or given Reynolds number) correspond respectively to plate locations $\underline{Xmax/b}$ = 10, 15, 20, 25, and 30. The heat-transfer-coefficient values for each Reynolds number are identified by colors which are matched to numerical values of the transfer coefficient by means of a color strip situated immediately below the horizontal array of front-face views to which it pertains. It is interesting to note the changes in the numerical meanings of the color strips with respect to the Reynolds number. The maximum transfer coefficients corresponding to the right-hand end (the red color) of the respective strips are 120, 195, 275, 390, and 550 for Re = 11,000, 22,000, 33,000, 55,000, and 88,000 respectively. In addition, the numerical range of each color also differs with the Reynolds number.

For discussion purposes, it is convenient to focus on a given Reynolds number and to identify the responses of the heat transfer coefficient to variations of the distance X_{max}/b between the jet egress and the target plate. As a guide for expectations with regard to the heat transfer results, it is useful to re-examine the development of the velocity field displayed in Figs. 4.5 – 4.7. The useful facts extracted for the velocity field results are: (a) the expansion of the jet as a function of x/b is considerably greater in the vertical direction than in the horizontal direction, (b) the jet cross section increases with increasing x/b, and (c) the jet velocity magnitudes decrease with increasing x/b.

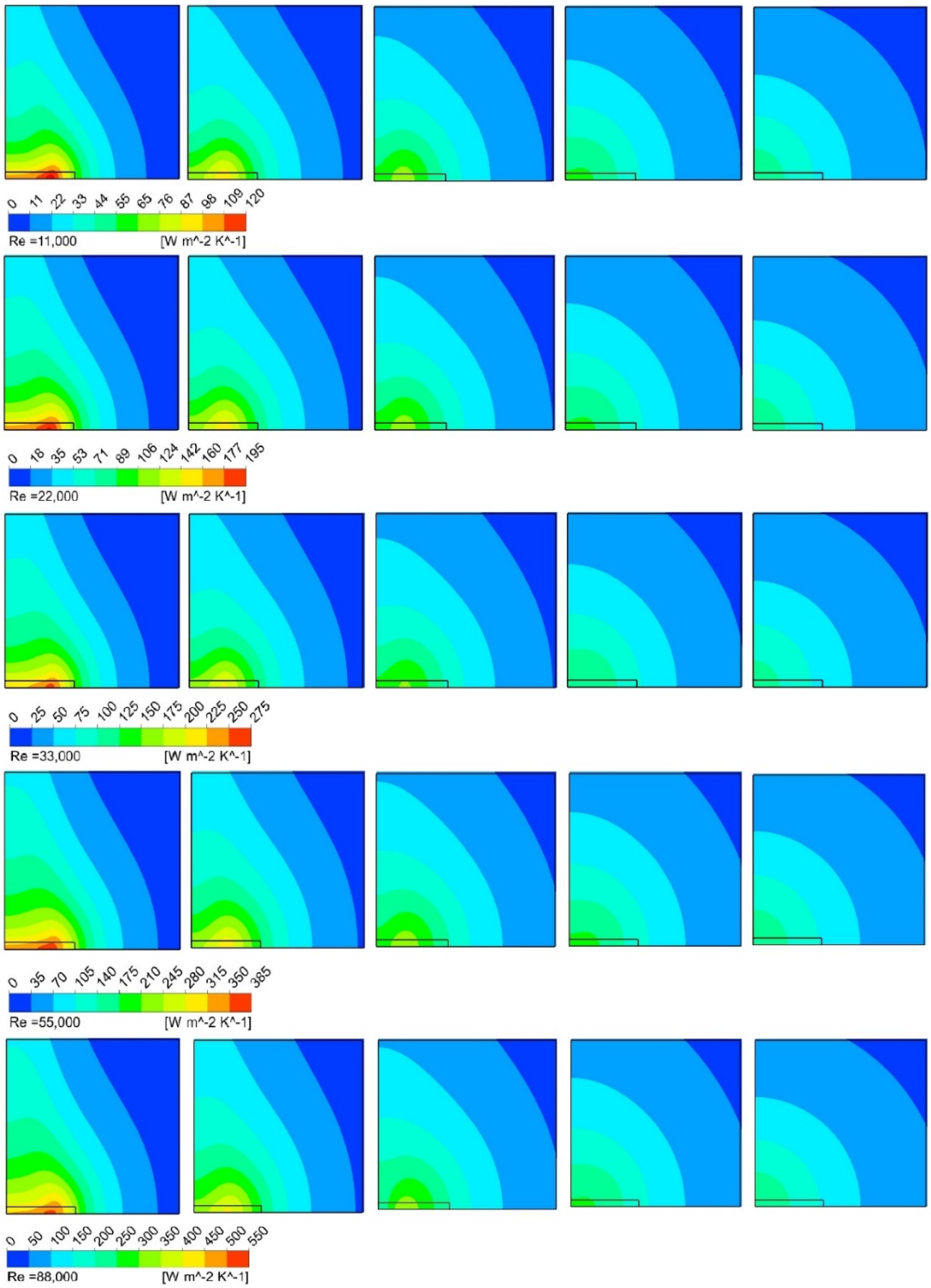

Fig. 4.19 *Contours of local heat transfer coefficient h for X_{max}/b = 10, 15, 20, 25, and 30 for Re = 11,000, 22,000, 33,000, 55,000, and 88,000, from top to bottom*

In appraising the heat transfer results of Fig. 4.19, it is relevant to note that each front-face diagram corresponds to only a portion of the plate where heat transfer is taking place and not the plate in its entirety, for the purposes of better representation.

Consequently, it appears that the highest magnitude of the transfer coefficient is achieved when the target plate is at its closest position (X_{max}/b = 10) with respect to the jet egress location. With increasing X_{max}/b, there is a general decrease in the magnitude of the transfer coefficient and a shrinkage of the impingement area where the higher coefficients are encountered. The shape of the impingement area also changes in accordance with the axis-switching process so that at the largest separation distance, X_{max}/b =30, the shape of the impinging jet is virtually circular. This finding negates the improper expectation that an impinging rectangular jet leaves a rectangular footprint on the target plate.

4.7 Concluding Remarks

This chapter is focused on an important real-world thermal management problem. The management tool investigated here is jet impingement. It is well established that jet impingement is capable of providing the largest possible values of the convective heat transfer. The employed solution methodology is numerical simulation.

Jets are created by numerous means, often simplified for the purposes of analysis relative to actual jet-producing geometries. Here, a geometry that possesses high fidelity with respect to real-world applications is considered. In particular, the jet, which is air, is produced at the outlet cross section of a long rectangular duct. The duct outlet cross section is capped by a plate which possess a rectangular slit which transforms the fully developed duct flow into a sharply etched rectangular jet. The thus-created jet passes into a free space without obstructions and finally impinges on a square plate situated at the downstream end of that space. The temperatures of the impinging air and the target plate are different, thereby giving rise to heat transfer at the plate surface.

The independent variables investigated here include the dimensionless separation distance between the jet egress location and the impingement plate surface. For each of several fixed values of the separation distance, several intervening stations are selected to

define planes that are parallel to the impingement plate. The distribution of the jet velocity in all such planes is displayed in order to illustrate the morphing shape of the jet cross section. Those displays clearly document that during its time of flight between the egress slit and the impingement plate, the cross-sectional shape of the jet may evolve from a pure rectangle mirroring the slit geometry to a circular cross section or an intermediate shape upon impingement. This phenomenon, called jet-axis switching, has not in the past been demonstrated for the range of Reynolds numbers investigated here. The Reynolds number, the second independent variable of this investigation, ranged from 11,000 to 88,000.

Jet-axis switching is shown to have a profound effect on the heat transfer coefficients on the surface of the impingement plate. Results for the local transfer coefficient are presented individually on graphs at the stagnation point, along the horizontal axis of the impingement plate and along the vertical axis of the impingement plate. Color contour diagrams are used to display the full spatial distribution of the transfer coefficient over the entire surface of the impingement plate. The highest values of the transfer coefficient occur at the smallest separation distance between the jet egress slit and the impingement plate. With increasing separation distance, there is a general decrease in the magnitude of the coefficient. Furthermore, the spatial distribution of the coefficient changes significantly owing to jet-axis switching.

CHAPTER FIVE

Heat Transfer in a Straight Pipe Downstream of a Bend with Partial Blockages of the Bend Flow

5.1 Introduction

Bends are a frequently encountered component of piping systems. Among the extensive geometrical variants of bends, distinctions may be made between single bends and bend clusters. The clusters may include in-plane and out-of-plane bends in series. Another important geometric variable is the angle subtended between the inlet and exit cross sections of a bend, with the 90^o bend being the most common. Still another geometric variable is the ratio of the radius of curvature of the bend to the radius/diameter of the pipe bend. All of the foregoing bend categories and bend-related independent variables have motivated extensive experimental and numerical investigations which are reported in the published literature.

All of the numerical simulation models reported in the literature are based on the tacit assumption that the components of the piping system, including the pipeline upstream of the bend, the bend proper, and the pipeline downstream of the beam, mate with perfect geometrical congruence. This assumption may be difficult to fulfill in practice. Here, for the first time, a simulation model will be developed and numerically implemented whose focus is to determine the impact on the downstream flow and heat transfer of a mismatch of the upstream piping and the bend at its inlet.

The model for this first exploration is to characterize the mismatch at the bend inlet as a blockage quantified by the ratio of the blocked portion of the cross section to the total cross section. The specific model to be investigated here is the presence of a straight-sided, washer-like ring situated at the inlet cross section of the bend. Figure 5.1 is a schematic of the washer-like ring. The open flow cross section is the bore of the washer.

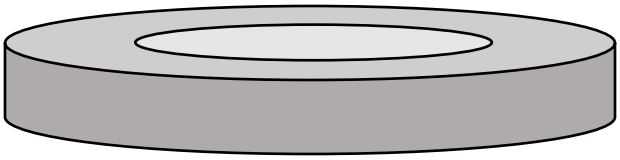

Fig. 5.1 *Schematic of the straight-sided, washer-like ring blockage*

The ratio of the blocked flow cross section to the blockage-free cross section, a main independent variable of the investigation, was varied between 0 and 60%. A second significant variable parameter of the study is the Reynolds number which extended over the range from 100 to 10,000. This range encompassed both laminar and turbulent flows. Another varied parameter is the radius of curvature of the bend, the chosen values of which gave rise to the ratios of the radius of curvature to the bend diameter of 1 and 3. The first of these ratio values corresponds to a short-radius bend whereas the second depicts a long-radius bend. Held fixed are the diameter of bend cross section and the diameters and lengths of the straight pipes which respectively deliver fluid to the bend and which receive the fluid outflow of the bend.

The focus of the investigation set forth in this chapter is the impact of the complex fluid flow field created by the bend and its upstream-end blockage on heat transfer in a straight pipe attached to the exit cross section of the bend. The uniqueness of this problem is that the flow at the bend exit should be heavily impacted by the combination of the partial blockage at the bend inlet and the curvature of the bend proper. To the knowledge of the writer, neither this fluid flow situation nor the associated heat transfer has not been investigated in the past.

5.2 Physical Description of the Simulation Model

A schematic diagram of the physical situation selected for study is conveyed in Fig. 5.2. As seen there, the system consists of four distinct entities: (a) a long straight upstream section of pipe that serves to develop the flow and deliver it to the bend inlet, (b) the washer-like ring that is situated at the downstream end of the aforementioned flow delivery pipe, (c) the bend proper, and (d) a long straight section that receives the outflow from the bend and serves to redevelop the flow. Heat transfer is confined to the downstream pipe.

The dimensions of these components are listed in Table 5.1. Figure 5.2 consists of two sections. The total piping system is displayed along the top and right-hand edge of the figure. The larger part of the figure shows an enlarged view of the bend, the blockage, and the pipes that interface with the inlet and exit of the bend.

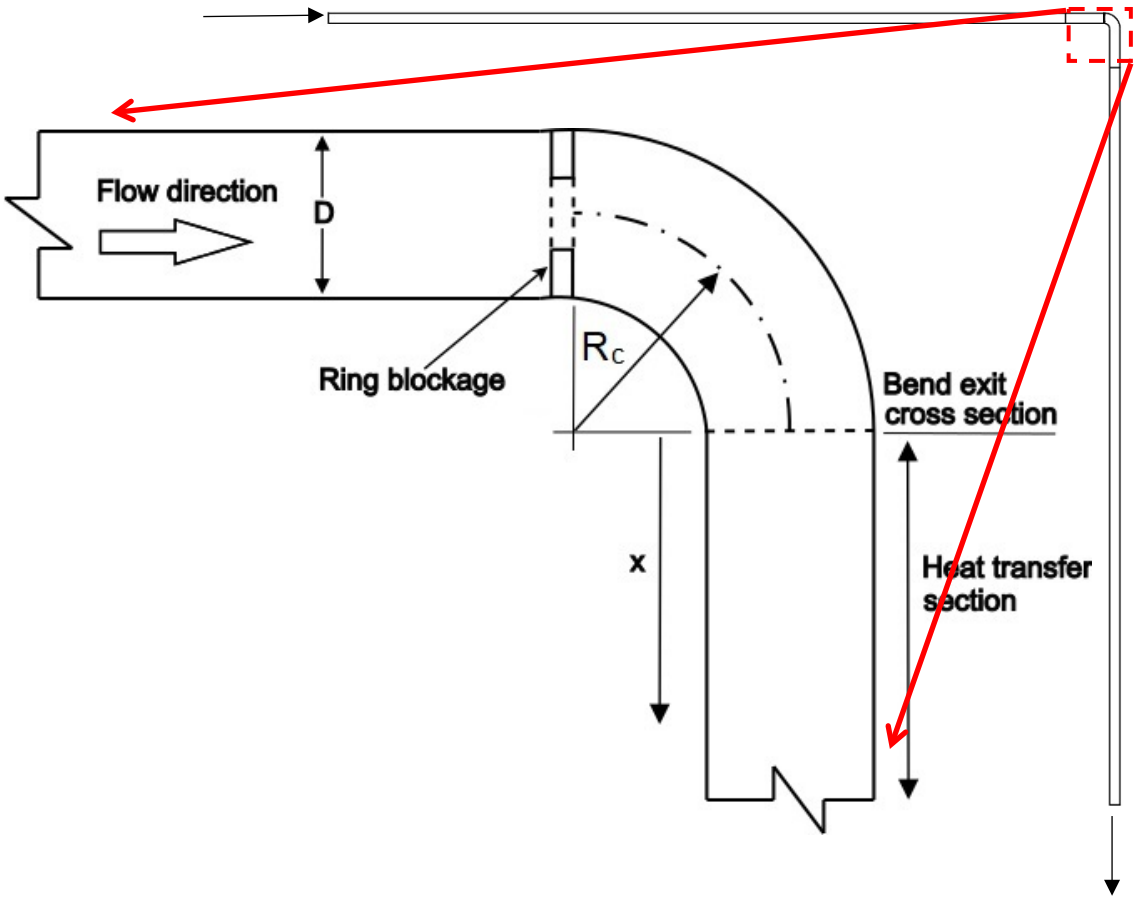

Fig. 5.2 *Schematic diagram of the piping system used for the numerical simulation.*

Table 5.1 *Dimensions of the components of the physical model.*

Component	**Symbol**	**Dimension (mm)**
Pipe diameter	D	8
Blockage thickness	t	0.5
Bend radius of curvature	R_c	8 or 24
Upstream and downstream pipe lengths	L	600 (L/D = 75)

The foregoing table presents dimensional information. Note that two different radii of curvature are considered, the ratios of the radii of curvature to the pipe diameter R_c/D are

1 and 3. Since long-radius pipe elbows or bends are defined as having values of this ratio ≥ 1.5, the bends considered here fall respectively into the short-radius and long-radius categories. In addition to the dimensionless parameters that appear in Table 5.1, the Reynolds number *Re* will be defined as

$$Re = \rho UD/\mu \tag{5.1}$$

in which ρ and μ are, respectively, the density and viscosity of the flowing fluid, and *U* is cross-sectional average velocity of the flow. The flowing fluid considered here is modeled as having constant density, viscosity, and specific heat, and Prandtl number. Specifically, the chosen properties are those of liquid water at 25°C. Since the final results will be presented in dimensionless terms, they are not restricted to a specific fluid but are dependent on the Reynolds and Prandtl numbers. The specific value of Prandtl number for the results is 5.77.

In simple flows, the flow regime is readily identified by the value of the Reynolds number. Flows in bends are properly regarded as complex, and this classification is strengthened when the mismatch-created blockages are taken into account. This seeming dilemma will be handled without difficulty here by choosing a turbulence model which reverts to laminar flow when the actual flow regime is laminar.

5.3 Governing Equations and their Solutions

Since consideration is to be given here to both laminar and turbulent flows, governing equations for those situations can be referred to in previous chapters. In Chapter Two, the RANS equations for turbulent momentum conservation are expressed by Eqn. (2.1) and that for mass conservation is stated in Eqn. (2.2). The governing equations for the SST turbulence model may also be found in Chapter Two as Eqns. (2.4), (2.5), and (2.6). Heat transfer was treated in Chapter Four, and the energy conservation equation is stated there in Eqn. (4.7). The turbulent Prandtl number definition stated in Eqn. (4.8) of that chapter will also be used here. The aforementioned equations were specifically written for turbulent flow and, therefore, contained quantities μ_{turb} and k_{turb}, respectively denoting the turbulence viscosity and the turbulent thermal conductivity. When laminar flow is to

be considered, these two quantities are eliminated from the equations in which they are situated for turbulent flow. No other specifications are needed here to identify the governing equations to be used in this chapter.

The software used for the numerical simulations performed for this chapter is ANSYS CFX 16.1. The meshing of the solution domain gave rise to about 19 million nodes. This node number was tested by various excursions and found to be accurate within 0.2% for the overall rates of heat transfer that are reported.

5.4 Results and Discussion

In the presentation that follows, the main emphasis will be placed on the heat transfer results. However, in order to provide a rational understanding of the trends among the heat transfer results, certain velocity results need to be presented and connected with the heat transfer. In addition, it is relevant to display velocity results to help clarify the interactions of the bend-based phenomena and those associated with blockages. Since the latter velocity results will be more compact in their display will the former ones, they will be presented first followed by the intermingled heat transfer and velocity results.

Fluid flow

The presentation format for the velocity results is a display of vector diagrams situated in a cross-sectional plane at the very exit of the bend. The display is conveyed in Fig. 5.4. Results are given for three Reynolds numbers: 500, 850, and 10,000. For each Reynolds number, there is a pair of side-by-side displays of the velocity field that show vectors that lie in the plane of the cross section. In particular, diagrams (a), (c), and (e) correspond to the situation where there is no upstream blockage. In contrast, diagrams (b), (d), and (f) convey results when a blockage is present. The entirety of Fig. 5.4 corresponds to the dimensionless radius of curvature ratio of 1, which is the more sharply contoured of the two bends considered here.

For the situation without blockage, such vector diagrams or their streamline counterparts are found in standard fluid-flow textbooks. Three examples of textbook images for fluid flow in a bend are presented in Fig. 5.3. All of these images show perfect symmetry about a diametral plane which connects the high pressure and low pressure zones of the cross section. It is interesting to observe that the fluid flow from the high to the low pressure chooses a path along the wall which is longer than a straight path through the center of the cross section. A second plane of symmetry is identifiable in the right-diagram of Fig. 5.3 as perpendicular to the first symmetry plane, cutting it at right angles.

It is relevant to compare the textbook illustrations shown in Fig. 5.3 with the flow patterns from the present numerical simulations that are displayed in Fig. 5.4 (a), (c), and (e). Clearly, there are significant differences in detail between the classical illustrations and the results of the present investigation. For one thing, the second plane of symmetry, identified in the foregoing discussion of Fig. 5.3, is totally absent in the present results. In particular, what is seen in the present figures 5.4 (a), (c), and (e) is a significant shift in the recirculating eddies toward the low-pressure end of the cross section. Furthermore, with increasing values of the Reynolds number, the eddies tend to

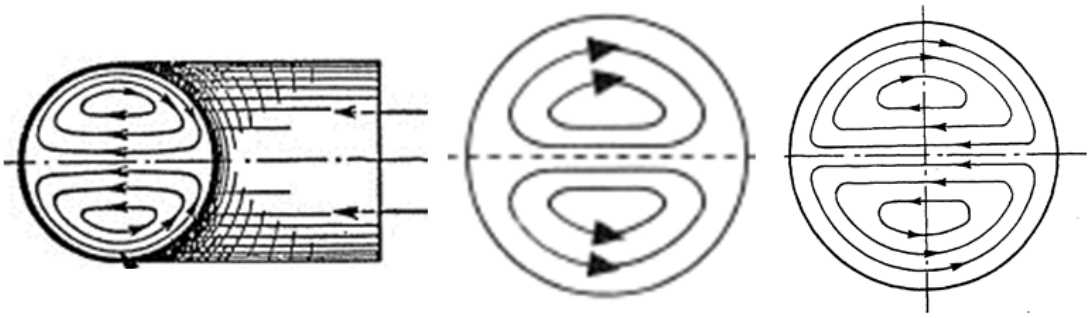

Fig. 5.3 *Three illustrative diagrams from the literature showing cross-sectional flow patterns in a bend*

become flattened against the bounding wall at the low-pressure end. Aside from these features, the flow directions displayed in figures 5.4 (a), (c), and (e) are the same as those in the classical diagram.

In appraising Fig. 5.4, it is useful to confirm that the left-hand edge of each of the displayed cross sections corresponds to the outer radius of the bend, which is the high

pressure zone. However, the fluid flow between the high and low pressure ends in a given cross section is clearly affected by the presence of upstream blockages as can be seen in diagrams (b), (d), and (f). In particular, for the Reynolds number of 850, the straight central path between the low and high pressure ends is by no means as cleanly chiseled as for the other cases that are displayed. This observation is of special interest with regard to the heat transfer results that will be displayed shortly. The issue at hand is whether Re = 850 is in the laminar, intermittent, or turbulent regimes.

As was true for the results in the absence of the blockage, the eddies that are seen in the presence of the blockage are also shifting toward the low pressure end. The general flow pattern seen in diagrams (b) and (f) are quite similar in that there are compact eddies which do not span the entire cross section. Indeed, in those cases, the left-end closure of the eddies is bounded by a fraying of vectors that are directed away from the closure. The most unique flow pattern displayed in the entirety of Fig. 5.4 is that shown in diagram (d). That diagram corresponds to Re = 850. The flow pattern shown there is irregular and distorted. The two major eddies have complex shapes and their left-end closures are bounded by frayed vectors that are directed toward the eddies. These irregularities and distortions may, in all likelihood, be the cause of unique behaviors in the heat transfer results for that Reynolds number.

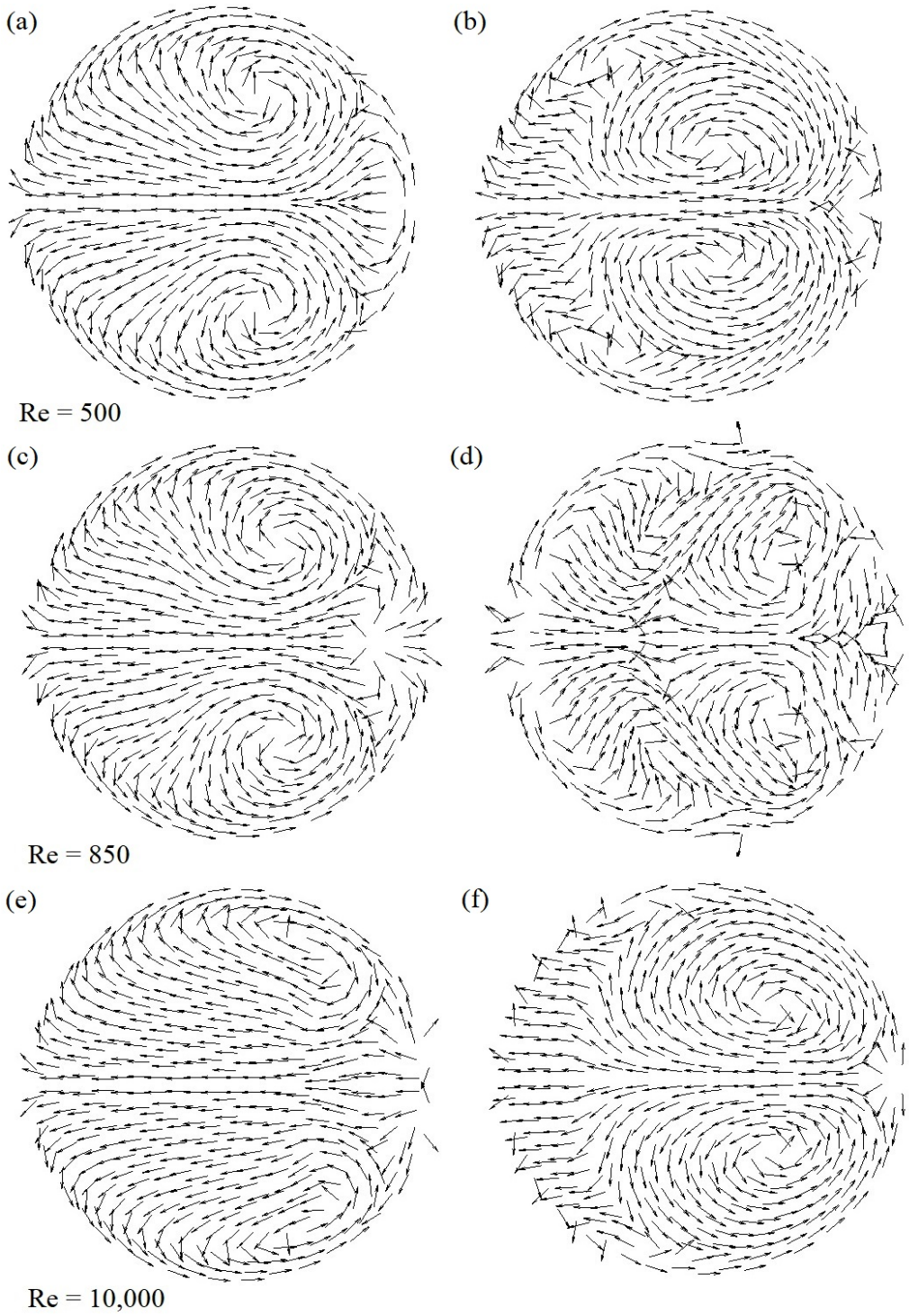

Fig. 5.4 *Normalized vector diagrams showing fluid flow in the bend exit plane for radius of curvature ratio = 1. The images on the left, (a), (c), and (e), are for the case with no blockage and those on the right, (b), (d), and (f), are for the 60% blockage case. Each pair of images corresponds to a given Reynolds number: Re = 500, 850, and 10,000*

Attention may now be turned to a display of cross-sectional fluid flow patterns for the radius of curvature ratio of 3. The format of the forthcoming presentation will follow that used in Fig. 5.4 for the radius of curvature ratio of 1. Focus will first directed to the results corresponding to the absence of the blockage; these results are set forth in parts (a), (c), and (e) of Fig. 5.5. An overview of those diagrams leads to an unexpected outcome: that flow patterns are much more sensitive to the radius of curvature than might have been expected. For one thing, the patterns seen in Fig. 5.5, (a), (c), and (e), are much more irregular than those in the corresponding diagrams of Fig. 5.4. This is especially true for the Reynolds number of 850. The return flow from low to high pressure, achieved smartly across the breadth of the cross section in Fig. 5.4, has been reduced to a discontinuous and interrupted path in Fig. 5.5. Once again, this complexity may be a symptom of intermittency. The Reynolds number results for 500 and 10,000 also suggest an increased complexity in the flow.

Focus may now be directed to diagrams (b), (d), and (f) of Fig. 5.5 which correspond to the presence of blockage. Clearly, the blockage effects are of high impact. In particular, the previous direct straight flow between the two pressure zones was from low to high pressure along the diameter that cut through the center of the cross section has undergone a reversal. Now, the flow along that path experiences a change of direction depending on where in the cross section observations are being made. Specifically, if observations are confined to the right-hand part of the cross section, flow is seen to be going toward the low pressure end. Indeed, that flow appears to be a coherent stream. In contrast, observations confined to the left-hand portion indicate the absence of coherency. Overall, there appears to be more mixing in the case of radius of curvature ratio equals 3 compared with that for the radius of curvature ratio of 1.

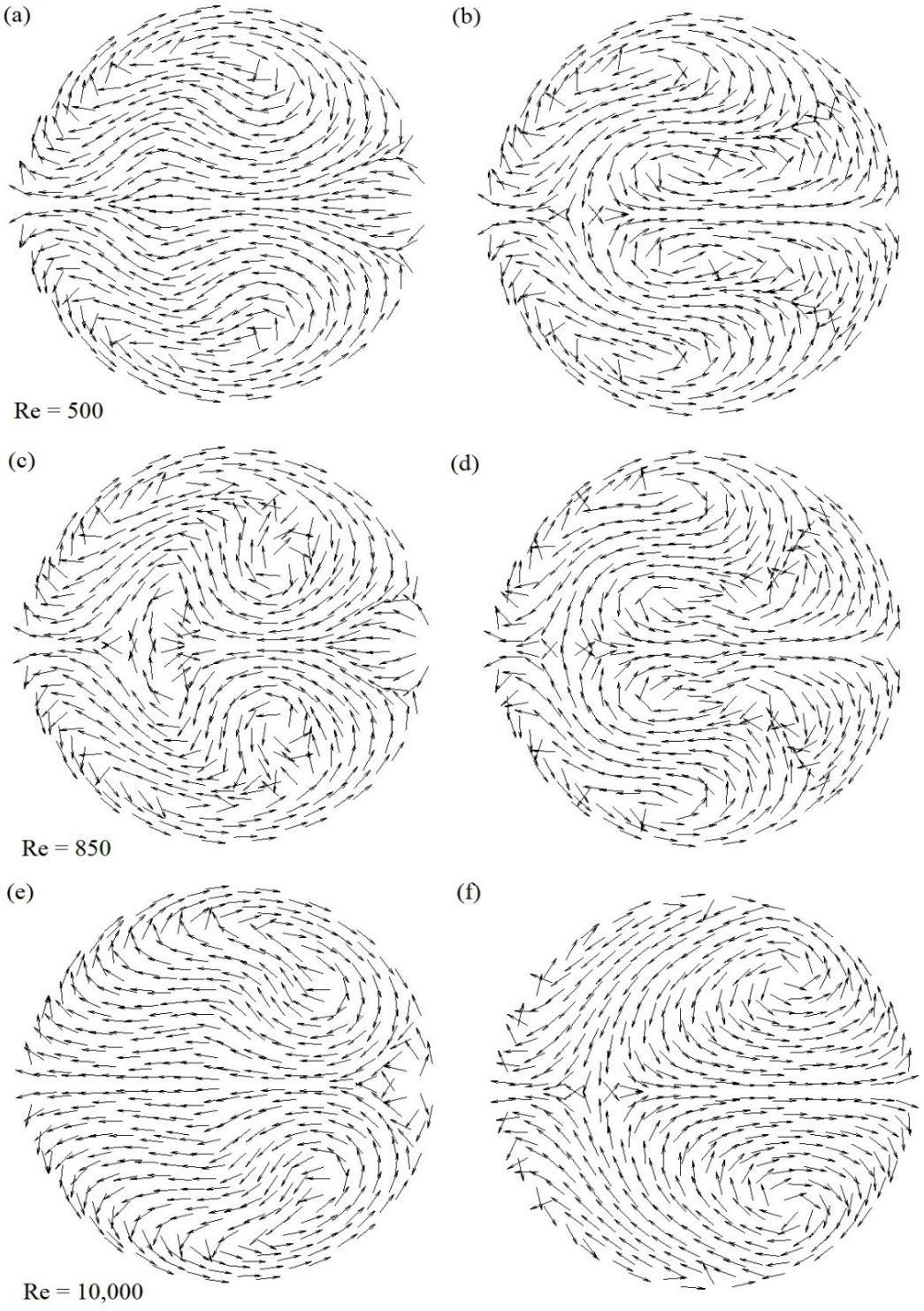

Fig. 5.5 *Normalized vector diagrams showing fluid flow in the bend exit plane for radius of curvature ratio = 3. The images on the left, (a), (c), and (e), are for the case with no blockage and those on the right, (b), (d), and (f), are for the 60% blockage case. Each pair of images corresponds to a given Reynolds number: Re = 500, 850, and 10,000*

Heat Transfer

The heat transfer results will be presented in terms of the circumferentially averaged Nusselt number $Nu_D = hD/k$. The heat transfer coefficient h is the circumferentially averaged coefficient defined by

$$h = \frac{\int_0^{2\pi} q\frac{D}{2}d\theta dx}{(\pi D dx)(T_w - T_b)} = \frac{\int_0^{2\pi} q d\theta}{2\pi(T_w - T_b)} \tag{5.2}$$

in which q is the local angle-dependent heat flux at a streamwise location x, and T_b is the bulk temperature at that x; T_w is the uniform wall temperature. In the presentation that follows, the Nusselt number for a specified Reynolds number, blockage ratio, and radius of curvature ratio will be plotted as a function of x/D. In view of the fact that the results for all six Reynolds numbers will be conveyed on a given plot, and that there are four blockage ratios and two radius of curvature ratios, the entire presentation of heat transfer results will necessitate eight graphs. In order to provide perspective of the trends that will be identified in the heat transfer figures, each of such figures will be supplemented by a display of velocity magnitudes at a succession of cross sections starting at the exit of the bend and progressing downstream.

To begin, attention will first be focused on the results for the radius of curvature ratio of 1, with successive figures for blockage ratios of 0, 20, 40, and 60%. Figure 5.6a, which corresponds to the blockage ratio of 0%, is a graph in which the Nusselt number is plotted as a function of *x/D* with the Reynolds number as curve parameter. In order to enable a presentation that will encompass the widely different ranges of the Nusselt number corresponding to Reynolds numbers ranging from 100 to 10,000, Fig. 5.6a has been structured with a main section for the higher Reynolds numbers and an inset section for the lower Reynolds numbers.

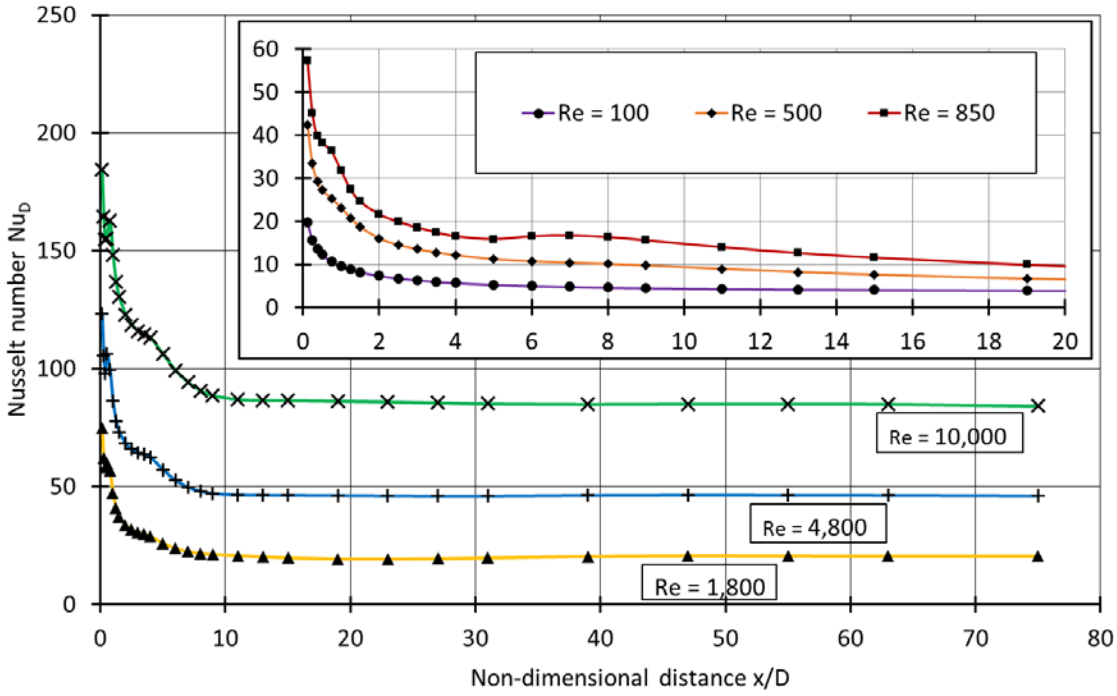

Fig. 5.6a *Nusselt number results for Reynolds numbers ranging from 100 to 10,000 for a radius of curvature ratio of 1 and blockage ratio of 0%.*

In assessing the results, it is relevant to note that the fluid-flow model for the Reynolds numbers of 100, 500, and 850 was chosen to be laminar whereas the model for the Reynolds numbers of 1,800, 4,800, and 10,000 was turbulent. The Nusselt number graphs display some slightly irregular variations with *x/D* that, in the absence of upstream blockage, may be ascribed solely to the geometry-based complexity of the flow. In particular, for the three higher Reynolds numbers of 1,800, 4,800, and 10,000, there are two unexpected features of the curves that merit discussion. One of these, which can be seen at locations x/D ~ 0.5, is a rapid dropoff followed by a rapid rise in the Nusselt number. This behavior may be given qualified attribution to the presence and subsequent decay of a pocket of backflow. The other feature are moderate humps in evidence in the curves at approximately x/D ~ 5. These humps may be attributed to the developing velocity field downstream of the bend exit.

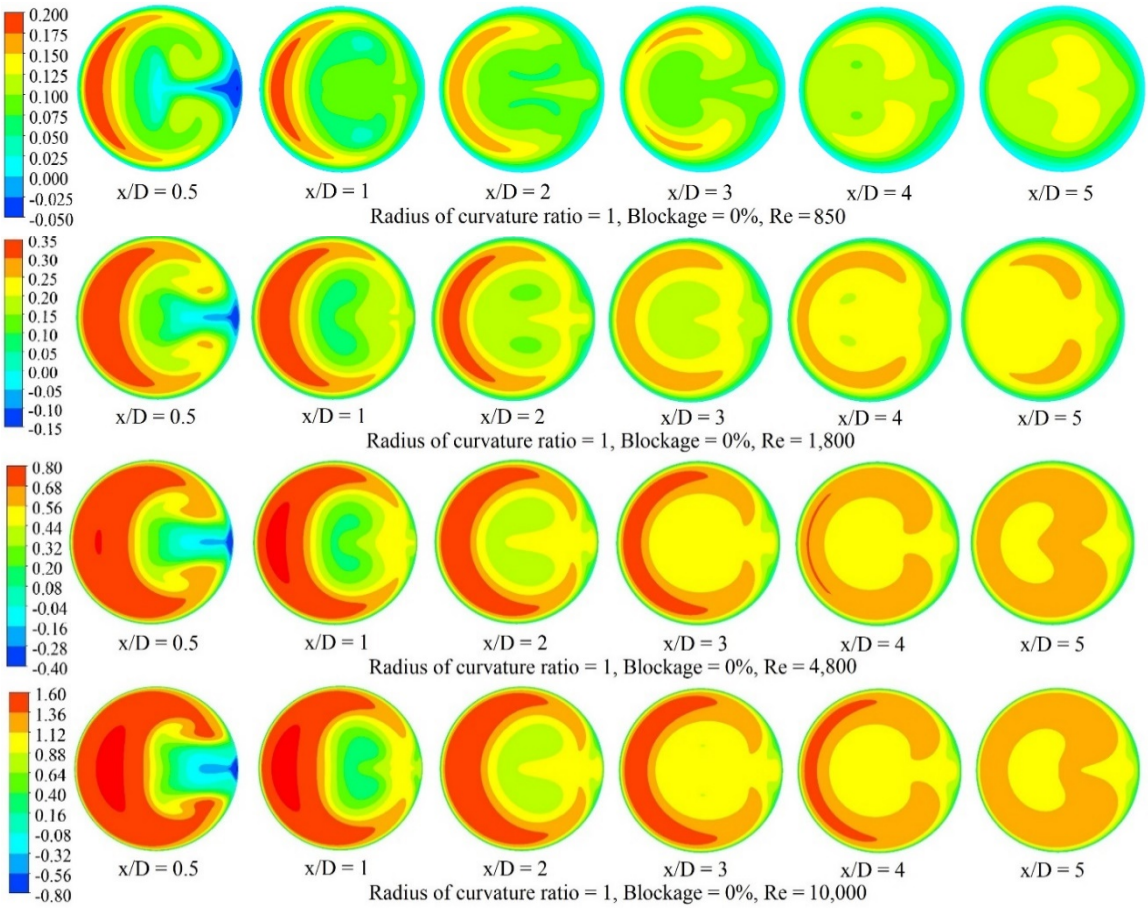

Fig. 5.6b *The color contour diagrams display the axial velocity magnitudes in m/s in cross sections that are situated from x/D = ½ to 5*

For the Reynolds numbers of 500 and 850, unexpected shapes are encountered for the Nusselt number curves. First of all, at x/D ~ 1, modest humps can be seen. Furthermore, for Re = 850, an unexpected wave in the Nusselt number curve is in evidence between x/D = 5 and 12. This unique behavior for Re = 850 would appear to add reinforcement to the conjecture that this Reynolds number corresponds to flow in the transition (intermittent) regime.

The Nusselt number graphs clearly display a thermal entrance region and a fully developed region. For the upper three Reynolds numbers, thermally developed flow appears to have been achieved at *x/D* = 10. The situation for the lower three Reynolds numbers seems to be more dependent on the value of the Reynolds number. At the lowest Reynolds number, Re = 100, thermal development is fully complete by *x/D* = 10, which substantiates standard expectations. Those expectations also suggest increasingly longer

development lengths at higher laminar Reynolds numbers. This expectation is fulfilled for Re = 500 and 850; however, for Re = 850, the situation is somewhat distorted by the aforementioned humps in the curves.

The assemblage of the color contour diagrams displayed in Fig. 5.6b was put together with a view to illuminating the moderate humps. For the Reynolds numbers of 1,800, 4,800, and 10,000 (turbulent flow model), the color contour diagrams show that in the near neighborhood of the bend exit, there is a pocket of backflow. It may be reasoned that that pocket is the cause of the odd behavior of Nusselt number curves in that neighborhood. Further inspection of the color contour diagrams indicates a rapid redevelopment of the flow in the direction of greater uniformity. The presence of the backflow in the absence of upstream blockage is believed to be a finding of relevance. At very small values of *x/D*, the velocity distribution is tremendously skewed to the high pressure end of the cross section, but the distribution becomes more uniform with increasing downstream distance. There are some evidences of the formation and subsequent demise of circulation, both of which occur in shorter distances at higher Reynolds numbers. The aforementioned non-monotonic humps in the Nusselt number distributions may be ascribed to the complexity of the velocity distributions.

The assemblage of velocity magnitude diagrams includes the results for Re = 850. Inspection of the velocity magnitude diagram of that case shows a region of backflow immediately downstream of the bend exit. That region rapidly dissipates, and that flow reversal is believed to be related to the modest hump in the Nusselt number that begins in the neighborhood of x/D ~ 0.5. Further examination of that diagram shows that at x/D ~ 5, recirculation no longer exists. This establishment of a new flow pattern may be responsible for the wave in the Nusselt number graph that extends between x/D ~ 5 and 12.

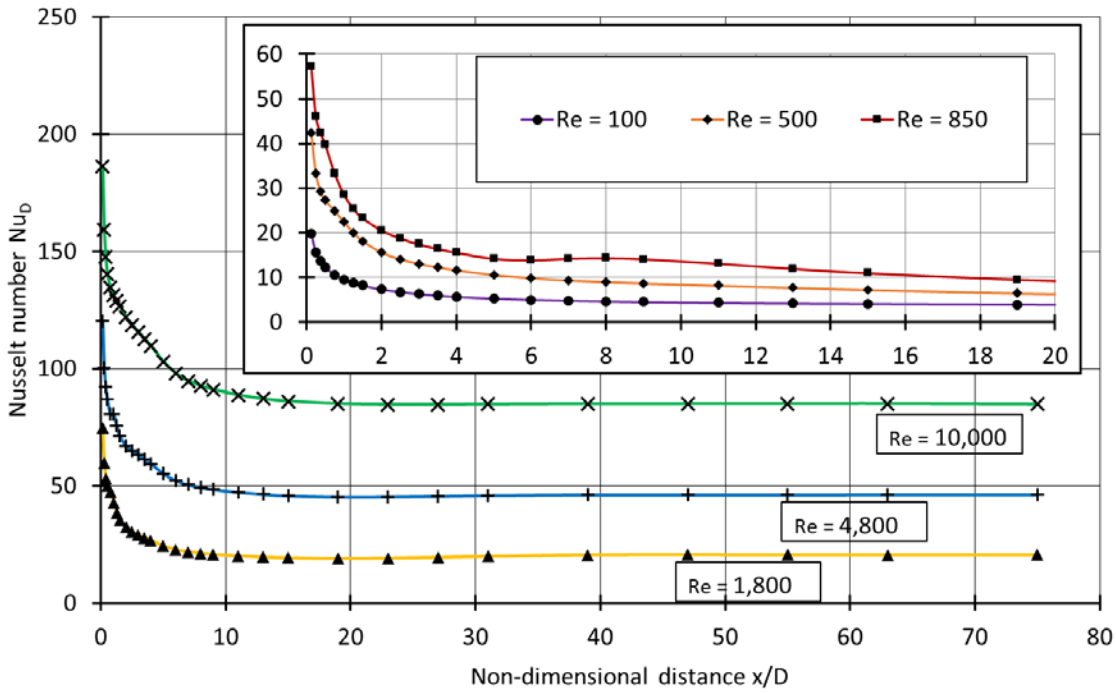

Fig. 5.7a *Nusselt number results for Reynolds numbers ranging from 100 to 10,000 for a radius of curvature ratio of 1 and blockage ratio of 20%.*

Attention may now be redirected to Fig. 5.7, which is the counterpart of Fig. 5.6 but for a blockage ratio of 20%. As was the case in the presentation for Fig. 5.6, there is a graph displaying the Nusselt number distribution as a function of axial location supplemented by an assemblage of color contour diagrams showing velocity magnitudes of the axial flow at several cross sections downstream of the bend exit, presented as parts (a) and (b).

An overview of the Nusselt number results of Fig. 5.7a reveals some similarities and some differences from those of Fig. 5.6a. The odd behavior in the neighborhood of x/D ~ 5 continues in force for Re = 4,800 and 10,000. However, that behavior has disappeared for Re = 1,800. In that regard, inspection of the color contour velocity diagrams indicate a different duration of backflow for the 0 and 20% cases. In addition, the evolution of the velocity distribution toward uniformity is considerably slower for 20% blockage than 0% blockage. The Nusselt number results for the lower three Reynolds numbers, shown in

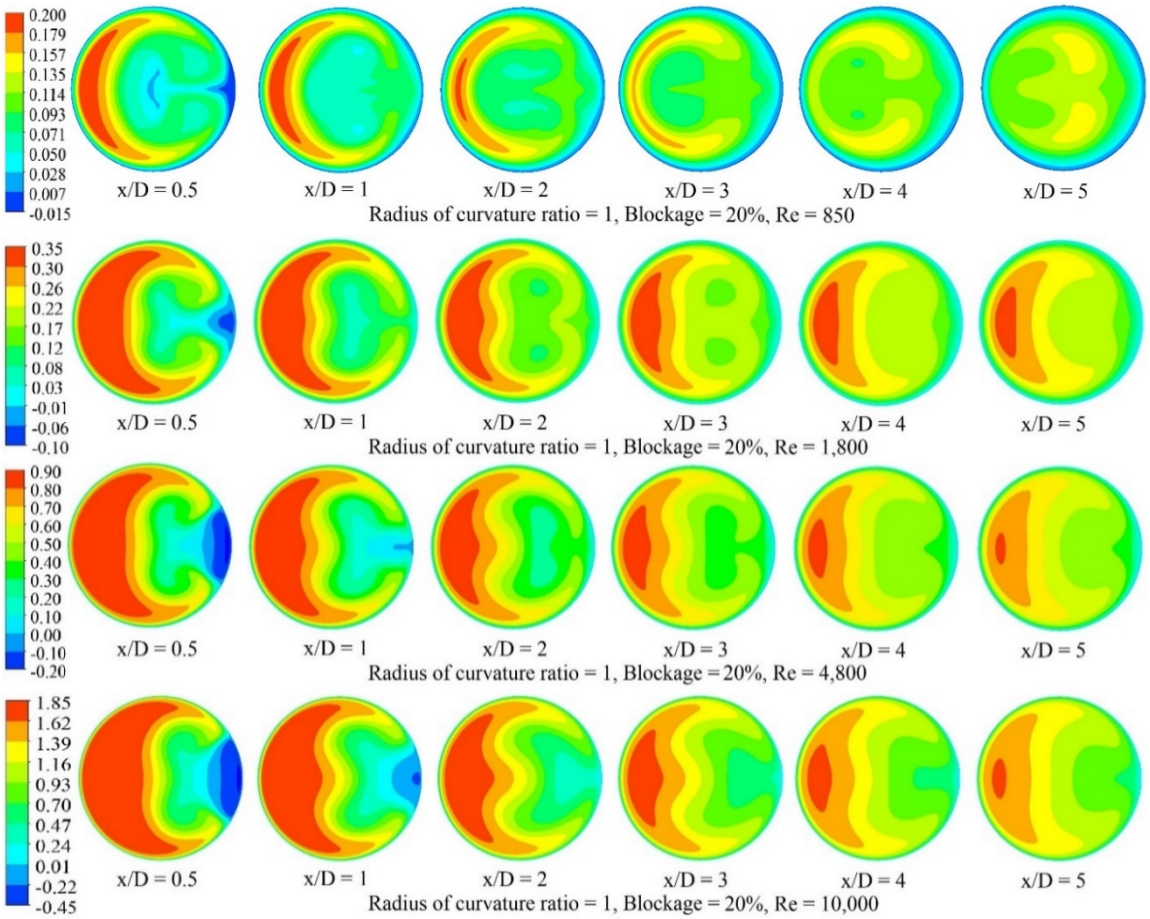

Fig. 5.7b *The color contour diagrams display the axial velocity magnitudes in m/s in cross sections that are situated from x/D = ½ to 5*

the inset of Fig. 5.7a, differs from what was seen in the inset of Fig. 5.6a in that the modest hump in the Nu distribution for Re = 850 in the neighborhood of x/D ~ 0.5 has

also disappeared but, on the other hand, the slight flattening of the Re = 500 curve in that same neighborhood of x/D persists for the 20% blockage. Overall, a comparison of the Nusselt number magnitudes for 0 and 20% blockage reveals small differences in the region of thermal development, but the fully developed values are unaffected.

The next blockage condition to be considered for presentation is 40%. The Nusselt number distributions for this case are conveyed in Fig. 5.8a with a supplement of color-contour displays for the magnitudes of the axial velocity in Fig. 5.8b. Overall, the Nusselt number curves are quite regular except for those for Re = 4,800 and 10,000. For the Re

=10,000 case, there is an odd behavior in the range between x/D ~ 2 and 4 whereby there is abrupt

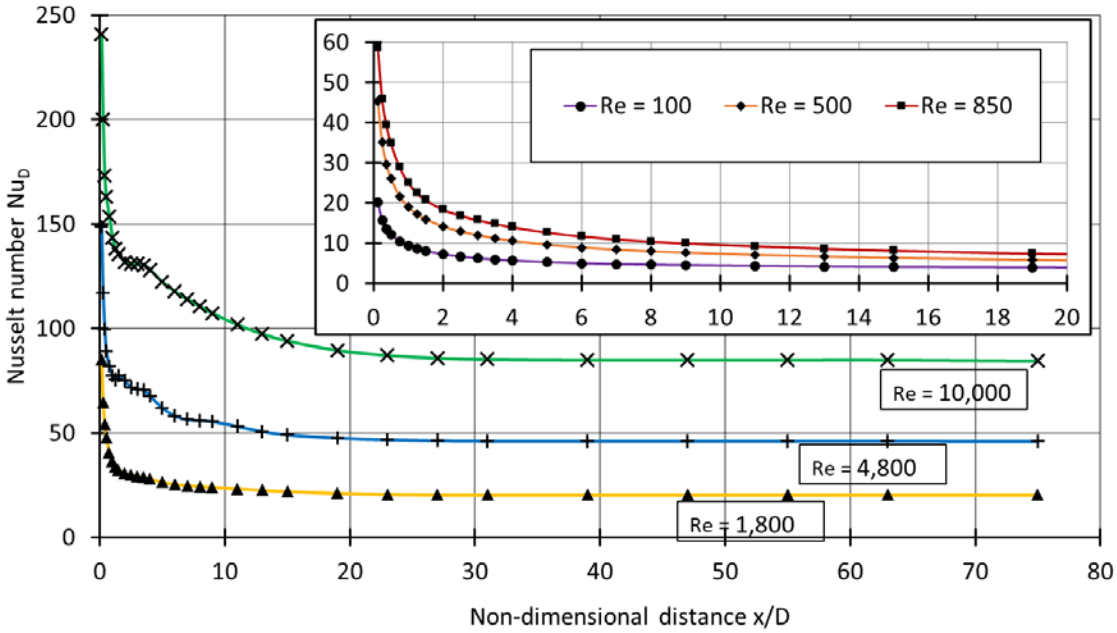

Fig. 5.8a *Nusselt number results for Reynolds numbers ranging from 100 to 10,000 for a radius of curvature ratio of 1 and blockage ratio of 40%.*

discontinuity in the slope of the Nu curve. On the other hand, for Re = 4,800, the Nu curve shows a flattening between x/D ~ 1.5 and 10. Inspection of the color contour velocity displays for these Reynolds numbers shows a pattern whereby the velocity distributions appear to be developing a stratified, non-axisymmetric distribution across the breadth of cross section.

The last of the cases for which Nusselt number results are presented is for the blockage ratio of 60%. Again, the Nusselt number display is supplemented by an assemblage of color contour velocity magnitude diagrams. This information is presented in Fig. 5.9. An overview of the Nusselt number figure shows that all of the three higher Reynolds number cases are affected by the blockage. For all these cases, the curves show a flattening in the range of x/D from about 1.2 to 10. For Re = 1,800, there is an abrupt change of slope at x/D ~ 1.2 similar to that observed for Re = 10,000 in the presence of the 40% blockage. Most remarkable is the Nusselt number curve for Re = 850.

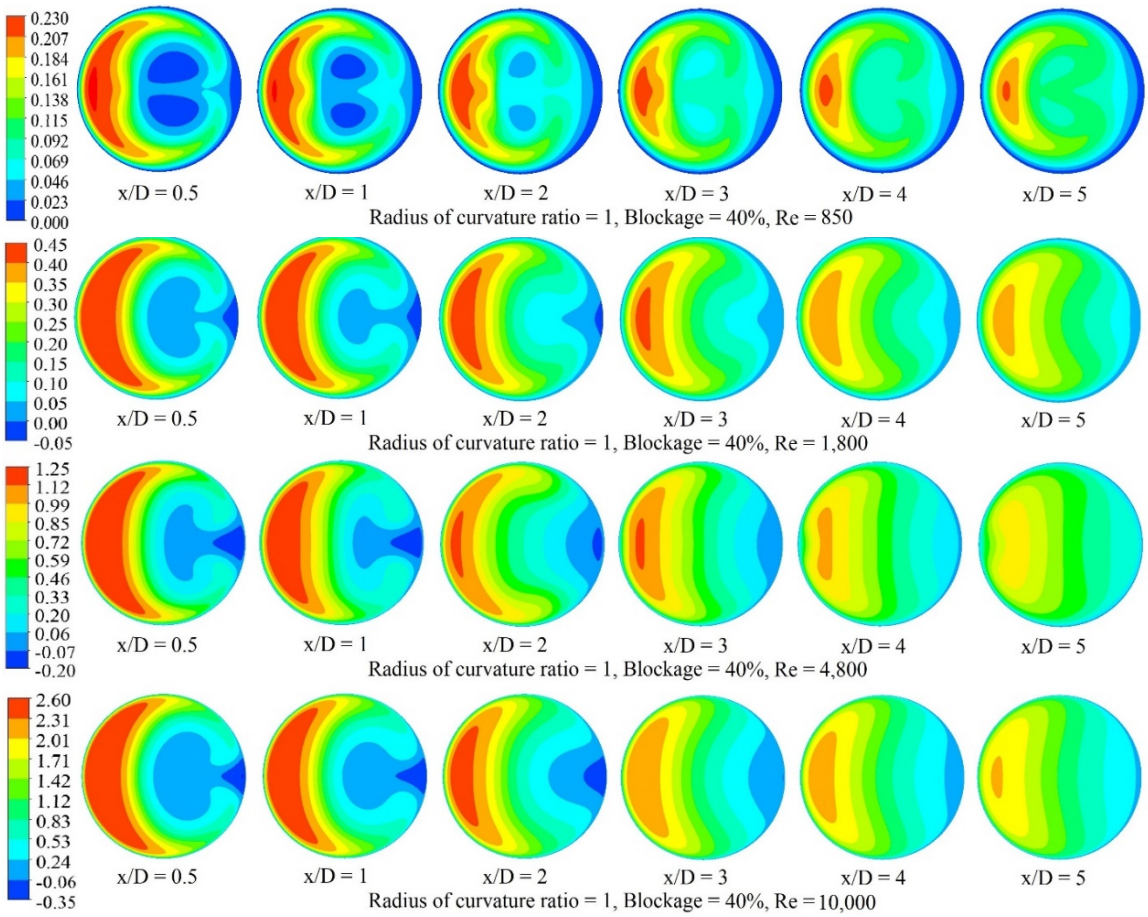

Fig. 5.8b *The color contour diagrams display the axial velocity magnitudes in m/s in cross sections that are situated from x/D = ½ to 5*

Clearly, the oscillatory nature of that curve suggests fluid flow complexity and adds to the conjecture of intermittent flow. From the color contour velocity diagrams for that case, a large backflow region initially exists and persists to x/D ~ 2. There is also seen a rapid change in the distribution of the flow which may be the major factor in the Nusselt number fluctuations. The Nusselt number results for the Reynolds numbers of 100 and 500 are quite regular and do not display any irregularities.

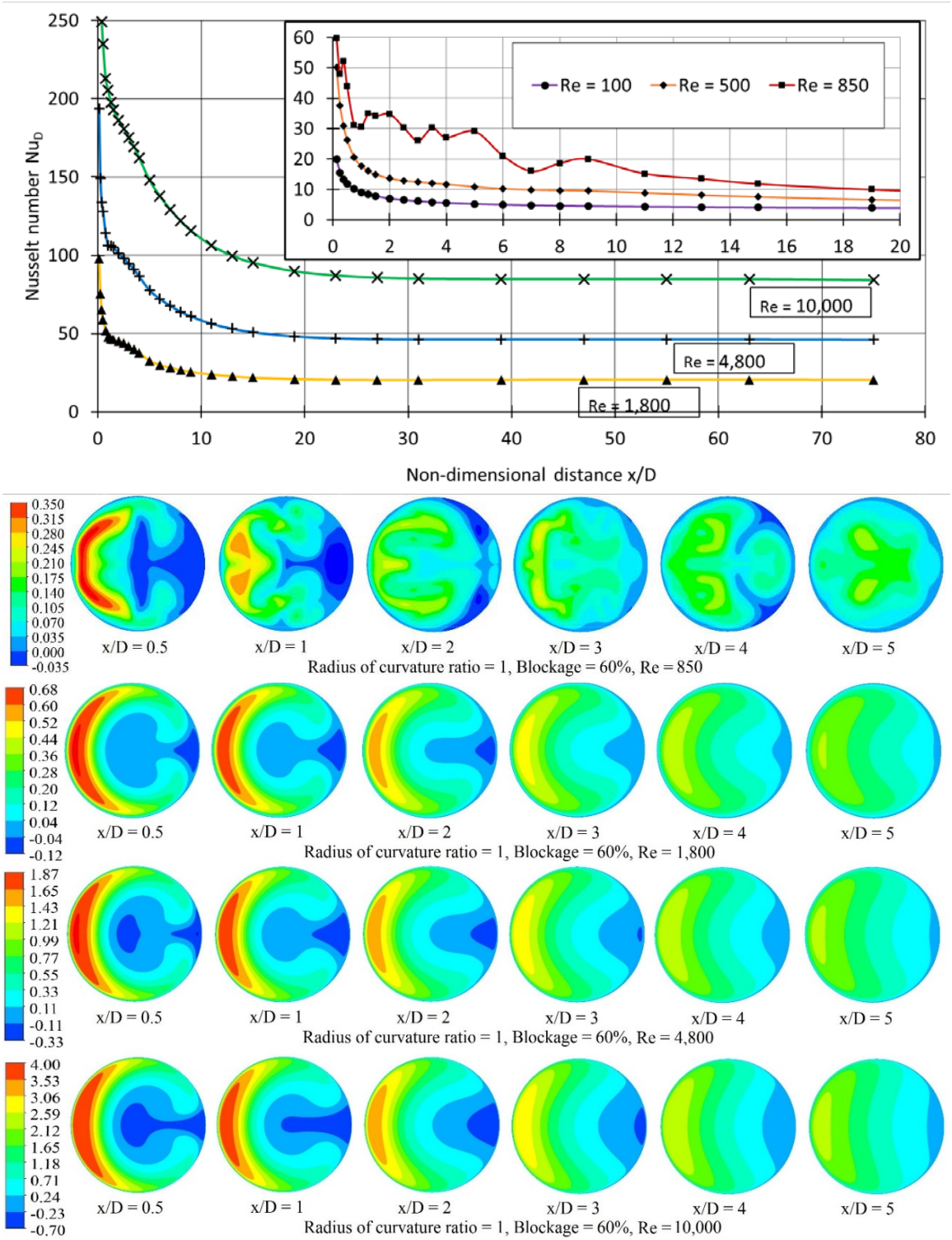

Fig. 5.9 *Nusselt number and axial velocity results for a radius of curvature ratio of 1 and blockage ratio of 60%*

The next set of results correspond to a curvature ratio of 3. The layout of the forthcoming presentation follows that of the just-presented results for the curvature ratio of 1. The first

of the forthcoming figures is Fig. 5.10 which corresponds to a blockage ratio of 0% and the entire slate of Reynolds numbers from 100 to 10,000. It is relevant to compare the Nusselt number distributions of Fig. 5.10 to those corresponding to the curvature ratio of 1 which have already been displayed in Fig. 5.6a. If that figure is revisited, both by inspection of the graph and of the textual discussion, it is immediately clear that there are very great differences between the cases depicted in Figs. 5.6 and 5.10. For the former, there are unique behaviors such as a hiccup in the curves at very small *x/D* for the three higher Reynolds numbers as well as a flattening of the curves for the same Reynolds numbers at slightly larger *x/D.* Equally unique is the wave in the Re = 850 curve that is seen in Fig. 5.6a.

None of these behaviors is evident in Fig. 5.10. Instead, careful inspection of the Nusselt number variations displayed in the main part of Fig. 5.10 reveals the presence of an undershoot in the value of the Nusselt number at *x/D* values less than 40. This phenomenon may be attributed to the process of laminarization. In that regard, it has been established that a turbulent flow entering a pipe may experience a return to a laminar boundary layer which may persist some distance into the pipe. Ultimately, turbulence is reestablished. The rate of decrease of laminar-flow heat transfer coefficients in the entrance region of a pipe is greater than the rate of decrease of turbulent-flow heat transfer coefficients, and it is this difference that is responsible for the undershoot.

The color contour diagrams for the axial flow show that there is no backflow for the 0% blockage for the radius of curvature ratio of 3. This is in contrast to the presence of backflow, displayed in Fig. 5.6b, for 0% blockage case for the radius of curvature ratio of 1. This difference may be attributed to the fact that the curvature ratio of 3 experiences a much diminished centrifugal force than does the curvature ratio of 1.

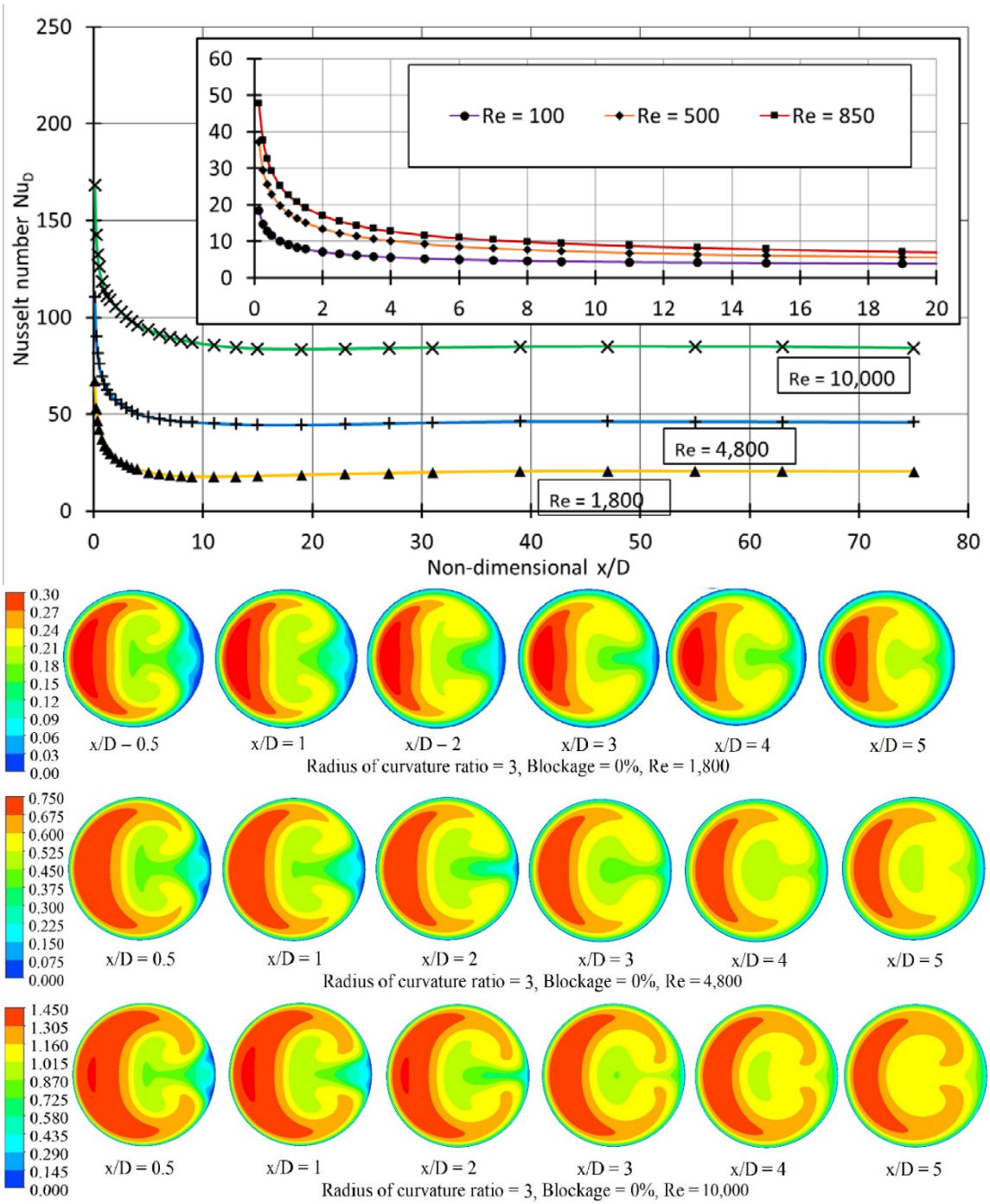

Fig. 5.10 *Nusselt number and velocity color contour diagrams for a radius of curvature ratio of 3 and 0% blockage*

Focus is now redirected to Fig. 5.11 for the 20% blockage case for the curvature ratio of 3. The Nusselt number results for this case do not show any significant differences relative to those for the 0% blockage case.

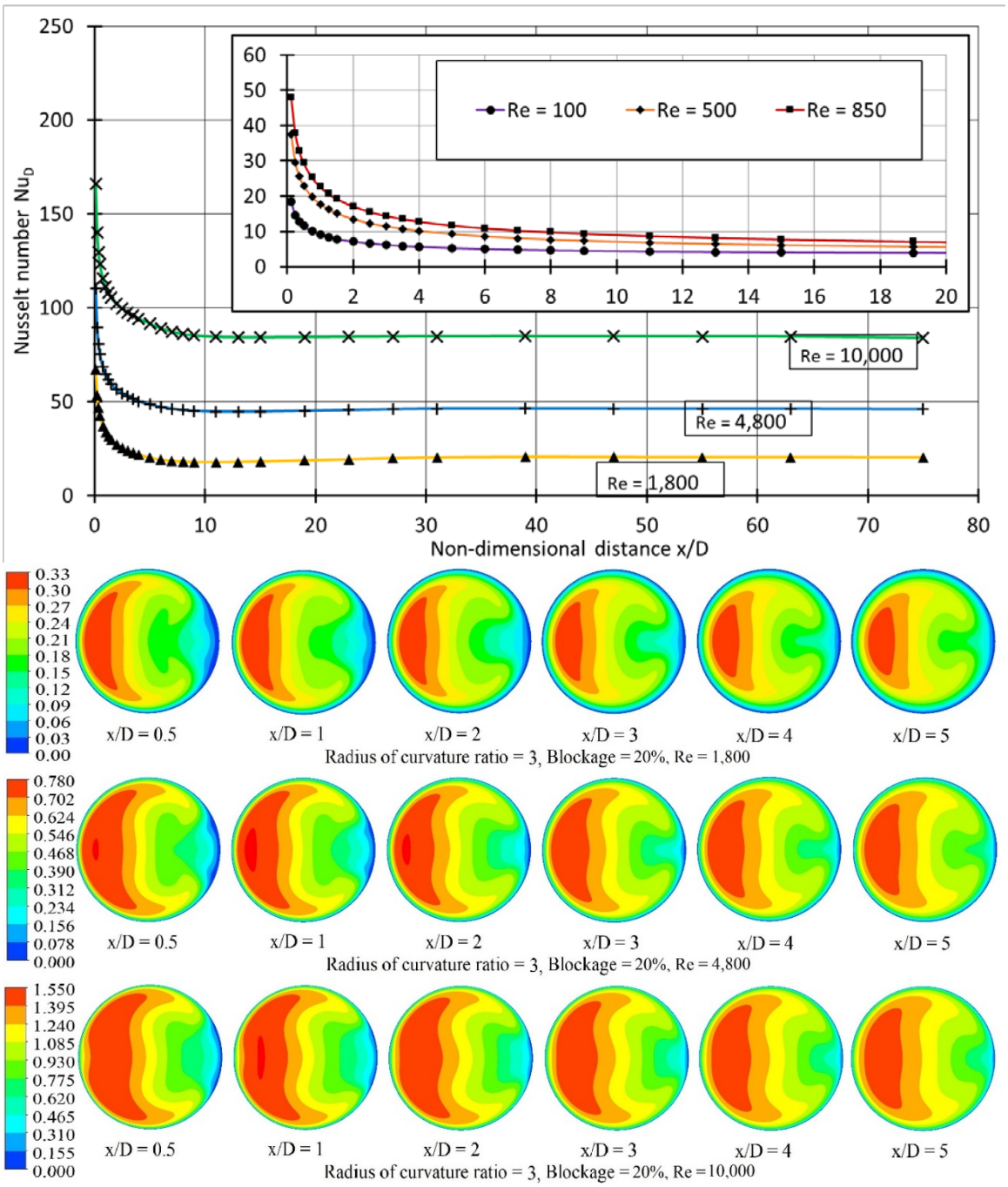

Fig. 5.11 *Nusselt number and velocity color contour diagrams for a radius of curvature ratio of 3 and 20% blockage*

Next, consideration is given to the blockage ratio of 40% for which the results are shown in Fig. 5.12. Compared with the results of Fig. 5.11 for the 20% blockage, there are some

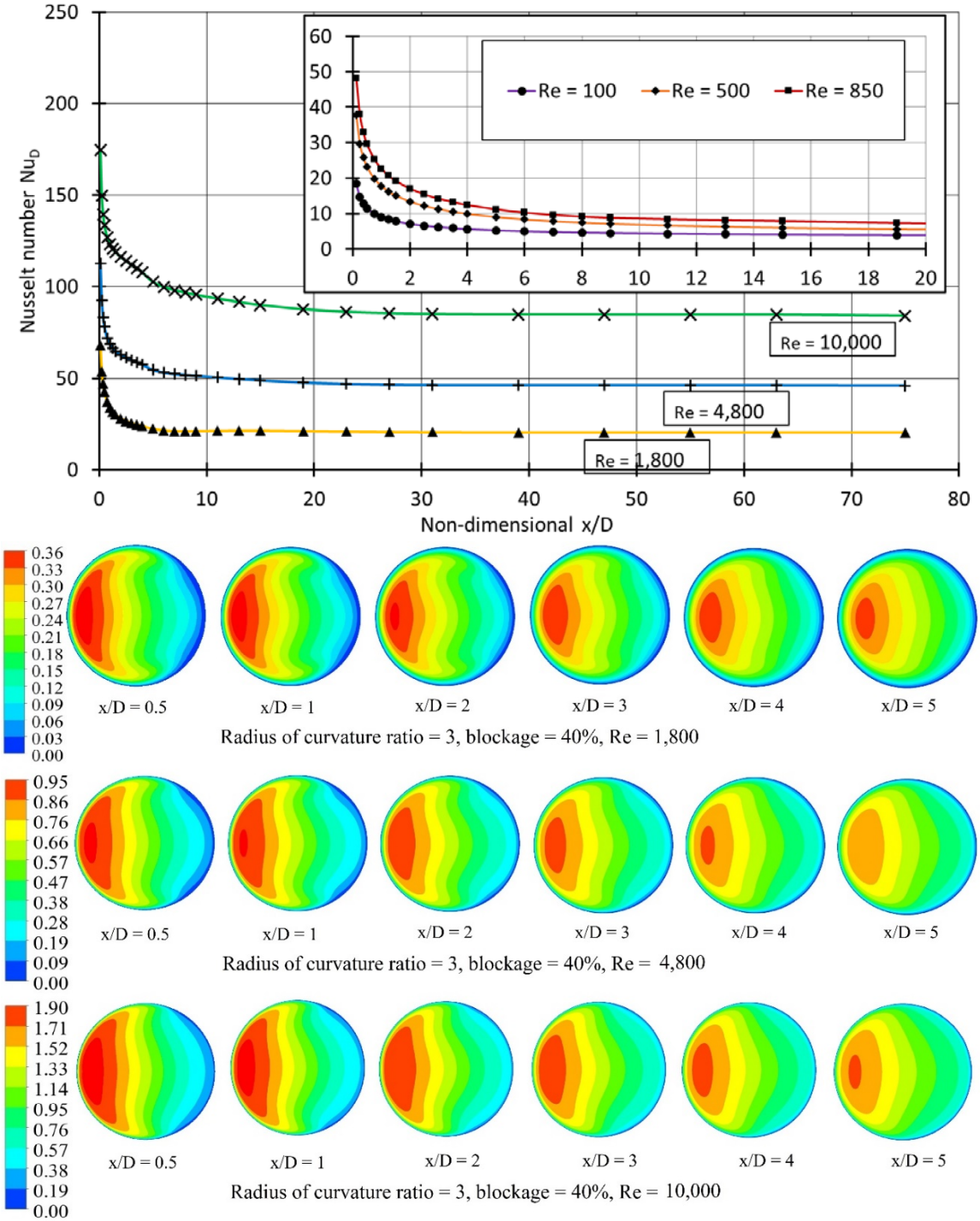

Fig. 5.12 *Nusselt number and velocity color contour diagrams for a radius of curvature ratio of 3 and 40% blockage*

significant differences. In particular, the undershoots no longer exist for the Reynolds numbers of 10,000 and 4,800, but a slight undershoot prevails for Re = 1,800. What is especially different in Fig. 5.12 is the flattening of the Nu distributions for small *x/D* for the Reynolds numbers of 10,000 and 4,800. This flattening was observed earlier in Figs. 5.6, 5.7, 5.8, and 5.9, all of which pertain to the radius of curvature ratio of 1. Inspection of the velocity contour diagrams in the lower portion of Fig. 5.12 reveals a newly prevailing distribution of velocity magnitudes which may be characterized as stratified. What is meant is that in a horizontal traverse from the high pressure end to the low pressure end, a monotonic decrease of the velocity would be encountered. This type of distribution has not been seen in any of the previous color contour diagrams.

Final focus is directed to Fig. 5.13 which corresponds to a blockage ratio of 60% for the curvature ratio of 3. In view of the large blockage afforded by the 60% case, it may be expected that ramifications would occur. For the Reynolds numbers of 4,800 and 10,000, the Nusselt number distributions in Fig. 5.13 are not significantly different from those in Fig.5.12 for the 40% blockage. No undershoot is seen for the Reynolds number of 1,800. What is of most immediate interest is that for Re = 850, the Nusselt number distribution now is disturbed by a wave-like pattern. That pattern was seen earlier in Figs. 5.6 and 5.7 for the 0 and 20% blockages for the radius of curvature ratio of 1. It is interesting that for the curvature ratio of 3, the lower Reynolds numbers appeared to be insensitive to the presence of blockage and may well have maintained laminar flow. The newly observed wave in Fig. 5.13 may well suggest the transformation of the Re = 850 case from laminar to intermittent.

The color-contour diagrams of Fig. 5.13 display the stratified pattern for all of the three turbulent Reynolds numbers. For Re = 850, the flow pattern is evidently much more complicated.

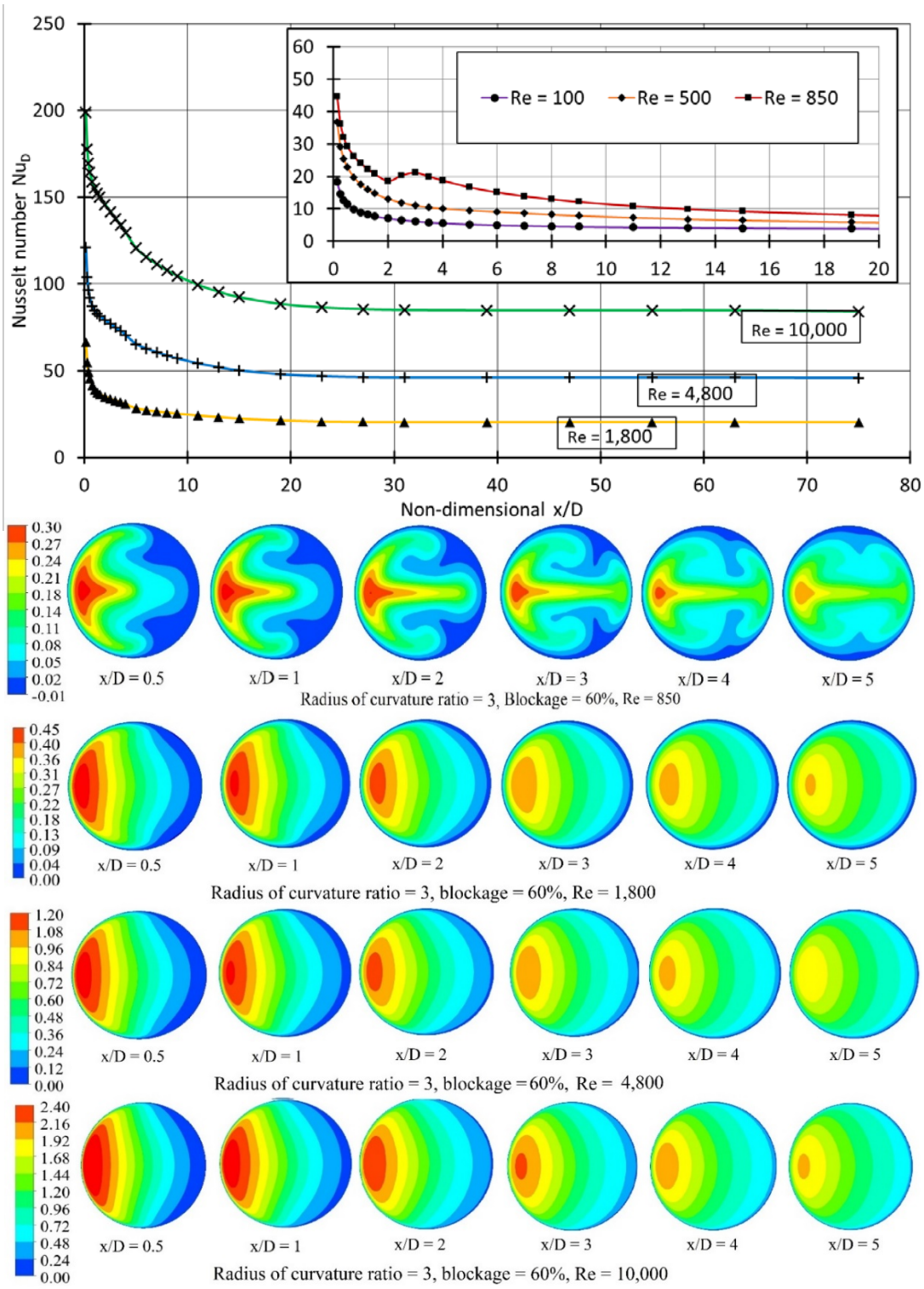

Fig. 5.13 *Nusselt number and velocity color contour diagrams for a radius of curvature ratio of 3 and 60% blockage*

5.5 Tabulation of Nusselt Number Results Showing Blockage Effect

The forgoing presentation of Nusselt number results was not the most convenient for isolating the effect of the magnitude of the blockage ratio. Here, a tabulation format is used to achieve this purpose. Two tables have been prepared for this purpose. Table 5.2 presents results for the radius of curvature ratio of 1, whereas the results for the curvature ratio of 3 are displayed in Table 5.3. The spaces created by the matrix of blockage ratio values and x/D values are filled with the corresponding Nusselt number values.

Table 5.2 consists of six subsections, respectively for Re = 100, 500, 850, 1,800, 4,800, and 10,000. In each subsection, the blockage ratios of 0, 20, 40, 60% are listed vertically at the left-hand edge. Across the top of each subsection, streamwise locations are listed horizontally from x/D = 0.25 to 6. The spaces created by the matrix of blockage ratio values and x/D values are filled with the corresponding Nusselt number value.

Overall inspection of Table 5.2 indicates that there is no single pattern of variation either with Reynolds number or with blockage ratio which is applicable to the entirety of the results displayed in the table. As a consequence, each of the subsections of a table will be considered separately. For Re = 100 in Table 5.2, it appears with only a single moderate exception, that the highest Nusselt numbers are for 0% blockage cases and the lowest Nusselt numbers are for the 60% blockage. Overall, for that Reynolds number, the variation of the Nusselt number with blockage ratio is small. For the results corresponding to Re = 500, there is a trend, except at x/D = 0.25, whereby the Nusselt number decreases with increasing blockage ratio from 0 to 40%. There is no consistent pattern in the change in the Nusselt number as the blockage ratio increase from 40 to 60%.

For Re = 850, there are different trends for different x/D values. For x/D = 0.25 and 0.5, the trend of Nu with blockage ratio is an initial increase, then a decrease followed by an increase when the blockage ratio reaches 60%. On the other hand, for x/D = 1, 2, 4, and 6, there is a monotonic decrease in Nu as the blockage varies from 0 to 40%, followed by an increase as blockage increases from 40 to 60%. In the case of Re = 1,800, there is an overall trend whereby the Nusselt number increases with increasing blockage, but the

Table 5.2 *Summary of Nusselt number results for radius of curvature ratio = 1*

Re = 100	***x/D = 0.25***	***x/D = 0.5***	***x/D = 1***	***x/D = 2***	***x/D = 4***	***x/D = 6***
0%	15.61	12.28	9.55	7.35	5.69	5.00
20%	15.67	12.29	9.52	7.32	5.68	4.99
40%	15.75	12.20	9.37	7.20	5.63	4.96
60%	15.55	11.88	9.08	7.03	5.57	4.96
Re = 500	***x/D = 0.25***	***x/D = 0.5***	***x/D = 1***	***x/D = 2***	***x/D = 4***	***x/D = 6***
0%	33.49	27.31	23.12	16.03	12.13	10.67
20%	33.25	27.25	22.44	15.61	11.61	9.83
40%	35.07	26.12	19.01	14.13	10.56	8.88
60%	37.64	26.20	17.68	13.57	11.71	10.23
Re = 850	***x/D = 0.25***	***x/D = 0.5***	***x/D = 1***	***x/D = 2***	***x/D = 4***	***x/D = 6***
0%	45.19	38.25	31.85	21.65	16.53	16.52
20%	46.04	39.79	28.57	20.56	15.56	13.85
40%	45.88	34.92	25.16	18.44	14.04	11.72
60%	48.00	43.84	30.57	34.76	27.05	20.99
Re = 1,800	***x/D = 0.25***	***x/D = 0.5***	***x/D = 1***	***x/D = 2***	***x/D = 4***	***x/D = 6***
0%	62.27	59.63	47.13	33.61	28.81	23.77
20%	59.75	50.03	42.81	32.24	26.67	22.81
40%	64.73	47.80	36.39	30.72	28.25	25.47
60%	75.37	59.03	47.91	45.29	37.67	29.96
Re = 4,800	***x/D = 0.25***	***x/D = 0.5***	***x/D = 1***	***x/D = 2***	***x/D = 4***	***x/D = 6***
0%	105.5	106.1	86.24	68.36	62.33	52.60
20%	100.3	86.77	80.44	66.96	59.31	52.20
40%	117.0	89.00	77.49	74.97	67.64	58.15
60%	149.2	128.1	106.2	101.3	86.47	72.07
Re = 10,000	***x/D = 0.25***	***x/D = 0.5***	***x/D = 1***	***x/D = 2***	***x/D = 4***	***x/D = 6***
0%	164.5	155.2	148.0	122.9	113.3	99.21
20%	159.1	140.3	131.1	121.8	109.5	97.84
40%	200.2	163.1	143.5	131.9	128.1	117.7
60%	264.9	235.0	205.4	186.4	162.3	137.9

increase is not monotonic. A similar pattern is observed for Re = 4,800. In particular, the Nu values corresponding to a blockage ratio of 60% are the largest for this Reynolds

number. For the largest Reynolds number, Re = 10,000, the aforementioned pattern for Re = 4,800 is repeated, but with an even more decisive maximum Nusselt number at the 60% blockage.

Finally, attention is redirected to Table 5.3. Inspection of the results for the two lowest Reynolds numbers, Re = 100 and 500, shows that the Nusselt number is virtually the same for all of the displayed cases except, perhaps, for the $x/D = 6$ situation for Re = 500. For Re = 850, the Nusselt number values for blockages of 0, 20, and 40% are virtually the same. When the blockage is increased to 60%, the Nusselt number either increases or decreases. Observation of the results for Re = 1,800 shows a pattern whereby the Nusselt numbers for $x/D = 0.25$, 0.5, and 1 are relatively constant for blockages of 0, 20, and 40%. For the other x/D values, there is a monotonic increase as the blockage ratio varies from 0 to 60%. Overall, for all cases for Re = 1,800, the maximum Nusselt number occurs for the blockage ratio of 60%. The trends of the Nusselt number with blockage ratio are the same for Re = 4,800 and 10,000. That pattern is a decrease in Nu as the blockage ratio increases from 0 to 20%. Thereafter, further increases in the blockage ratio up to 60% is coupled to a monotonic increase in the Nusselt number. For the Reynolds numbers, the maximum Nusselt number occurs for a blockage of 60%.

Overall, it appears that with regard to heat transfer enhancement, there is a general trend that the Nusselt number is highest at the largest blockage ratio.

Table 5.3 *Summary of Nusselt number results for radius of curvature ratio = 3*

Re = 100	***x/D = 0.25***	***x/D = 0.5***	***x/D = 1***	***x/D = 2***	***x/D = 4***	***x/D = 6***
0%	14.65	11.56	9.053	7.093	5.627	4.987
20%	14.65	11.56	9.053	7.093	5.627	4.987
40%	14.63	11.53	9.040	7.080	5.627	4.987
60%	14.59	11.49	9.000	7.067	5.613	4.987
Re = 500	***x/D = 0.25***	***x/D = 0.5***	***x/D = 1***	***x/D = 2***	***x/D = 4***	***x/D = 6***
0%	29.41	22.95	17.68	13.45	10.16	8.587
20%	29.45	22.97	17.69	13.45	10.13	8.560
40%	29.75	23.16	17.75	13.37	9.947	8.333
60%	29.19	22.87	17.51	13.07	10.15	9.107
Re = 850	***x/D = 0.25***	***x/D = 0.5***	***x/D = 1***	***x/D = 2***	***x/D = 4***	***x/D = 6***
0%	37.67	29.39	22.61	17.11	12.81	10.96
20%	37.83	29.49	22.68	17.15	12.81	10.91
40%	38.00	29.59	22.65	16.97	12.39	10.23
60%	36.13	29.33	24.01	18.60	18.77	15.12
Re = 1,800	***x/D = 0.25***	***x/D = 0.5***	***x/D = 1***	***x/D = 2***	***x/D = 4***	***x/D = 6***
0%	53.11	42.32	33.95	27.19	21.63	19.00
20%	53.49	42.51	33.95	27.20	21.69	19.11
40%	53.80	42.55	33.99	28.12	23.96	21.53
60%	54.71	45.67	39.19	35.04	30.76	27.35
Re = 4,800	***x/D = 0.25***	***x/D = 0.5***	***x/D = 1***	***x/D = 2***	***x/D = 4***	***x/D = 6***
0%	90.16	76.04	65.43	57.31	50.21	47.56
20%	89.51	75.08	64.63	56.64	50.13	47.15
40%	92.31	77.97	68.47	62.56	57.48	53.03
60%	103.9	92.16	84.68	79.20	70.51	62.77
Re = 10,000	***x/D = 0.25***	***x/D = 0.5***	***x/D = 1***	***x/D = 2***	***x/D = 4***	***x/D = 6***
0%	142.8	126.1	114.1	105.8	95.97	91.25
20%	140.1	123.2	111.2	102.1	94.36	89.09
40%	149.5	133.4	123.3	116.2	107.8	99.83
60%	177.7	164.3	155.1	145.8	129.3	115.5

5.6 Concluding Remarks

This chapter is motivated by interest in how downstream fluid-flow and heat transfer processes are affected by upstream flow disturbances. An idealized model of a means for creating such disturbances is developed and implemented by numerical simulation. The investigated physical situation is a 90^o pipe bend fitted at its inlet with a wall-adjacent washer-like obstruction that partially blocks the flow cross section.

The work of this chapter continues and extends the theme of fluid-flow complexity with heat transfer that marked the preceding chapters of this thesis. Here, the number and type of independent variables enables more definitive control of the extent of the complexity. There are three independent variables that have to be considered with respect to the physical situation that is the focus of this chapter. One of these, the blockage ratio, directly affects both the shape of the velocity profile carried into the bend and the extent of the zone of flow separation that exists in the wake of the blockage element. A second, the radius of curvature of the bend, has a direct effect on the sharpness of the 90^o turn and on the extent of the centrifugal force exerted on the fluid. The third variable, the Reynolds number, distinguishes between the relative importance of inertia forces and friction forces.

When the blockage ratio is set equal to 0%, the flow complexity at the bend exit is totally due to processes occurring in the bend, that is, secondary flow and the centrifugal force. At the maximum considered blockage ratio of 60%, it may be anticipated that the presence of blockage would contribute considerably to the complexity of the flow at the bend exit.

For the heat transfer situation, the fluid passing through the bend is strictly adiabatic. As a consequence, the fluid exiting the bend is isothermal. The wall of the pipe attached to the pipe-exit cross section is also isothermal, but at a temperature that exceeds the bend-exiting fluid temperature. Although the heat transfer results are the main focus of the work, the dominating influence of the patterns of fluid flow on convective heat transfer

motivates an in-depth display of flow-mechanic results to enable a logical understanding of the trends among the presented heat transfer quantities.

The heat transfer results are presented in terms of the circumferential-averaged heat transfer coefficient. The dimensionless form of this quantity is the local Nusselt number, which is displayed as a function of the dimensionless streamwise coordinate x/D. The conventional streamwise variation of the local Nusselt number is a monotonic decrease with increasing x/D. However, many of the displayed Nu vs x/D distributions do not follow this simple path. In particular, for the three turbulent-flow cases considered, local hiccups may be encountered as well as non-smoothly fitted flat portions of the Nu vs x/D curves. For the most part, these unexpected irregularities can be traced to pockets of backflow in the fluid in the neighborhood just downstream of the bend exit or to rearrangement of the shape of the velocity profile in that neighborhood. One of the Reynolds numbers selected for study, Re = 850, is normally for laminar flow in a conventional pipe flow. However, there is substantial evidence that that regime does not hold sway for certain of the investigated blockages or bend radii of curvature. In particular, the Nu vs /D curve may display a choppy variation or a wave-like shape.

CHAPTER SIX

Summary of Accomplishments

This thesis addresses a trio of unique and complex problems in turbulent-flow fluid mechanics and related heat transfer situations, none of which have previously been studied either in depth or at all in the past. All of these problems have roots of various depths in practical applications. The problems to be considered are: (a) flow created and governed by interactions with a piezometer ring, (b) initiation of large aspect-ratio rectangular jets, with downstream jet—free-space fluid interactions causing the jet axis-switching phenomenon, and subsequent impingement on a heat transfer surface, and (c) fluid flow and heat transfer downstream of the exit of a pipe bend in which there is partial cross-sectional blockages at the bend inlet.

These problems will be modeled and solved by means of numerical simulation. Since the flow regime for virtually all of the investigated cases is turbulent, a necessary part of the work is to select and validate an appropriate turbulence model. The selection and validation task is performed in Chapter Two. The validation methodology starts with the identification of a set of complete and accurate experimental data which correspond to a well-defined physical situation that is relevant to the main work of the thesis. Here, the meaning of completeness of the experiment is that the state of the turbulence at the inlet of the solution domain is known to high accuracy and is well documented. In the absence of such information, the problem is ill-defined and the calculation of the downstream flow is not definitive.

Since two of the three problems of interest here involve turbulent flow in bends and since appropriate experimental data for turbulent bend flow was available, the turbulence validation study was performed for that physical situation. The candidate turbulence model validated is the SST k-ω turbulence model. This model has been validated in the literature and in our laboratory by others for different situations, but never before for turbulent bend flow. The validation study performed in Chapter two was fully successful

in that the predicted flow field based on the SST k-ω turbulence model was in excellent agreement with the experimental data.

The focus of Chapter three is the piezometer ring. It is a small-diameter tube formed into the shape of a circle which girdles a pipe which contains a flowing fluid. The outer surface of the pipe wall is connected to the ring by means of several hollow radial spokes (i.e., pipe stubs). If there are circumferential pressure variations within the pipe flow, these variations are transmitted to the ring and may set up a circumferential flow in the ring which can, in turn, alter the flow in the pipe.

Piezometer rings are frequently encountered in engineering practice as an aid to pressure measurement. On the other hand, a thoughtful review of the literature suggests some fundamental doubts about whether the many uses of such instrumentation were performed in a manner that took proper cognizance of the participating fluid-mechanic phenomena. A major concern stemming from the literature search is the total absence of any rational approach to the choice of the optimum tap-off location on the ring circumference for capturing the mean pressure in the ring and conveying it to a proper measurement instrument. The use of piezometer rings seems to have had a life of its own despite the lack of a full understanding of the phenomena involved. The plan of the present work is to perform a deep fundamentals-based analysis that can also serve others who are appropriately dedicated to the use of piezometer rings as an experimental tool but would profit by a fuller understanding of the participating physical phenomena.

The situation chosen for the piezometer-ring study is the fluid flow downstream of the exit of a right-angle bend. This choice was made because this type of fluid flow possess a large but readily quantifiable circumferential pressure variation.

Two independent variables were taken into account during the course of the piezometer-ring investigation. One of these was the pipe Reynolds number which ranged from approximately 50,000 to 200,000. The other was the geometry of the piezometer ring.

Two rings, both of similar form but with different dimensions, were investigated. Each ring consisted of four radially deployed short lengths of round tubing which connected the pipe proper to a circular tube that girdles the pipe. The interconnections between the pipe and the ring were situated at 90^o intervals around the circumference of the pipe. Two of these locations respectively corresponded to the highest and lowest values in the circumferential pressure distribution, while the other two locations were at intermediate locations. These deployments coincided with standard practice as reported in the literature.

With regard to the results, major focus was directed to three issues: (a) the optimal circumferential locations of the radial bridges (spokes) connecting the pipe and the ring, (b) the optimal circumferential locations of take-off lines which enable accurate measurement of the pressure of the fluid flow in the pipe, and (c) the pressure drop penalty, if any, incurred by the use of a piezometer ring.

For the clear specification of these optimal take-off positions, the outside of the bend was described to be at the 0^o angular position and the inside of the bend was at the $\pm 180^o$ angular position. For the smaller piezometer ring, optimum pressure take-off occurred at angles of $\pm 50^o$ whereas for the larger piezometer ring, pressure take-off at $\pm 95^o$ was the most advantageous. The pressure drop between the pipe inlet and the bend exit was seen to increase due to the presence of the ring. For the smaller ring configuration, the increase relative to the no-ring pressure drop was on the order 15%. The pressure drop increase due to the presence of the larger ring configuration was about 10%.

The next chapter, Chapter four, is focused on jet impingement, an important real-world thermal management problem. It is well established that jet impingement is capable of providing the largest possible values of the convective heat transfer.

Jets are created by numerous means, often simplified for the purposes of analysis relative to actual jet-producing geometries. Here, a geometry that possesses high fidelity with respect to real-world applications is considered. In particular, the jet, which is air, is

produced at the outlet cross section of a long rectangular duct. The duct outlet cross section is capped by a plate which possess a rectangular slit which transforms the fully developed duct flow into a sharply etched rectangular jet. The thus-created jet passes into a free space without obstructions and finally impinges on a square plate situated at the downstream end of that space. The temperatures of the impinging air and the target plate are different, thereby giving rise to heat transfer at the plate surface.

The investigated independent variables include the dimensionless separation distance between the jet egress location and the impingement plate surface. For each of several fixed values of the separation distance, several intervening stations are selected to define planes that are parallel to the impingement plate. The distribution of the jet velocity in all such planes is displayed in order to illustrate the morphing shape of the jet cross section. Those displays clearly document that during its time of flight between the egress slit and the impingement plate, the cross-sectional shape of the jet may evolve from a pure rectangle mirroring the slit geometry to a circular cross section or an intermediate shape upon impingement. This phenomenon, called jet-axis switching, has not in the past been demonstrated for the range of Reynolds numbers investigated here. The Reynolds number, the second independent variable of this investigation, ranged from 11,000 to 88,000.

Jet-axis switching is shown to have a profound effect on the heat transfer coefficients on the surface of the impingement plate. Results for the local transfer coefficient are presented individually on graphs at the stagnation point, along the horizontal axis of the impingement plate and along the vertical axis of the impingement plate. Color contour diagrams are used to display the full spatial distribution of the transfer coefficient over the entire surface of the impingement plate. The highest values of the transfer coefficient occur at the smallest separation distance between the jet egress slit and the impingement plate. With increasing separation distance, there is a general decrease in the magnitude of the coefficient. Furthermore, the spatial distribution of the coefficient changes significantly owing to jet-axis switching.

The last chapter of the thesis is Chapter five. Here, the focus is on the fluid flow and heat transfer in a circular pipe attached to and extending downstream from the exit cross section of a 90^o bend. The special feature of the physical situation is the presence of a wall-adjacent, ring-like blockage at the bend inlet immediately adjacent to its upstream end. As a consequence, the flow exiting the bend is affected by the combined effects of the secondary flow in the bend and the separated flow due to the blockage. Heating of the flow with a uniform-wall temperature boundary condition begins at the bend exit. The flow in the bend proper is strictly adiabatic. The working fluid for this study is water with a Prandtl number of 5.77.

All told, six values of the pipe-based Reynolds number were selected for study: Re = 100, 500, 850, 1,800, 4,800, and 10,000. Among these values, the lower three were modeled as laminar flow, and the upper three as turbulent flow. For each Reynolds number, consideration was given to four blockage ratios: 0, 20, 40, and 60%, defined as the ratio of the blocked cross-sectional area to the total cross-sectional area. The final parameter was the radius of curvature ratio, with values of 1 and 3. This ratio is defined as the actual radius of curvature to the pipe diameter.

The strong dependence of convective heat transfer on the patterns of fluid flow motivated a display of velocity vector diagrams showing the nature of the flow patterns in the bend exit cross section for both the blockage-free and with-blockage cases. For the former case, there are numerous schematic diagrams of in-bend cross sections in textbooks showing fluid flow patterns. These images are generally over-simplified in that they show too-perfect symmetry, both up-and-down and side-to-side.

On the contrary, the present results indicate that the secondary-flow eddies are displaced toward the low-pressure zone of the cross section. The present flow patterns for Re = 850 show the greatest deviations from the textbook diagrams. In the presence of the upstream blockages, the flow patterns are less regular, especially that for Re = 850. There are significant differences in the flow patterns for the curvature ratios of 1 and 3. For the latter, even the flow patterns for the no-blockage cases are significantly more distorted

than would be expected based on textbook images. In the presence of blockage, the in-cross-section velocity patterns are markedly distorted, with flow directions reversed from those for the no-blockage case.

The main focus of the presentation of results is on the circumferential-averaged heat transfer coefficients (Nusselt numbers) displayed as a function of the downstream distance x/D from the bend exit. In general, the expectation of the heat transfer coefficient decreasing monotonically with increasing x/D is fulfilled, but with significant deviations in detail. These departures from monotonic behavior are attributable to the presence of pockets of backflow (upstream flow) in the immediate neighborhood of the bend exit. Interestingly, backflow is seen to occur both in the absence and in the presence of upstream blockage. The most affected situations are the Reynolds numbers of 850, 4,800, and 10,000.

For the Re = 850 case, there appears to be ample evidence that the laminar flow specification is not correct, and that the flow is better described as intermittent or transitional. For the other Reynolds numbers, the originally selected flow regimes appear to be supported by the results of the numerical simulations.

Bibliography

[1] Enayet, M. M., Gibson, M. M., Taylor, A. M. K. P., & Yianneskis, M. (1982). Laser-Doppler measurements of laminar and turbulent flow in a pipe bend. *International Journal of Heat and Fluid Flow*, *3*(4), 213-219.

[2] Enayet, M. M., Gibson, M. M., Taylor, A. M. K. P., & Yianneskis, M. (1982). Laser Doppler measurements of laminar and turbulent flow in a pipe bend. *NASA Contractor Report 3551*.

[3] Li, A., Chen, X., Chen, L., & Gao, R. (2014). Study on local drag reduction effects of wedge-shaped components in elbow and T-junction close-coupled pipes. In *Building Simulation* (Vol. 7, No. 2, pp. 175-184). Tsinghua University Press.

[4] W. Li, J. Ren, J. Hongde, Y. Luan, P. Ligrani, Assessment of six turbulence models for modeling and predicting narrow passage flows, Part 2: Pin fin arrays, *Numer. Heat Tr. A-Appl.*, vol. 69, pp. 445-463, 2016.

[5] U. Engdar and J. Klingmann, Investigation of Two-Equation Turbulence Models Applied to a Confined Axis-Symmetric Swirling Flow. In *ASME 2002 Pressure Vessels and Piping Conference*, pp. 199-206, 2002.

[6] Park, J., Park, S., & Ligrani, P. M. (2015). Numerical predictions of detailed flow structural characteristics in a channel with angled rib turbulators. *Journal of Mechanical Science and Technology*, *29*(11), 4981-4991.

[7] E.M. Sparrow, J.M. Gorman, and J.P. Abraham, Quantitative Assessment of the Overall Heat Transfer Coefficient U, *ASME Journal of Heat Transfer*, vol. 135, p. 061102, 2013.

[8] Y. Bayazit, E.M. Sparrow, and D.D. Joseph, Perforated Plates for Fluid Management: Plate Geometry Effects and Flow Regimes, *International Journal of Thermal Sciences*, vol. 85, pp. 104-111, 2014.

[9] P. D. Clausen, S. G. Koh, and D. H. Wood, Measurements of a swirling turbulent boundary layer developing in a conical diffuser, *Exp. Therm. Fluid Sci.*, vol. 6, pp. 39-48, 1993.

[10] Gorman, J. M., Sparrow, E. M., Abraham, J. P., & Minkowycz, W. J. (2016). Evaluation of the efficacy of turbulence models for swirling flows and the effect of turbulence intensity on heat transfer. *Numerical Heat Transfer, Part B: Fundamentals*, *70*(6), 485-502.

[11] Blake, K. A. (1976). The design of piezometer rings. *Journal of Fluid Mechanics*, *78*(2), 415-428.

[12] Vilbrandt, F. C. (1938). A One-Piece Standard Pipe Tee Piezometer Ring. *Industrial & Engineering Chemistry Analytical Edition*, *10*(3), 168-169.

[13] Vleggaar, J., & Tels, M. (1973). A remarkable drag-reduction phenomenon. *Chemical Engineering Science*, *28*(1), 309-311.

[14] Withers, J. G. (1980). Tube-side heat transfer and pressure drop for tubes having helical internal ridging with turbulent/transitional flow of single-phase fluid. Part 1. Single-helix ridging. *Heat Transfer Engineering*, *2*(1), 48-58.

[15] Barber, M. E., Bakeer, R. M., Sever, V. F., & Boyd, G. R. (2005). Effect of close-fit sliplining on the hydraulic capacity of a pressurized pipeline. *Tunnelling and underground space technology*, *20*(1), 23-31.

[16] Beyler, C. L. (1977). An evaluation of sprinkler discharge calculation methods. *Fire Technology*, *13*(3), 185-194.

[17] Petroe, G. (1943). Venturi meter and method of measuring liquids flowing through it. *U.S. Patent 2,337,921, issued December 28, 1943.*

[18] Keagy, W. R., & Ellis, H. H. (1948, January). The application of the schlieren method to the quantitative measurement of mixing gases in jets. In *Symposium on Combustion and Flame, and Explosion Phenomena* (Vol. 3, No. 1, pp. 667-674). Elsevier.

[19] Collins, D. B., & Gacesa, M. (1971). Measurement of steam quality in two-phase upflow with venturimeters and orifice plates. *Journal of Basic Engineering*, *93*(1), 11-20.

[20] Keulegan, G. H., & Beij, K. H. (1937). *Pressure losses for fluid flow in curved pipes*. US Government Printing Office.

[21] Welsh, M. C. (1976). Flow control in wide-angled conical diffusers. *ASME, Transactions, Series I-Journal of Fluids Engineering*, *98*, 728-735.

[22] Bullen, P. R., Cheeseman, D. J., Hussain, L. A., & Ruffellt, A. E. (1987). The determination of pipe contraction pressure loss coefficients for incompressible turbulent flow. *International journal of heat and fluid flow*, *8*(2), 111-118.

[23] Seliger, M., & Kurszewski, S. (2006). *U.S. Patent Application No. 11/362,323*.

[24] Grinstein, F. F. (1995). Self-induced vortex ring dynamics in subsonic rectangular jets. *Physics of Fluids*, *7*(10), 2519-2521.

[25] Yu, H., & Girimaji, S. S. (2008). Study of axis-switching and stability of laminar rectangular jets using lattice Boltzmann method. *Computers & Mathematics with Applications*, *55*(7), 1611-1619.

[26] Akbarzadeh, M., Birouk, M., & Sarh, B. (2012). Numerical simulation of a turbulent free jet issuing from a rectangular nozzle. *Computational Thermal Sciences: An International Journal*, *4*(1).

[27] Manivannan, P., & Sridhar, B. T. N. (2013). Characteristic study of non-circular incompressible free jet. *Thermal Science*, *17*(3), 787-800.

[28] Chen, N., & Yu, H. (2014). Mechanism of axis switching in low aspect-ratio rectangular jets. *Computers & Mathematics with Applications*, *67*(2), 437-444.

[29] Gorman, J. M., Sparrow, E. M., & Abraham, J. P. (2014). Slot jet impingement heat transfer in the presence of jet-axis switching. *International Journal of Heat and Mass Transfer*, *78*, 50-57.

[30] Churchill, S. W. (2002). A reinterpretation of the turbulent Prandtl number. *Industrial & engineering chemistry research*, *41*(25), 6393-6401.

[31] Kays, W. M. (1994). Turbulent Prandtl number—where are we?. *Journal of Heat Transfer*, *116*(2), 284-295.

[32] Gardon, R., & Akfirat, J. C. (1966). Heat transfer characteristics of impinging two-dimensional air jets. *Journal of Heat Transfer*, *88*(1), 101-107.

[33] Choo, K. S., Youn, Y. J., Kim, S. J., & Lee, D. H. (2009). Heat transfer characteristics of a micro-scale impinging slot jet. *International Journal of Heat and Mass Transfer*, *52*(13), 3169-3175.

[34] Miyazaki, H., & Silberman, E. (1972). Flow and heat transfer on a flat plate normal to a two-dimensional laminar jet issuing from a nozzle of finite height. *International Journal of Heat and Mass Transfer*, *15*(11), 2097-2107.